Platforms for Analyzing and Controlling Charge Transfer Processes at Semiconductor/Liquid Interfaces

by

Mitchell Lancaster

A dissertation submitted in partial fulfillment
of the requirements for the degree of
Doctor of Philosophy
(Chemistry)
in The University of Michigan
2019

Doctoral Committee:

Professor Stephen Maldonado, Chair
Professor Robert Kennedy
Professor Mark Meyerhoff
Professor Jamie Phillips

Mitchell M. Lancaster

mlanc@umich.edu

ORCID iD: 0000-0001-6829-6352

© Mitchell Lancaster 2019

ACKNOWLEDGEMENTS

I want to thank all my family and friends for support along my academic journey. My parents, Claire, Sunny, Swarly, and Aroo deserve a significant amount of credit for all the love and support that has allowed me to succeed while at Michigan. I also want to acknowledge all the excellent mentors and collaborators I've had the pleasure to work with throughout the years. None of this work would be possible without all of you.

TABLE OF CONTENTS

LIST OF FIGURES

LIST OF TABLES

LIST OF EQUATIONS

LIST OF SYMBOLS

$[A]$	Concentration of oxidized redox species
$[A^-]$	Concentration of reduced redox species
$[A^*]$	Bulk redox species concentration
A	Electrode area
a	Radial direction from electrode
a_i	Ionic radius of redox species
C_{dl}	Diffuse-layer capacitance
C_H	Helmholtz-layer capacitance
C_{sc}	Space-charge capacitance
C_{ss}	Surface state capacitance
C_{tot}	Total electrode capacitance
D_A	Diffusion coefficient of oxidized redox species
D_{A-}	Diffusion coefficient of reduced redox species
d	Electrode recession depth
E	Electrode potential
$E^{\circ\text{`}}$	Standard potential of redox couple
$E_{1/2}$	Potential at half the mass-transport limited current
E_a	Anodic degradation potential
$E_{applied}$	Applied potential to the electrode
E_c	Cathodic degradation potential
E_{cb}	Conduction band edge
E_F	Fermi level
E_{fb}	Flat-band potential
E_{onset}	Onset potential
E_{ss}	Surface state potential
F	Faraday constant

$F_{3/2}$	Fermi-dirac integral of order 3/2
$F_{1/2}$	Fermi-dirac integral of order 1/2
f	Fraction of surface states filled
I	Current
I_{tot}	Integrated current across electrode surface
J	Current density
$J_{L,a}$	Anodic limiting current density
$J_{L,c}$	Cathodic limiting current density
J_{sc}	Short-circuit current density
k_B	Boltzmann’s constant
k_b	Reverse rate constant
k_{et}	Heterogeneous electron-transfer rate constant
$k_{et,max}$	Rate constant at maximum exoergicity
k_f	Forward rate constant
k_{fit}	Fitted rate constant
k_{ss}	Rate constant for filling surface states
k_{ss-1}	Rate constants for emptying surface states
l	Surface layer thickness
m	Mass transport coeffect
N_{cb}	Effective density of states in the conduction band
N_d	Dopant density of the semiconductor
N_{ss}	Surface state density
n_{H2O}	Refractive index of water
n_{Si}	Refractive index of silicon
n_s	Surface concentration of majority carriers
$n_{s,E^{\circ}`}$	Surface concentration of majority carriers at Eo’
q	Unsigned charge of an electron
R	Molar gas constant
R_h	Distance between homogeneous charge transfer reactants
r	Electrode radius
T	Temperature

t	Time
V_{oc}	Open-circuit photovoltage
W_d	Depletion width
z	Direction normal to the electrode surface
α_{et}	Transfer coefficient for electron transfer
α_{fit}	Fitted transfer coefficient
β	Energy barrier for charge tunneling
γ	Ideality factor for charge transfer
ΔE_{dl}	Potential drop across the diffuse layer
ΔE_H	Potential drop across the Helmholtz layer
ΔE_{sc}	Potential drop across the space-charge region
ΔG°`	Driving force for charge transfer
δ	Thickness of Helmholtz layer
ε	Static dielectric constant of the semiconductor
ε_0	Permittivity of free space
ε_{CH3OH}	Dielectric constant of methanol
ε_{H2O}	Dielectric constant of water
$\varepsilon_{interface}$	Dielectric constant of the electrode interface
ε_{Si}	Dielectric constant of silicon
θ	Parameterized diffusion-kinetic relationship term
κ	Parameterized diffusion-kinetic relationship term
λ_{sc}	Total reorganization energy of redox couple
$\lambda_{sc,i}$	Inner-sphere contribution to the reorganization energy
$\lambda_{sc,o}$	Outer-sphere contribution to the reorganization energy
λ_{se}	Self-exchange reorganization energy
$\lambda_{se,i}$	Inner-sphere self-exchange reorganization energy
$\lambda_{se,o}$	Outer-sphere self-exchange reorganization energy
μ	Ionic strength of electrolyte
Ψ	Number of photogenerated charge carriers

ABSTRACT

This thesis describes new methods for the analysis and control of charge transfer processes at semiconductor/liquid interfaces. The main aim of this work is to utilize electrochemical methods to further understand, and ultimately, optimize semiconductor/electrolyte interfaces for solar energy conversion technologies. These strategies rely mainly on electrochemical techniques in which redox/precursor molecule flux can be precisely controlled for analysis or deposition by the aid of simple electronics. As such, the work presented herein is broadly applicable and easily adaptable for a myriad of applications.

The first portion of this thesis develops a new semiconductor ultramicroelectrode (SUME) platform for the analysis of charge transfer kinetics and thermodynamics at semiconductor/liquid contacts. Chapter 2 examines the geometrical dependence of the error in rate constant and transfer coefficient for electron transfer at a recessed metal UMEs to aid in design of the SUME platform. Simulated and experimental voltammetry demonstrate that recessed UMEs with thin insulating layers exhibit small errors in the rate constant and transfer coefficient for outer-sphere charge transfer reactions relative to their inlaid counterparts, especially when near-reversible kinetics are operative. Chapter 3 details the fabrication process and electrochemical behavior of n-Si SUMEs in aqueous media. The platform demonstrated behavior characteristic of metallic UMEs (e.g. high current densities) while maintaining inherent semiconductor properties. The SUMEs were shown to be highly sensitive to dynamic surface conditions, such as oxidation, and were used to broadly fit several outer-sphere redox couple to kinetic parameters in line with predictions from classical charge-transfer theory. Chapter 4 extends the utility of the SUME voltammetric response by considering how the applied potential is distributed across the interface. In doing so, nearly all energetic and kinetic parameters relevant to charge transfer at the semiconductor/liquid interface can be extracted directly from the voltammetric response.

The second portion of this thesis describes an electrochemical process for protective layer deposition directly on photoelectrodes for solar hydrogen production. Chapter 5 describes the photoelectrodeposition of MoS_x on p-$GaInP_2$ photocathodes. By controlling the deposition parameters, 8-10 nm films were deposited that exhibited minimal parasitic absorption of incident radiation and high catalytic activity for the hydrogen evolution reaction. The thin layers displayed excellent stability for over 50 hours of photoelectrolysis, highlighting this method as a simple strategy for protective layer formation with comparable photoelectrochemical properties to catalyst thin films formed by more energy-intensive and complex methods.

CHAPTER 1

Introduction

1.1. Context and Importance

The continued reliance on the combustion of fossil fuels as a primary energy source has led to an increased desire and need for alternative and clean energy solutions. Solar energy is often seen as an ideal candidate for low-carbon energy given a large and continuous overall energy output, relatively homogeneous distribution across the Earth's surface, and the ability to directly produce heat, electricity, or chemical fuels.[1-4] In particular, hydrogen is an intriguing solar energy conversion product given its high energy density, easy transmission and storage, and nominally benign combustion and usage by-products.[5-10]

Direct conversion of solar energy to hydrogen gas via photoelectrochemistry is regarded as a promising method for sustainable and renewable generation of hydrogen.[11-14] Since the initial demonstration of photoelectrochemical production of hydrogen on TiO_2 electrodes by Fujishima and Honda in 1972,[15] a dedicated effort has been made to understand the processes that govern sunlight absorption and subsequent fuel formation. Advances in materials' preparation and overall device design since this initial demonstration have led to direct solar-to-hydrogen efficiencies of 10-20%.[16-19] Still, much work is needed to develop this technology into a cost-effect method for renewable hydrogen production.

1.2. Technical Background

Photoelectrochemical Energy Conversion

The conversion of sunlight into hydrogen can be considered the sum of three main processes (Figure 1.1). First, photons with energies greater than or equal to the band gap of the photoelectrode material are absorbed, exciting an electron from the valence band to the conduction band and forming an electron-hole pair. One of these charges is then driven to the interface via the electrical field while the other is transported to the back contact. For example,

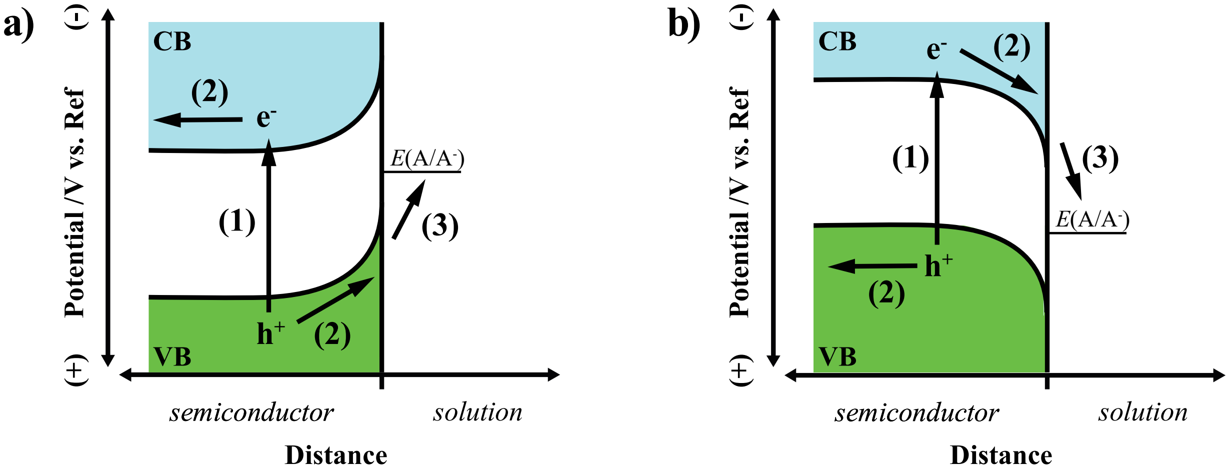

Figure 1.1. General mechanism of (1) charge generation, (2) separation, and (3) transfer for an (a) n-type and (b) p-type semiconductor photoelectrode.

an ideal n-type material will support electron transport to the back contact and hole transfer to the interface (Figure 1.1a). The opposite is true for a p-type material (Figure 1.1b). Finally, the photogenerated charge will pass across the interface and react with the redox couple in solution (e.g. protons) to generate the desired product.

Several attributes are generally necessary for efficient and stable conversion of sunlight to hydrogen. First, the bulk material properties need to be such that incident light can be absorbed efficiently. In general, direct, mid-sized band gap materials will absorb light most efficiently. Next, charges need to be collected at the interface before they recombine. In this sense, materials with high mobilities and carrier lifetimes are useful. Finally, charge transfer across the interface needs to be facile and stable. For most semiconductors, catalytic activity towards the photoelectrochemical reaction of interest is poor.[20] That is, photogenerated charges either recombine or react with surface atoms to degrade the material, resulting in lost performance. In fact, the long-term durability of photoelectrodes is widely considered the primary hinderance of large-scale implementation of cost-effective systems.[21, 22] In the 47 years since the initial demonstration of water photoelectrolysis, few systems have demonstrated high light-limited photocurrents maintained over 100 hours.[22] This is still far from the years-long stability necessary for commercial relevance. As such, continued work to understand and ultimately control the charge transfer processes at semiconductor/liquid interfaces that underpin this technology is paramount.

Charge Transfer at Semiconductor/Liquid Interfaces without Illumination

Energy level diagrams for an n-type semiconductor and a separated solution containing a dissolved redox couple, A/A^-, are shown in Figure 1.2a. In this case, the Fermi level of the semiconductor electrode, E_F, lies at a more negative potential than the formal electrochemical potential of the redox couple, $E°$`(i.e. $E_F$ of the solution). When the electrode is placed in contact with solution, electrons from the conduction band edge of the semiconductor, $E_{cb}$, transfer into solution. This process lowers $E_F$ and will continue until value of $E_F$ and $E°$` are equivalent. The equilibration state of the semiconductor/liquid contact is defined through a constant electrochemical potential of electrons across the interface (i.e. the Fermi levels are equal) (Figure 1.2b). A similar equilibration process occurs with p-type semiconductors with hole transfer to

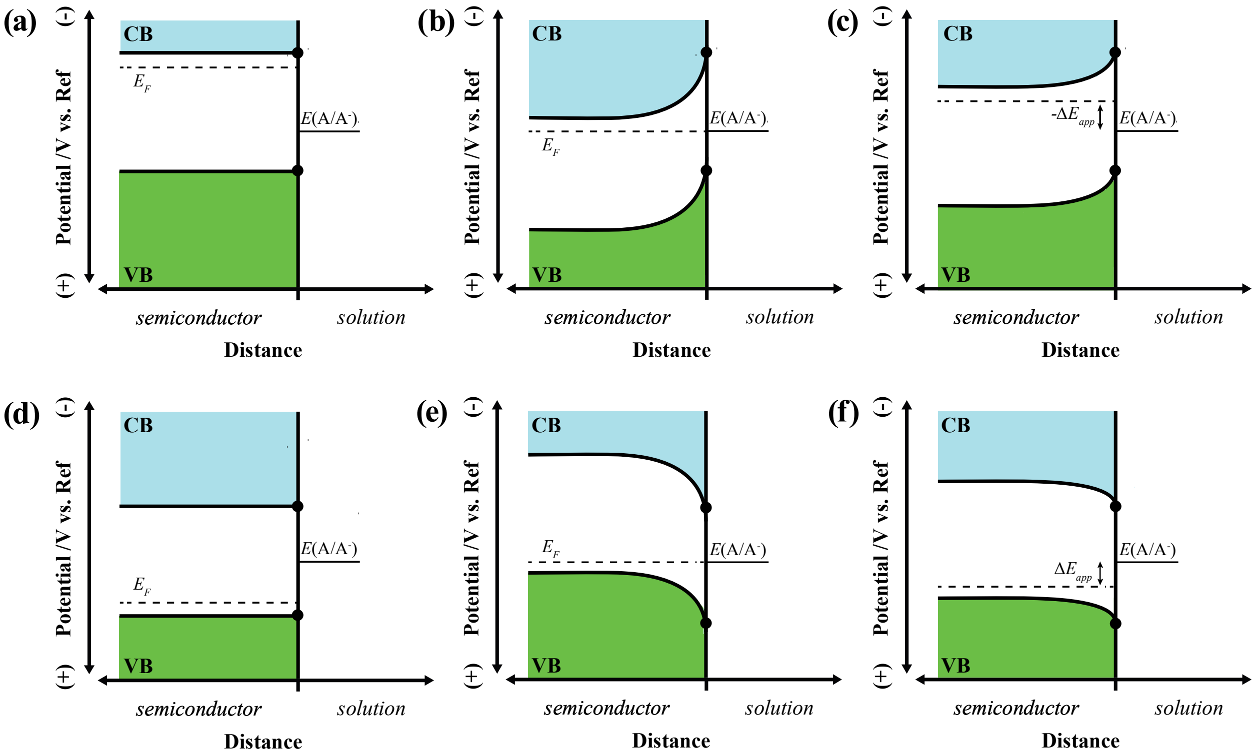

Figure 1.2. Band structures for an n-type semiconductor (a) before equilibration, (b) after equilibration, and (c) after a negative applied bias. The corresponding band diagrams for a p-type material are shown in (d-f) with a positive applied bias in (f).

solution. This is depicted in Figures 1.2d and 1.2e. The two main methods of perturbing equilibrium to affect desired changes in solution are through an applied bias or light. The effect of an applied bias will solely be considered herein.

The main result of the equilibration of a semiconductor electrode with an electrolyte solution is the formation of a region of the semiconductor depleted of majority charge carriers. For an n-type material, the electron density at the electrode surface is not sufficient to equilibrate the system. Electron density is then pulled from a region deeper within the material, leaving a region near the surface consisting of fixed positive charges. This region is known as the depletion region and typically has a width, W_d, of 10-1000 nm that depends on the bulk material dopant density and initial Fermi energy difference between the semiconductor and solution. The positive charge magnitude is largest at the semiconductor surface and gradually declines until the electron density reflects the bulk doping conditions. This charge density gradient produces a significant potential difference between the surface and the bulk of the semiconductor, resulting in the formation of an electrical field that directs electrons toward the semiconductor bulk. A similar field forms in p-type materials with opposite sign (i.e. electrons are directed toward the interface).

The electric field at the semiconductor/liquid interface acts as an energy barrier to charge transfer to acceptors in solution and has profound effects on the kinetics of interfacial processes. The current density for charge transfer from the conduction band edge of a semiconductor electrode to a freely diffusing acceptor species in solution is shown in *eq. 1.1,*

$$J(E) = qk_{et}n_s(E)[A] \tag{1.1}$$

where q is the charge of an electron, k_{et} is the heterogeneous charge transfer rate constant, [A] is the concentration of acceptor molecules in solution, and $n_s(E)$ is the potential-dependent surface concentration of electrons expression through *eq. 1.2.*

$$n_s(E) = N_d e^{\frac{q(E_{fb} - E_{applied})}{k_B T}} \tag{1.2}$$

Here, N_d is the bulk dopant density of the semiconductor electrode, E_{fb} is the flat-band potential, k_B is Boltzmann's constant, T is temperature, and $E_{applied}$ is the applied potential. The potential dependence on n_s has distinct implications for analysis of charge transfer at semiconductor electrodes. Namely, the application of a bias to the electrode alters the surface concentration of majority charge carriers rather than affecting the rate constant. That is, applied bias increases or decreases the energy barrier at the interface. This is largely different from kinetic analyses at metallic electrodes, where the carrier concentration is much larger (and not potential dependent) and built into the rate constant.[23] The reduction of band-bending at the semiconductor/liquid interfaces upon application of applied bias is highlighted for n- and p-type electrodes in Figure 1.2c and 1.2f, respectively.

The Charge Transfer Rate Constant

Determining k_{et} at semiconductor interfaces has been of long-standing interest for understanding the function of solid-state and solution junctions as well as addressing fundamental theories of charge transfer.[23-26] To this end, significant effort has been put forth to probe the factors that influence k_{et}. Similar importance has been placed on k_{ht}, however surface oxidation reactions at semiconductors electrodes nearly always occur in concert with corrosion reactions (*vide infra)*. As such, k_{ht} will not be considered here. Based on the classical framework for charge transfer,[27, 28] k_{et} can be expressed by *eq. 1.3,*

$$k_{et} = k_{et,\max} e^{\frac{(-\Delta G^{\circ}\text{`}-\lambda_{sc})^2}{4\lambda_{sc} k_B T}} \qquad (1.3)$$

where $k_{et,max}$ is the rate constant at optimal exoergicity, λ_{sc} is the reorganization energy of the redox couple in solution, and $\Delta G^{\circ}\text{`}$ is the driving force for charge transfer, given by *eq. 1.4*.

$$\Delta G^{\circ}\text{`} = E_{cb} - E^{\circ}\text{`} \qquad (1.4)$$

Based on this equation, the rate constant follows a parabolic relationship as shown in Figure 1.3, with the maximum k_{et} value at $-\Delta G^{\circ}\text{`} = \lambda_{sc}$. At $-\Delta G^{\circ}\text{`} > \lambda_{sc}$, the rate constant decreases. This regime is colloquially known as the 'inverted' region. More recent examinations with quantum mechanical-based methods have predicted a shallower decrease in k_{et} at large driving forces due to coupling with vibronic states.[29] This deviation from classical theory is shown with a dashed line in Figure 1.3.

Still, proving/refuting the existing theories for charge transfer has been challenging. Only several detailed examinations have been attempted. A series of rate measurements were obtained by Morrison and co-workers that showed compelling evidence of 'inverted' behavior for n-ZnO immersed in aqueous solutions with redox species possessing very positive standard potentials.[30]

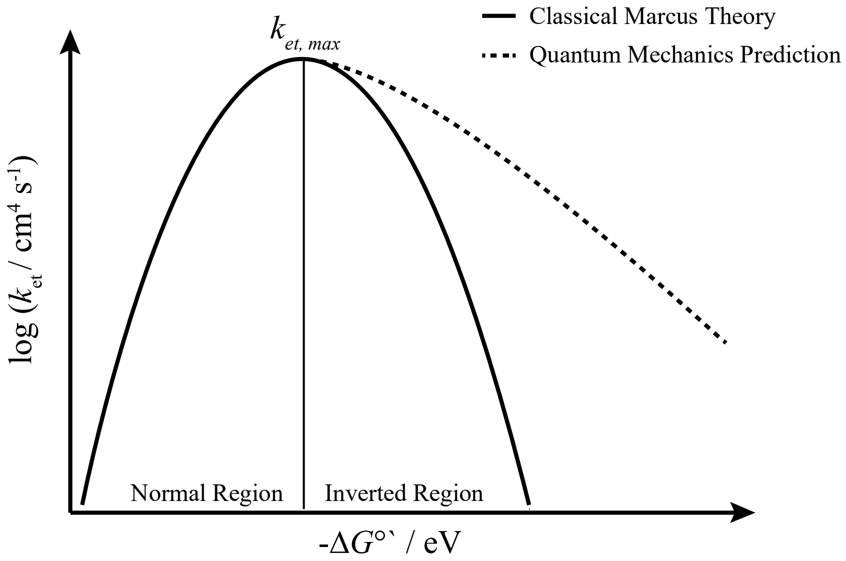

Figure 1.3. Classical and quantum mechanics-based rate constant predictions as a function of driving force.

Current-potential responses collected at currents less than the mass-transport-limited current, when extrapolated to the potential where there is no band bending within the semiconductor, yielded data suggestive of small values of k_{et}. Unfortunately, the interpretation was complicated by large uncertainties in the reorganization energies of the employed redox couples. Nevertheless, these measurements were consistent with theory predictions and actually preceded the more-cited studies of tethered donor-acceptor molecules and solvated electron reactions[31-35] that are credited for proving the existence of an ‘inverted region’. Later measurements with n-Si in non-aqueous solvents[23, 24] and n-ZnO in aqueous solutions[25, 26, 36] further supported the observation of ‘inverted’ behavior and reaffirmed the utility of semiconductor/solution interfaces for fundamental understanding of charge transfer processes.

One practical reason why only classical behavior has been observed in semiconductor electrochemistry is that comparatively few semiconductor/solution interfaces have been sufficiently studied, particularly in the absence of complications. Beyond the complexities associated with interfacial surface states, the uncertainty in previous rate constant measurements[30,37] may be large enough to mask the possibility of this aspect. Undoubtedly, the uncertainties in capacitive measurements of band edge potentials and in the reorganization energies of redox species decrease the precision in estimates of rate constants. Alternate approaches for making k_{et} and k_{ht} measurements would be valuable in this regard.

Durability of Semiconductor Photoelectrodes

A confounding factor of both practical water splitting systems and detailed investigations of charge transfer theory is the corrosion of semiconductor electrodes when in contact with liquid electrolyte.[38-41] By the nature of materials surfaces, undercoordinated surface atoms are highly reactive and constantly exposed to the atmosphere or solution. The chemical reactivity of surface can impact electronic properties and create defined electronic states at the interface, altering the overall charge transfer mechanisms and kinetics. A brief description of (electro)chemical corrosion mechanisms for relevant semiconductor materials is provided below.

The inherent thermodynamics of a semiconductor electrode contact can lead to electrode degradation under bias and/or illumination. Figure 1.4a and 1.4b shows the band edges of a semiconductor relative to potentials of arbitrary cathodic (E_c) and anodic (E_a) corrosion processes. In Figure 1.4a, both corrosion potentials are within the band gap of the semiconductor.

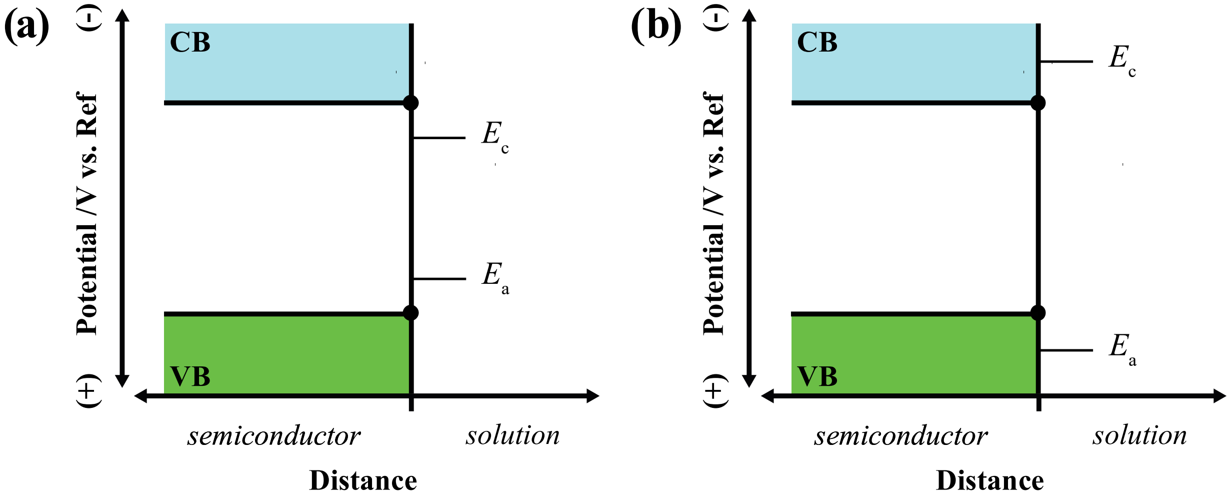

Figure 1.4. General band diagram for thermodynamically (a) unstable and (b) stable semiconductor materials.

That is, corrosion can spontaneously occur via majority carriers (in the dark) and minority carriers (under illumination), assuming sufficiently facile kinetics. Figure 1.4b shows a case where the cathodic and anodic formal potentials are above and below the conduction and valence band, respectively. Under these conditions, the electrode is thermodynamically stable.

Kinetic aspects can also induce corrosion processes. A key example relevant to this thesis is the photoreduction[42] and oxidation of surface Ga atoms in III-V semiconductors such as GaP and $GaInP_2$ under photoelectrochemical operation. Both GaP and $GaInP_2$ are relatively efficient in separating electron-hole pairs but exhibit poor kinetics for reactions such as hydrogen evolution and water oxidation.[21, 43] This results in the accumulation of charges at the interface that can react with surface atoms and affect electrode performance. For example, GaP can be oxidized by photogenerated holes through *eq. 1.5*,[44]

$$GaP + 4OH^- + 3h^+ \rightarrow GaO_2^- + P + 2H_2O \qquad (1.5)$$

where gallium oxide either dissolves into solution or acts as a passivating layer. A similar process occurs under cathodic conditions where photogenerated electrons can reduce surface gallium atoms to gallium metal, as shown in *eq. 1.6*.[42]

$$GaP + 3e^- \rightarrow Ga(l) + P \qquad (1.6)$$

In this case, metallic gallium can form a contact that prevents charge collection in solution and can absorb/reflect incident radiation. Methods to mitigate these degradation mechanisms will be discussed later in this thesis.

Electrochemical Analysis of Semiconductor Electrodes

Electrochemical analysis can be used to understand kinetic and mechanistic aspects of charge transfer related to semiconductor device performance and deleterious corrosion processes. Several platforms have been used for electrochemical analysis. The most common platform for charge transfer analysis involves measurement with macroscopic semiconductor electrodes (mm^2 or cm^2 area exposed to solution).[25, 45, 46] Several inherent limitations are present during the utilization of large semiconductor electrodes. First, the significant electrode area produces large current density magnitudes that can lead to appreciable ohmic drops, especially in resistive media such as aprotic organic solvents.[47] Additionally, the larger surface area exposes numerous surface defects states and can exhibit high current heterogeneity across the electrode, convoluting interpretation of the voltammetric response. Second, mass-transport limitations restrict the portion of the voltammetric response that can be analyzed without complications from mass transfer.[23] That is, the purely kinetically-limited portion of the response is limited to only tens of mV past the current onset. This is additionally complicated by the fact that no analytical relationship has been presented that can account for the voltammetric response under mixed kinetic- and diffusion-controlled regimes.[48]

Mass transport can be decoupled from kinetics with large semiconductor electrodes through construction of rotating disk electrodes (RDEs).[49, 50] Under defined convection, kinetic parameters can be determined, and high current densities can be obtained.[51, 52] Similarly, a rotating ring disk electrode (RRDE) can be employed to examine the redox activity of the reaction product, providing additional mechanistic and rate information.[53, 54] However, for bulk semiconductor materials, these motifs are extremely cumbersome to fabricate and require ultra-smooth surfaces for correct interpretation of convective aspects. As such, their use in semiconductor electrochemistry has been limited.

Ultramicroelectrodes (UMEs) are electrodes that have radii less than ~25 μm, commonly fabricated by sealing a metal/carbon filament within an insulating sheath.[55] Even smaller UMEs can be obtained by heating and pulling the metal/insulator construct to a defined size.[55-57] Their small size provides several unique advantages over macroelectrodes in terms of electrochemical analysis. First, the measured currents are typically in the nA range or less. As such, the ohmic drop using small electrodes are negligible, even in highly resistive solutions. Second, radial diffusion is predominantly operative at UMEs, compared to linear diffusion profiles at larger electrodes. This leads to current densities several orders of magnitude larger than stationary and rotating macroelectrodes.[52, 55-57] Additionally, the relationship between kinetics and radial diffusion at a UME is well defined and the full voltammetric response can be fit to relevant kinetic and thermodynamic parameters.[58, 59]

The UME geometry has been exploited to study charge transfer at semiconductors in two fashions. A general depiction of these two motifs is shown in Figure 1.5. Scanning electrochemical microscopy (SECM) (Figure 1.5a) involves scanning a metal UME tip across a surface, where the observed current at the UME is proportional to distance from the substrate and the electrochemical kinetics.[60, 61] This method has been used in multiple studies to probe

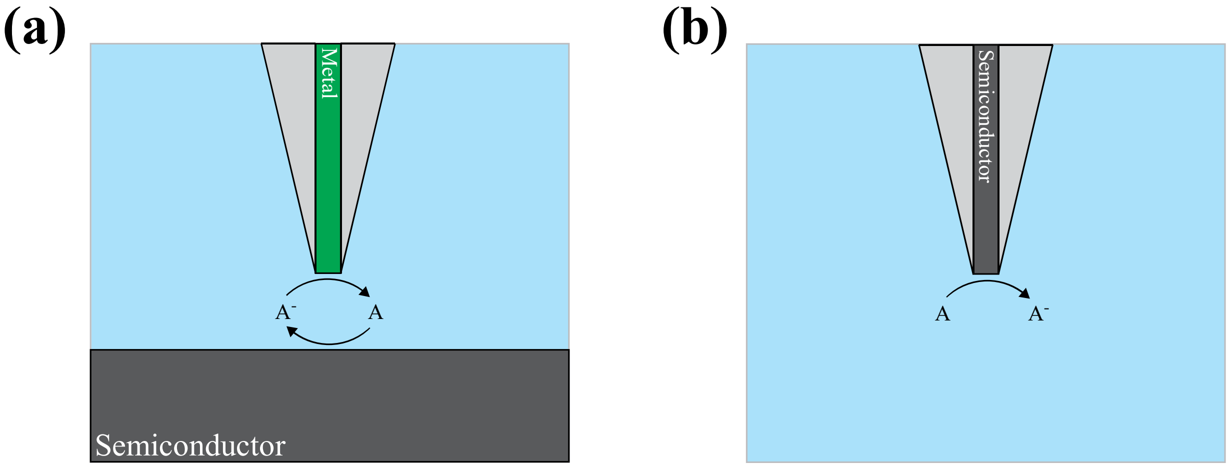

Figure 1.5. Existing methods for UME analysis of semiconductor electrodes: (a) SECM with a metal UME tip and (b) semiconductor filament sealed in an insulating sheath.

local corrosion processes at semiconductor surfaces.[62, 63] Several aspects limit SECM for charge transfer studies. First, any slight change in the surface roughness will convolute the UME tip current. Relatedly, non-faradaic processes such as corrosion or surface oxidation will ambiguously alter the feedback response. Second, the feedback current is not directly associated with the unique energetics of the semiconductor substrate. That is, it is challenging to directly probe driving force – rate constant relationships. An alternative method is to replace the metal filament in traditional UMEs with a semiconductor rod or wire (Figure 1.5b).[64] However, most semiconductor materials are not available in wire form at that size scale and it is unclear how the current response would be affected when the depletion width extends to the wire/insulator boundary. In this regard, devising a UME geometry with bulk semiconductor wafers as the substrate would be useful as an accurate and precise measurement technique in semiconductor electrochemistry.

Intent of Thesis

The intent of this thesis is two-fold. First, a new semiconductor electroanalytical platform will be introduced and a framework for analyzing its voltammetric response will be detailed. Importantly, this work will be placed in context with previous methods for examining charge transfer at semiconductor/liquid contacts. Second, electrodeposition of dual-functional protective layers on III-V semiconductor photoelectrodes will be demonstrated. Comparison of device performance metrics to protective layers fabricated by other techniques will highlight the advantages of using the methods described herein.

1.3. Content Description

Chapter 2 describes the error associated with electrochemical measurements at recessed disk metallic ultramicroelectrodes (UMEs) using inlaid disk-specific diffusion models. Finite element simulations of UMEs with varying radii and recession depths were analyzed with extant analytical expressions for radial diffusion to assess error magnitudes for the heterogeneous charge transfer rate constant and transfer coefficient as a function of increasing recession depth and decreasing electrode radius. Recessed Pt UMEs that were fabricated through photolithography confirmed the simulations results for both fast and slow outer-sphere redox processes. Cumulatively, the data in this chapter shows that errors in kinetic parameters due electrode recession can be large, but are predictable based on the UME geometry.

Chapter 3 demonstrates the fabrication of semiconductor ultramicroelectrodes (SUMEs) and their use for voltammetric analysis of charge transfer processes at semiconductor/liquid contacts. n-Si SUMEs were prepared by photolithographic patterning of defined pinholes in dielectric coatings on semiconductor wafers. Methods are reported for interpreting their electrochemical response characteristics in the absence of illumination. Radial diffusion is reconciled with the diode equation to describe the full voltammetric response, allowing direct determination of heterogenous charge-transfer rate constants and surface quality. The voltammetric responses of n-type Si SUMEs were assessed and showed prototypical UME characteristics with higher obtainable current densities than conventional macroscopic electrodes. The SUME voltammetry proved highly sensitive to both native and intentionally-grown oxides highlighting their ability to precisely track dynamic surface conditions reliably through electrochemical measurement. Subsequently, electron transfer from the conduction band of n-Si SUMEs to aqueous $Ru(NH_3)_6^{3+}$ was determined to occur near optimal exoergicity. In total, this work validates the SUME platform as a new tool to study fundamental charge-transfer properties at semiconductor/liquid junctions.

Chapter 4 provides a framework for how to interpret and predict the steady-state voltammetric responses of SUMEs. Through consideration of the Marcus-Gerischer treatment for heterogeneous charge transfer, as well as addressing the interplay between the fractions of the applied potential that drop across the space-charge region, the solution, and their interface, the complex potential dependences of the majority carrier densities, n_s, and the rate constant for electron transfer from the conduction band edge, k_{et}, are identified. Incorporation of these terms into a defined expression describing the interplay between mass transport and kinetic control at inlaid disc electrodes affords determination of the full J-E responses of n-type SUMEs for the 1e- reduction of outer-sphere species in a variety of experimental configurations and spanning both depletion and accumulation conditions within the semiconductor. Working curves are presented to illustrate how the conduction band edge potential, the reorganization energy for charge transfer, the standard potential of the redox species, the doping density, and the ionic strength of the electrolyte influence data in the case of a pristine semiconductor/electrolyte interface. Further, working curves are provided to examine the expected influence of surface states on the shape and position of the steady-state J-E responses. An example of how to analyze experimental data without the use of 'non-ideality' factors so as to gain full insight on the physicochemical and electrochemical parameters of the system is shown. In total, this work provides a clear guide on how to utilize simple, raw voltammetric data from SUMEs to study semiconductor/electrolyte contacts of interest.

Chapter 5 describes the direct photoelectrodeposition of catalytic MoS_x thin films on $GaInP_2$ photocathodes for stable photoelectrochemical hydrogen generation. Specifically, the MoS_x deposition conditions were controlled to obtain 8-10 nm films directly on p-$GaInP_2$ substrates without ancillary protective layers. The films were nominally composed of MoS_2, with additional MoO_xS_y and MoO_3 species detected, and showed no long-range crystalline order. The as-deposited material showed excellent catalytic activity towards the hydrogen evolution reaction relative to bare p-$GaInP_2$. Notably, no appreciable photocurrent reduction was incurred by the addition of the photoelectrodeposited MoS_x catalyst to the $GaInP_2$ photocathode under light-limited operating conditions, highlighting the advantageous optical properties of the film. The MoS_x catalyst also imparted enhanced durability towards photoelectrochemical hydrogen evolution in acidic conditions, maintaining nearly 85% of the initial photocurrent after 50 hours of electrolysis. In total, this work demonstrates a simple method for producing dual-function catalyst/protective layers directly on high performance, planar III-V photoelectrodes for photoelectrochemical energy conversion.

Chapter 6 summarizes the conclusions of this thesis along with describing several research topics that merit further exploration based on the results of this work. First, the expansion of the SUME platform to alternative semiconductor substrates and smaller size scales will be discussed. Specifically, the challenges associated with the fabrication and experimental utilization of n-GaP and n-GaN SUMEs will be detailed. Preliminary measurements with these SUMEs will also be shown. Motivation for voltammetric analysis of charge transfer at <100 nm SUMEs be described. Second, electrodeposition of Fe-doped NiOOH on nanoporous GaP photoanodes for photoelectrochemical water-splitting will be discussed. Control over the porosity through electrochemical etching will be demonstrated and deposition conditions necessary to obtain uniform catalyst coverage throughout the pore depth will be described. Finally, marriage of the two separate research directions presented in this thesis will be proposed in the form of SUME arrays for photoelectrochemical water-splitting. Prospects for enhancement of photovoltage and photocurrent through array design will be presented. Initial experiments describing the size dependence on the onset potential and light-limited photocurrent will be shown.

1.4. References

1. Lewis, N. S. *Science* **2016,** *351*, 353.

2. Armstrong, R. C.; Wolfram, C.; de Jong, K. P.; Gross, R.; Lewis, N. S.; Boardman, B.; Ragauskas, A. J.; Ehrhardt-Martinez, K.; Crabtree, G.; Ramana, M. V. *Nat. Energy* **2016,** *1,* 1.

3. Kamat, P. V. *J. Phys. Chem. C* **2007,** *111*, 2834.

4. *Solar Hydrogen Generation Toward a Renewable Energy Future*. 1 ed.; Spring-Verlag: New York, 2008.

5. Jia, J. Y.; Seitz, L. C.; Benck, J. D.; Huo, Y. J.; Chen, Y. S.; Ng, J. W. D.; Bilir, T.; Harris, J. S.; Jaramillo, T. F. *Nat. Commun.* **2016,** *7,* 13237.

6. Shaner, M. R.; Atwater, H. A.; Lewis, N. S.; McFarland, E. W. *Energ. Environ. Sci.* **2016,** *9*, 2354.

7. Abbasi, T.; Abbasi, S. A. *Renew. Sust. Energ. Rev.* **2011,** *15*, 3034.

8. Turner, J.; Sverdrup, G.; Mann, M. K.; Maness, P. C.; Kroposki, B.; Ghirardi, M.; Evans, R. J.; Blake, D. *Int. J. Energ. Res.* **2008,** *32*, 379.

9. Nowotny, J.; Sorrell, C. C.; Sheppard, L. R.; Bak, T. *Int. J. Hydrogen Energ.* **2005,** *30*, 521.

10. Balat, M. *Int. J. Hydrogen Energ.* **2008,** *33*, 4013.

11. Gratzel, M. *Nature* **2001,** *414*, 338.

12. Nozik, A. J. *Annu. Rev. Phys. Chem.* **1978,** *29*, 189.

13. Kornienko, N.; Gibson, N. A.; Zhang, H.; Eaton, S. W.; Yu, Y.; Aloni, S.; Leone, S. R.; Yang, P. D. *ACS Nano* **2016,** *10*, 5525.

14. Sivula, K.; van de Krol, R. *Nat. Rev. Mater.* **2016,** *1* (2).

15. Fujishima, A.; Honda, K. *Nature* **1972,** *238*, 37.

16. Young, J. L.; Steiner, M. A.; Doscher, H.; France, R. M.; Turner, J. A.; Deutsch, T. G., *Nat. Energy* **2017,** *2* (4).

17. Cheng, W. H.; Richter, M. H.; May, M. M.; Ohlmann, J.; Lackner, D.; Dimroth, F.; Hannappel, T.; Atwater, H. A.; Lewerenz, H. J. *ACS Energy Lett.* **2018,** *3*, 1795.

18. Khaselev, O.; Turner, J. A. *Science* **1998,** *280*, 425.

19. May, M. M.; Lewerenz, H. J.; Lackner, D.; Dimroth, F.; Hannappel, T. *Nat. Commun.* **2015,** *6*.

20. Walter, M. G.; Warren, E. L.; McKone, J. R.; Boettcher, S. W.; Mi, Q. X.; Santori, E. A.; Lewis, N. S. *Chem. Rev.* **2010,** *110*, 6446.

21. Hu, S.; Shaner, M. R.; Beardslee, J. A.; Lichterman, M.; Brunschwig, B. S.; Lewis, N. S. *Science* **2014,** *344*, 1005.

22. Gu, J.; Aguiar, J. A.; Ferrere, S.; Steirer, K. X.; Yan, Y.; Xiao, C. X.; Young, J. L.; Al-Jassim, M.; Neale, N. R.; Turner, J. A. *Nat. Energy* **2017,** *2* (2).

23. Fajardo, A. M.; Lewis, N. S. *J. Phys. Chem. B* **1997,** *101*, 11136.

24. Farjardo, A. M.; Lewis, N. S. *Science* **1996,** *274*, 969.

25. Hamann, T. W.; Gstrein, F.; Brunschwig, B. S.; Lewis, N. S. *J. Am. Chem. Soc.* **2005,** *127*, 7815.

26. Hamann, T. W.; Gstrein, F.; Brunschwig, B. S.; Lewis, N. S. *Chem. Phys.* **2006,** *326*, 15.

27. Royea, W. J.; Fajardo, A. M.; Lewis, N. S. *J. Phys. Chem. B* **1997,** *101*, 11152.

28. Marcus, R. A. *J. Chem. Phys.* **1965,** *43*, 679.

29. Siders, P.; Marcus, R. A. *J. Am. Chem. Soc.* **1981,** *103*, 748.

30. Morrison, S. R. *Surf. Sci.* **1969,** *15*, 363.

31. Miller, J. R.; Beitz, J. V.; Huddleston, R. K. *J. Am. Chem. Soc.* **1984,** *106*, 5057.

32. Closs, G. L.; Miller, J. R. *Science* **1988,** *240*, 440.

33. Fukuzumi, S.; Ohkubo, K.; Suenobu, T. *Acc. Chem. Res.* **2014,** *47*, 1455.

34. Irvine, M. P.; Harrison, R. J.; Beddard, G. S.; Leighton, P.; Sanders, J. K. M. *Chem. Phys.* **1986,** *104*, 315.

35. Wasielewski, M. R.; Niemczyk, M. P.; Svec, W. A.; Pewitt, E. B. *J. Am. Chem. Soc.* **1985,** *107*, 1080.

36. Hamann, T. W.; Gstrein, F.; Brunschwig, B. S.; Lewis, N. S. *J. Am. Chem. Soc.* **2005,** *127*, 13949.

37. Vanden Berghe, R. A. L.; Cardon, F.; Gomes, W. P. *Surf. Sci.* **1973,** *39*, 368.

38. Gerischer, H. *Electrochim. Acta* **1990,** *35*, 1677.

39. Gerischer, H. *J. Vac. Sci. Technol.* **1978,** *15*, 1422.

40. Gerischer, H. *Surf. Sci.* **1969,** *18*, 97.

41. Frese, K. W.; Madou, M. J.; Morrison, S. R. *J. Phys. Chem.* **1980,** *84*, 3172.

42. Brown, E. S.; Peczonczyk, S. L.; Wang, Z. J.; Maldonado, S. *J. Phys. Chem. C* **2014,** *118*, 11593.

43. Lancaster, M.; Mow, R.; Liu, J.; Cheek, Q. T.; MacInnes, M. M.; Al-Jassim, M. M.; Deutsch, T. G.; Young, J. L.; Maldonado, S. *ACS Appl. Mater. Interfaces* **2019,** *11*, 25115.

44. Memming, R.; Schwandt, G. *Electrochim. Acta* **1968,** *13*, 1299.

45. Pomykal, K. E.; Lewis, N. S. *J. Phys. Chem. B* **1997,** *101*, 2476.

46. Santangelo, P. G.; Lieberman, M.; Lewis, N. S. *J. Phys. Chem. B* **1998,** *102*, 4731.

47. Bard, A.; Faulkner, L., *Electrochemical Methods: Fundamentals and Applications*. 2nd ed.; John Wiley & Sons: New York, 2001.

48. Nicholson, R. S.; Shain, I. *Anal. Chem.* **1964,** *36*, 706.

49. Watts, D. K.; Koval, C. A. *J. Phys. Chem.* **1996,** *100*, 550.

50. Siemoneit, K.; Reineke-Koch, R.; Meier, A.; Memming, R. *Electrochim. Acta* **2000,** *45*, 4577.

51. Levich, V. G., *Physicochemical Hydrodynamics*. Prentice-Hall: Englewood Cliffs, NJ, 1962.

52. Bard, A. J.; Faulkner, L. R., *Electrochemical Methods: Fundamentals and Applications*. 2nd ed.; John Wiley & Sons, Inc.: Hoboken, NJ, 2001.

53. Miller, B.; Menezes, S.; Heller, A. *J. Electroanal. Chem.* **1978,** *94*, 85.

54. Hirano, K.; Bard, A. J. *J. Electrochem. So.c* **1980,** *127*, 1056.

55. Zoski, C. G. *Electroanalysis* **2002,** *14*, 1041.

56. Li, Y. X.; Bergman, D.; Zhang, B. *Anal. Chem.* **2009,** *81*, 5496.

57. Sun, P.; Mirkin, M. V. *Anal. Chem.* **2006,** *78*, 6526.

58. Bond, A. M.; Oldham, K. B.; Zoski, C. G. *J. Electrochem. Soc.* **1988,** *135*, 71.

59. Oldham, K. B.; Myland, J. C.; Zoski, C. G.; Bond, A. M. *J. Electroanal. Chem.* **1989,** *270*, 79.

60. Kwak, J.; Bard, A. J. *Anal. Chem.* **1989,** *61*, 1221.

61. Bard, A. J.; Fan, F. R. F.; Kwak, J.; Lev, O. *Anal. Chem.* **1989,** *61*, 132.

62. Park, H. S.; Leonard, K. C.; Bard, A. J. *J. Phys. Chem. C* **2013,** *117*, 12093.

63. Horrocks, B. R.; Mirkin, M. V.; Bard, A. J. *J. Phys. Chem.* **1994,** *98*, 9106.

64. Rodman, S.; Spitler, M. T. *J. Phys. Chem. B* **2000,** *8*, 9438.

CHAPTER 2

Inlaid Disk Approximation of Electron Transfer Kinetics at Recessed Disk Ultramicroelectrodes

2.1. Introduction

Measurement of charge transfer rates at electrode/electrolyte interfaces is key for describing processes that underpin sensing[1-2] and energy conversion technologies[3-4] as well as investigating fundamental electron transfer theories.[5-7] At inlaid disk-shaped ultramicroelectrodes (UMEs) and nanoelectrodes, radial diffusion and efficient mass-transport conditions have enabled measurements of fast electron-transfer kinetics and associated mechanisms.[8-11] This is simplified through the knowledge of an analytical expression for the full steady-state response of an inlaid disk UME which can be used to fit experimental results for the heterogeneous electron transfer rate constant, k_{et}, and the transfer coefficient, α_{et}.[12-14] For example, the facile fabrication of inlaid-disk electrodes through laser-pulling,[12, 15] electrochemical etching,[16] or a combination of the two,[17] have resulted in electrodes on the scale of several nanometers. The mass-transfer coefficients of these types of platforms are sufficiently large to record heterogeneous rate constant values in excess of 30 cm/s.[10] The necessary requirements for UMEs fabricated in these fashions include availability in filamented form factors, melting points compatible with instrument heat sources and desired insulating materials, and/or the ability to electrochemically corrode. Metals such as platinum and gold fit these requirements well, and as such have been most commonly used for kinetics studies.

In contrast to inlaid-disk electrodes, recessed UMEs can be readily fabricated with essentially any bulk substrate material through common photolithographic techniques.[18] While this type of geometry is typically exploited in an array fashion for electrochemical sensing,[19-20] use of an individual recessed electrode for application to kinetic measurements is limited. Theoretical and experimental examinations of the diffusion-limited (steady-state) current for recessed-disk electrodes of various geometries have been conducted, and the voltammetric response has been simulated, but an encompassing analytical expression describing geometry-specific behavior has not been presented.[21-22] This is partially due to difficulty reconciling transport conditions within the well to flux conditions at the mouth of the recession for the near-infinite possible recessed electrode shapes.[23-24]

A more tractable alternative to analyzing charge transfer kinetics at recessed electrodes is through evaluation of the error in using the inlaid disk diffusion model for recessed-disk geometries. Although it is well known that rate constants are typically overestimated at small, recessed electrodes,[25-26] the specific uncertainties associated with relevant experimental and fabrication parameters have not been defined. Such a description would bridge the gap between recessed electrodes' ease of fabrication and ability to make accurate kinetic measurements. Herein, a systematic analysis of the error in the heterogeneous charge transfer rate constant and transfer coefficient measured at recessed disk UMEs is provided relative to an inlaid disk diffusion model. Specifically, finite-element simulations for various recession depths, electrode radii, and rate constants are analyzed to assess key parameter uncertainties as a function of UME geometry. Additionally, experimental measurement of charge transfer rate constants at several UME recession depths are compared to an inlaid UME to verify simulation results.

2.2. Experimental

Simulations

COMSOL Multiphysics (v4.4) was used to simulate the transport and electron transfer of freely-diffusing redox species to and from the electrode surface in the stationary UME geometry shown in Figure 2.1a. A time-independent model was employed to remove capacitive contributions from the dielectric layer. This is generally applicable to experimental systems at sufficiently slow scan rates. In this work the electrode radius, *r*, was set at either 50, 5, or 0.5 μm. For each electrode size, the recession depth, *d*, was varied between 0-10 μm. Only diffusion-controlled transport was considered, as an unstirred solution with a large concentration of supporting electrolyte was assumed. Relevant parameters and constants are shown in Table 2.1.

The voltammetric responses of inlaid and recessed UMEs are simulated for a one-electron oxidation process as shown in *eq. 2.1*.

$$A^{-} \rightarrow A + e^{-} \qquad (2.1)$$

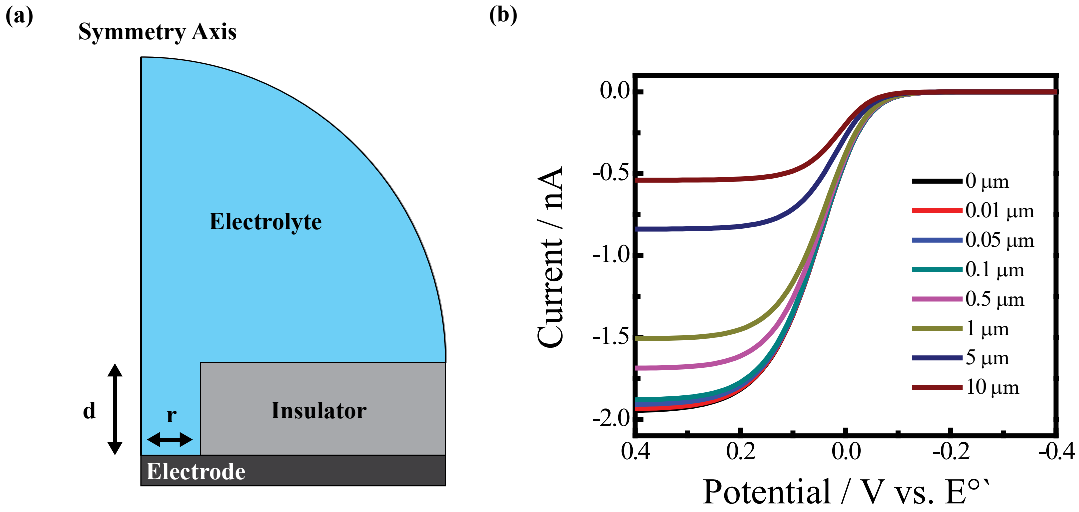

Figure 2.1. (a) Two-dimensional geometric model for the recessed-disk UME simulation. *d* represents the recession depth and *r* denotes the electrode radius. The hemispherical electrolyte boundary is not drawn to scale. (b) Simulated voltammetric response for a one-electron oxidation process using 5 µm inlaid and recessed UMEs with recession depths of 0-10 µm. In this simulation, k_{et} = 0.01 cm s^{-1}, α_{et} = 0.5, $[A^*]$ = 0.001 M, and D_A and D_{A-} = 1 x 10^{-5} cm^2 s^{-1}.

Table 2.1. Relevant parameters for finite element simulations

Symbol	Definition	Simulation Value
d	Recession Depth	0-10 µm
r	Electrode Radius	0.5, 5, or 10 µm
$[A^*]$	Bulk Concentration of Oxidized Species	1 mM
$E°`$	Standard/Formal Potential	0 V vs. Reference
D_A	Oxidized Species Diffusion Coefficient	$1\text{x}10^{-5}$ cm^2 s^{-1}
D_{A-}	Reduced Species Diffusion Coefficient	$1\text{x}10^{-5}$ cm^2 s^{-1}
T	Temperature	298 K

The forward and reverse heterogeneous rate constants, k_f and k_b, respectively, are described through by Butler-Volmer kinetics[12] in *eqs. 2.2* and *2.3*

$$k_f = k_{et} e^{\frac{-\alpha_{et} F (E_{applied} - E^{\circ`})}{RT}} \tag{2.2}$$

$$k_b = k_{et} e^{\frac{(1-\alpha_{et}) F (E_{applied} - E^{\circ`})}{RT}} \tag{2.3}$$

where k_{et} is the standard heterogeneous rate constant, α_{et} is the transfer coefficient, F is the Faraday constant, R is the molar gas constant, T is the temperature, $E_{applied}$ is the applied potential, and $E^{\circ`}$ is the formal/standard potential. Diffusion in this system can be described through Fick's second law in two-dimensional cylindrical coordinates by *eq. 2.4*,

$$\frac{\partial [A^-]}{\partial t} = D_{A^-} \left(\frac{\partial^2 [A^-]}{\partial a^2} + \frac{1}{a} \frac{\partial [A^-]}{\partial a} + \frac{\partial^2 [A^-]}{\partial z^2} \right) \tag{2.4}$$

where $[A^-]$ is the concentration of the reduced form of the redox couple, t is time, a is the direction radial from the electrode surface, and z is the direction normal to the electrode surface. The boundary conditions are as follows. Initially, the concentration of the reduced form of the redox couple is equivalent to the bulk concentration, $[A^*]$, and the oxidized form of the redox couple, $[A]$, is not present, as shown in *eqs. 2.5* and *2.6*.

$$[A^-] = [A^*] \tag{2.5}$$

$$[A] = 0 \tag{2.6}$$

These conditions hold throughout the model geometry. An semi-infinite domain was used at the electrolyte boundary where $[A^-]$ approaches $[A^*]$ at all times. Once a bias is applied to the electrode and a concentration gradient forms, the flux of the oxidized and reduced species can be descried through *eq. 2.7*,

$$D_A \left(\frac{\partial [A]}{\partial t} \right) = -D_{A^-} \left(\frac{\partial [A^-]}{\partial t} \right) \tag{2.7}$$

where D_A and D_{A-} are the diffusion coefficients of the oxidized and reduced forms of the redox species present in solution, respectively. The flux to all insulator/electrolyte boundaries is zero and described by *eq. 2.8*.

$$D_{A^-}\left(\frac{\partial[A^-]}{\partial t}\right)=0 \tag{2.8}$$

A Butler-Volmer formalism can be used to describe the current, *I*, at all points on the electrodes surface through *eq. 2.9*,

$$D_{A^-}\left(\frac{\partial[A^-]}{\partial t}\right)=k_f[A^-]-k_b[A]=\frac{I}{FA} \tag{2.9}$$

with the other variables as defined above. Because the disk shape may have non-uniform accessibility depending on the geometry, the current is integrated over the entirety of the electrode to obtain the total current passed across the interface via *eq. 2.10*.

$$I_{tot}=2\pi FD_{A^-}\int_0^r\frac{\partial[A^-]}{\partial t}rdr \tag{2.10}$$

To accurately resolve the concentration gradients near the electrode surface and insulator boundaries, a custom, fine mesh was used. The simulated voltammograms for a 5 µm UME with varying recession depths is shown in Figure 2.1b. Absolute mass-transport limited currents of the simulated voltammograms for electrodes with no recession were within 1% of the Cottrell prediction for all simulations in this work.

Fitting

The voltammetric response of an inlaid disk electrode for a quasi-reversible redox system has been described by the classical "Bond-Oldham-Zoski" equation[13] (*eq. 2.11*)

$$\frac{J}{J_{L,a}}=\left[1+\frac{\pi}{\kappa\theta}\left(\frac{2\kappa\pi+3\pi}{4\kappa\pi+3\pi^2}\right)\right]^{-1} \tag{2.11}$$

where J is the current density and $J_{L,a}$ is the mass-transport limited current density at large positive overpotentials for an oxidation reaction. The parameterized terms κ and θ relate kinetics and transport through *eqs. 2.12* and *2.13*

$$\theta=1+\frac{D_A k_b}{D_{A^-}k_f} \tag{2.12}$$

$$\kappa=\frac{\pi k_f}{4D_{A^-}} \tag{2.13}$$

where k_f and k_b have the same meaning as in *eqs. 2.2* and *2.3*. This formalism has been a common means to fit the entire voltammetric response of a metallic inlaid disk UME for direct determination of the heterogeneous rate constants and transfer coefficients. A recent modification to *eq. 2.11* has been made to account for poised solutions,[12] eliminating $E°`$ as an unknown variable. Here, it is assumed the standard/formal potential is known (Table 2.1).

Chemicals and Materials

Ferrocenemethanol (FcMeOH, 97%, Sigma-Aldrich), iron (II) sulfate heptahydrate ($Fe^{2/3+}$, 99+%, Acros), potassium sulfate (K_2SO_4, 99+%, Acros), potassium chloride (KCl, 99.5%, Fisher), acetone (ACS grade, Fisher), 2-propanol (ACS grade, Fisher), buffered hydrofluoric acid (BHF, Transene), Nano-strip (Cyantek® KMG 539400 Nano-Strip 2X®), Microposit S1813 photoresist (Shipley) and Megaposit SPR 220 3.0 photoresist (Microchem) were used as received. Degenerately doped n-type Si(111) 4 in. wafers (0.525 mm, ρ=0.003 Ω·cm were purchased from MTI Corp and used as the substrates for the recessed Pt and n^+-Si UMEs.

Recessed Electrode Fabrication

The fabrication process for n^+-Si SUMEs has been described previously.[27] Recessed- and inlaid-disk Pt UMEs were prepared via a slightly modified method. Silicon oxide (SiO_2) was deposited on the wafer substrates by plasma-enhanced chemical vapor deposition (Ultradep 2000, GSI Lumonics) at a deposition rate of ~20 nm min^{-1} and T = 350 °C and subsequently annealed at 800 °C in N_2 for 5 min (Jetfirst RTP 150, Jipelec). For the 0 µm and 0.5 µm recession, 0.6 µm of SiO_2 was deposited. For the 2.4 µm recession, 2.5 µm SiO_2 was deposited. The wafers were then coated with hexamethyldisilazane (HMDS) and SPR 220 3.0 photoresist and soft baked for 90 seconds at T = 115 °C. A custom mask with 5 µm features was used for exposure of the substrates through projection photolithography (GCA Autostep 200, RZ Enterprises, Inc., 365 nm). Reactive ion etching (RIE, APS Dielectric Etch Tool, STS) was then used to transfer the pattern in the SiO_2 layer using C_4F_8 (g). E-beam evaporation (Evovac, Angstrom Engineering) was then used to deposit a 10 nm Ti adhesion layer followed by Pt to produce the desired recession depth. The wafers were diced into dies and acetone and 2-propanol was used to remove the photoresist before use.

Electrochemical Measurements

All voltammetric experiments were conducted with a CHI420A potentiostat in a home-built Faraday cage. Recessed UMEs were placed in an open-air Teflon cell and sealed with a Viton o-ring (ID = 2.9 mm, McMaster-Carr). Measurements were made utilizing a three-electrode configuration with a Ag/AgCl (Sat'd KCl) reference electrode and a Pt wire counter electrode.

Electrode Characterization

Scanning electron microscope (SEM) images were acquired with a Hitachi SU8000 In-Line SEM equipped with a cold cathode field emission source and a secondary electron detector. Images were acquired at accelerating voltages of 10 or 15 kV.

2.3. Results

Figure 2.2 shows the simulated voltammetric responses of 50, 5, and 0.5 µm radius UMEs with recession depths between 0 µm and 10 µm and rate constants of 1 cm s^{-1}, 0.01 cm s^{-1}, and 1 x 10^{-5} cm s^{-1} and transfer coefficients of 0.5. These values were chosen to roughly approximate reversible, quasi-reversible, and near-irreversible electron transfer kinetics, respectively, over the range the radii simulated in this work. For a 50 µm radius UME at k_{et} = 1 cm s^{-1} in Figure 2.2a, the shape of the normalized response is completely insensitive to the recession depth to electrode radius ratio, d/r. As the rate constant decreases, slight deviations from the inlaid disk case ($d/r = 0$) become apparent, especially for k_{et} = 1 x 10^{-5} cm s^{-1}. For this rate constant, the half-wave potential, $E_{1/2}$, for the quasi-reversible case is shifted to slightly more negative potential from the reversible system, and as the d/r ratio increases, the curves become increasingly more negative with steeper slopes.

For a smaller electrode radius of 5 µm shown in Figure 2.2b, a similar trend is observed. For reversible redox processes, the curve position and shape changes little as a function of recession depth. However, this small change in slope is still more significant than for the larger 50 µm UME. As k_{et} slows, deviation from the inlaid disk case becomes more pronounced as the recession depth increases. Specifically, an overall shift in the voltammetric response to higher overpotentials is noted. The $E_{1/2}$ shifts for both sets of curves moves more positive with an increase in recession depth, although this manifests as a steeper curve at 0.1 cm s^{-1} and a shift in the current onset at 1x10^{-5} cm s^{-1}.

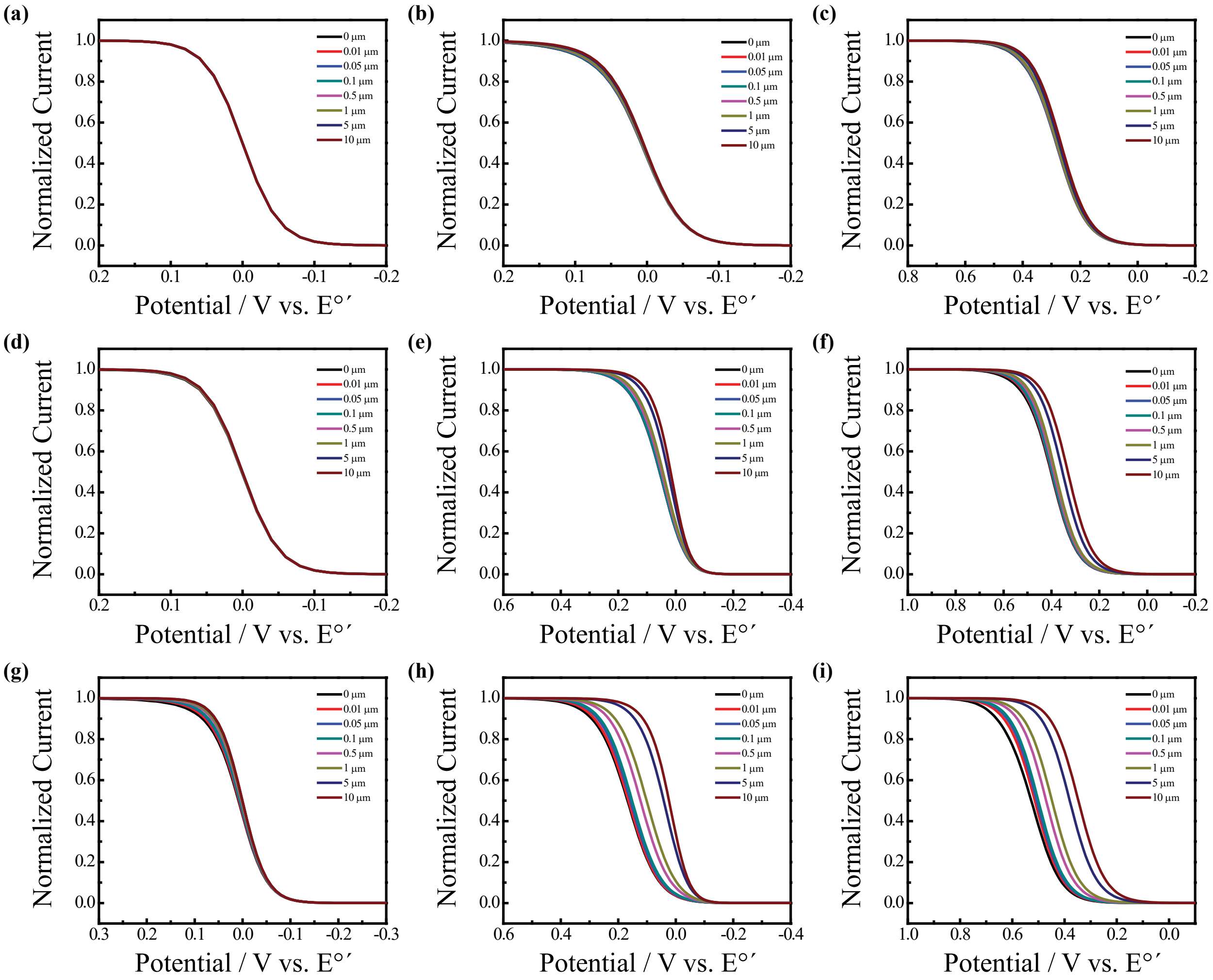

Figure 2.2. Normalized simulation voltammetric responses for (a,b,c) 50 µm, (d,e,f) 5 µm, and (g,h,i) 0.5 µm disk UMEs with recession depths of 0-10 µm. The simulated heterogeneous rate constants, k_{et}, were (a,d,g) 1 cm s^{-1}, (b,e,h) 0.01 cm s^{-1}, and (c,f,i) 0.00001 cm s^{-1}. For these simulations, the transfer coefficient, α_{et}, was 0.5.

At the smallest simulated electrode radius of 0.5 μm depicted in Figure 2.2c, slightly different behavior is observed. Unlike the results for larger electrodes in Figure 2.2a and 2.2b, the simulated response for a reversible reaction at a 0.5 μm UME shows a clear dependence on the recession depth. In this case, there is a slight shift of the curves to a more negative $E_{1/2}$ for all recession depths with an increase in slope with larger d/r. For rate constants of 0.1 cm s^{-1}, the shift of the curves as a function of recession depth is similar in direction to the responses of larger electrodes, but with much larger deviation in $E_{1/2}$ and more significant curve steepness with increasing d/r ratios. Similar results are observed for the simulated irreversible case. At $d = 0$, $E_{1/2}$ is shifted significantly negative but becomes more positive with increasing recession depth.

To assess the accuracy of the rate constant determinations with recessed UMEs, the voltammetric responses presented in Figure 2.2 were fit to *eq. 2.11*. The apparent rate constant from the fit results, k_{fit}, was compared to the input rate constant for the simulations, k_{et}, as a function of d/r. The results are highlighted in Figure 2.3a at all UME sizes with small recession depths and $k_{et} = 0.1$ cm s^{-1}. For $d/r = 0$, the ratio of rate constants was essentially 1, indicating no appreciable error in the fitted value relative to "true" rate constant. As d increases, k_{fit}/k_{et} rises in a non-linear fashion at low d/r before growing linearly at larger recession depths. The error tracks with electrode size, as increasing the electrode size results in largely enhanced k_{fit}/k_{et} values. For the slower charge transfer process of $k_{et} = 1 \times 10^{-5}$ cm s^{-1} as shown in Figure 2.3b, a markedly different trend was observed. For $d/r = 0$, the 0.5 μm recession shows the largest k_{fit}/k_{et} ratio. As d/r increases, k_{fit}/k_{et} decreases to a minimum value before starting to rise again. Interestingly, the k_{fit}/k_{et} values suggest rate constant underestimation with increasing electrode recession.

A similar comparison between simulated and fitted transfer coefficients (α_{et} and α_{fit}, respectively) is shown in Figure 2.4 for 5 and 0.5 μm radius electrodes. For the range of transfer coefficients explored, a consistent trend was observed with increasing d/r. At $d/r = 0$, a slight error of ~1% is observed between fitted and simulated values. Once a finite amount of recession is present, the deviation sharply rises. Further increases in the recession depth result in the error leveling out. Notably, this plateau of occurs at approximately the same value for all α_{et}.

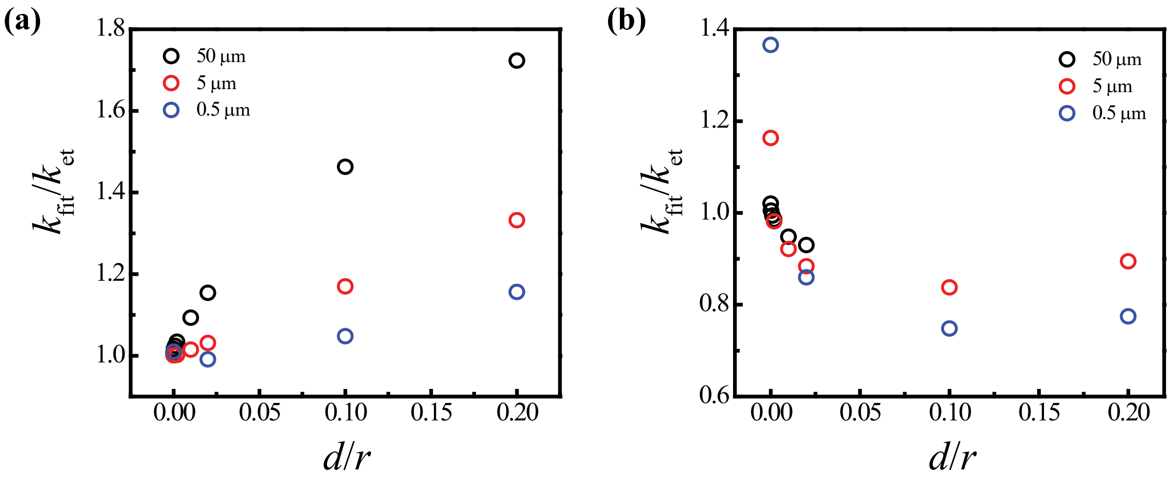

Figure 2.3. Deviation of fitted rate constant values (k_{fit}) from simulated values of (a) k_{et} = 0.01 cm s^{-1} and (b) k_{et} = 0.00001 cm s^{-1} for 50, 5, and 5 μm UMEs with d/r = 0 – 0.2.

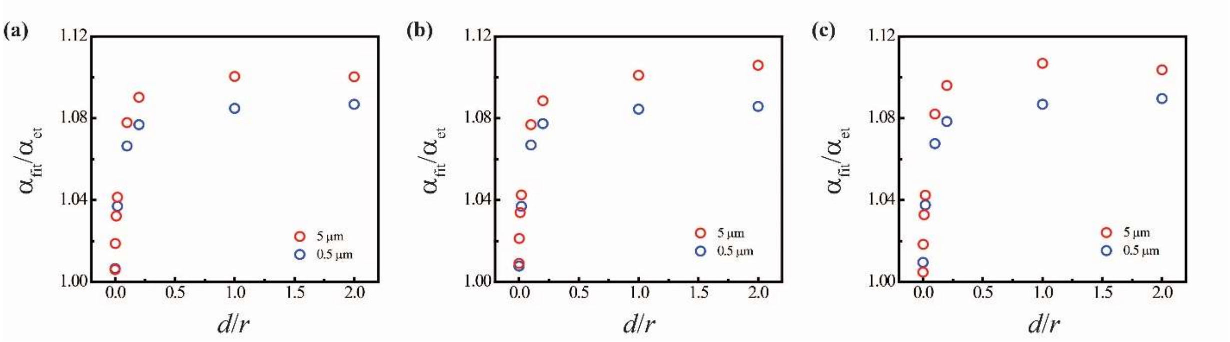

Figure 2.4. Deviation of the fitted transfer coefficient (α_{et}) from simulated values of (a) $\alpha_{et} = 0.25$, (b) $\alpha_{et} = 0.5$, and (c) $\alpha_{et} = 0.75$ for 5 and 0.5 µm UMEs with recession depths of 0 – 2.0.

Experimental voltammograms were acquired with inlaid- and recessed-disk Pt UMEs with 5 µm radii. Representative top-down and cross-section SEM images are shown in Figure 2.5a. A well-defined circular region contain the Pt electrode material is exposed to solution, with the insulator lip rising above the electrode plane for recessed disks. Pt appears to fill the well uniformly, even though some surface roughness is observed. Figure 2.5b compares the catalytic activity of the Pt-filled and bare n^+-Si UMEs in 0.5 M KCl. Both UME electrodes exhibit a slow rise in current attributable to O_2 reduction before a sharp current increase associated with proton reduction. For the Pt UME, this onset occurs over 1 V more positive than that of n^+-Si, highlighting the fabrication process for Pt UMEs employed here yields the expected, active Pt electrode behavior.

Figure 2.6 shows the experimental voltammograms of 5 µm inlaid- and recessed-disk Pt UMEs in contact with 1 mM FcMeOH and 2 mM $Fe(SO_4)$. FcMeOH is known to undergo a relatively facile charge transfer process,[28] while the $Fe^{2/3+}$ redox couple is more sluggish.[29] This fact is clearly evidenced in Figure 2.6a and 2.6b, where the FcMeOH response exhibits a much sharper transition to a mass transfer-limited value. Additionally, the inlaid and recessed limiting currents for both redox couples track well with predictions from the modified Cottrell equation for recessed UMEs[30] (*eq. 2.14*):

$$J_{L,a} = mnF[A^-] = \frac{4D_{A^-}}{4d + \pi r} nF[A^-] \qquad (2.14)$$

where m is the mass-transfer coefficient, and d is the insulator thickness. The normalized responses for each redox couple are depicted in 2.6c and 2.6d with an emphasis of the current near $E_{1/2}$. Full normalized voltammograms are shown in the respective insets. For FcMeOH, the inlaid- and recessed- disk UME responses overlay with each other at $E_{1/2}$, and generally follow the same shape at all relevant potentials. However, for the $Fe^{2/3+}$ redox couple, a small, but distinct negative shift is observed for the largest recession depth. Additionally, the current at higher and lower potentials for the 2.4 µm recession appears nominally consistent with that of the smaller recession depth and inlaid disk.

2.4. Discussion

The cumulative data speaks to three points. First, finite element modeling defines the applicability of the inlaid disk diffusion model for the determination of the heterogeneous charge

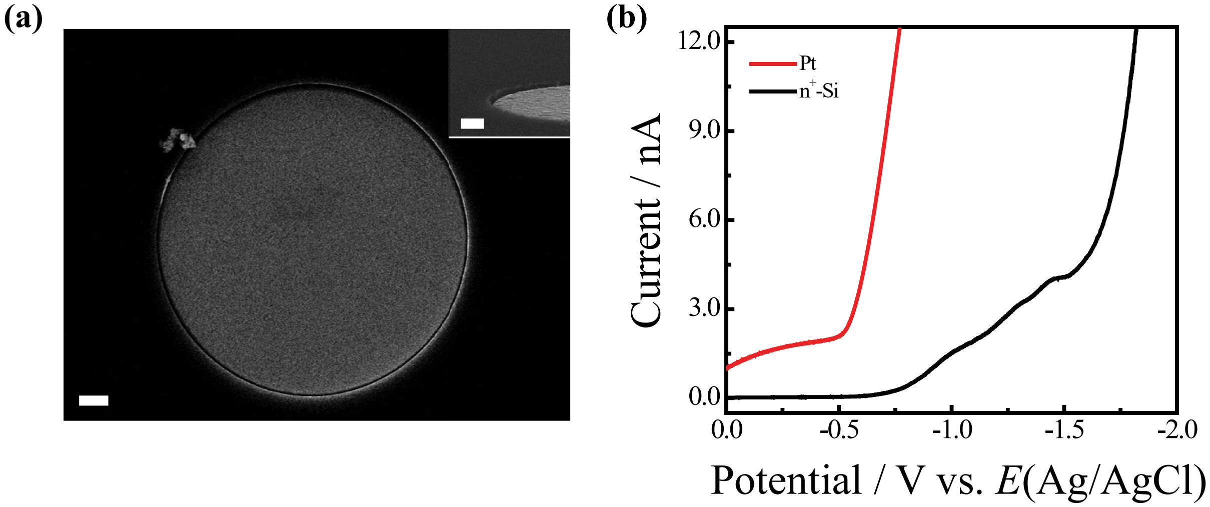

Figure 2.5. (a) Top-down scanning electron micrograph of a recessed Pt UME. The inset shows a 20° tilted image of the deposited metal relative to the insulator plane. The scale bare in both images are 1 μm. (b) Linear sweep voltammetric response of a 5 μm Pt UME with a recession depth of 2.4 μm and a 5 μm inlaid n^+-Si(111) UME in 500 mM KCl.

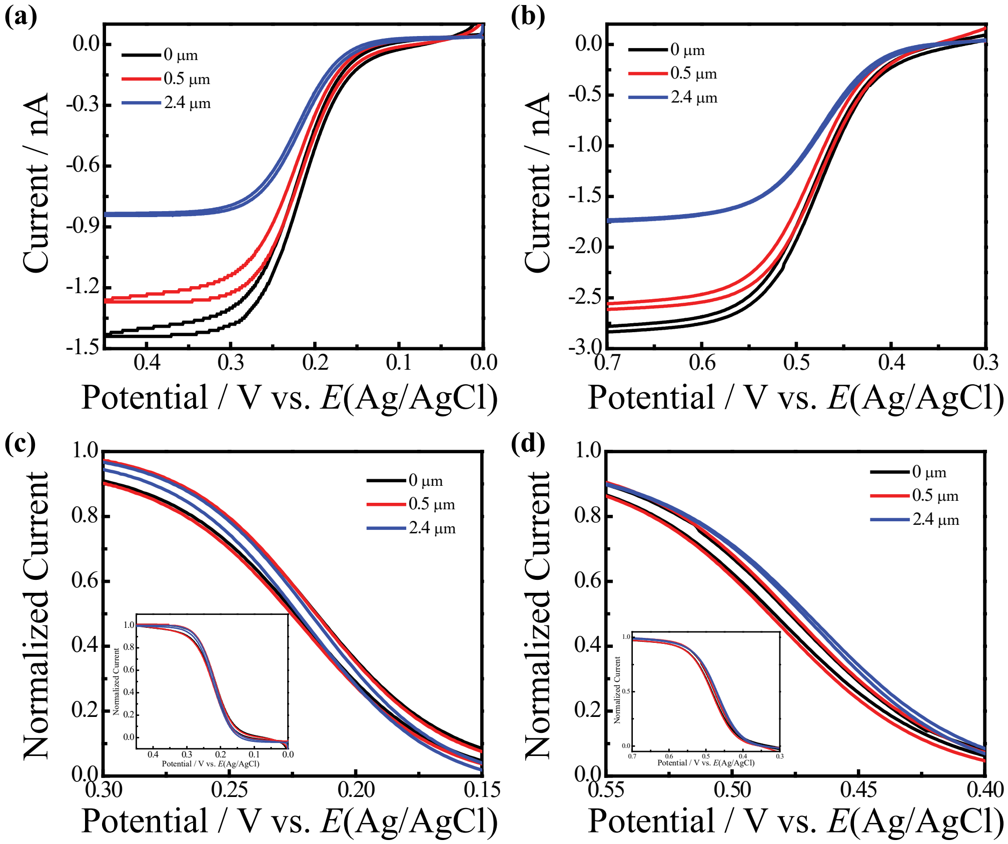

Figure 2.6. Experimental absolute current (a & b) and zoomed in normalized voltammograms (c & d) for the oxidation of (a & c) 1 mM FcMeOH and (b & d) 2 mM $Fe^{2/3+}$ with 5 μm Pt UMEs having recession depths of 0, 0.5, and 2.4 μm. The scan rate for all voltammetry was 5 mV s^{-1}. The insets in c & d show the full normalized voltammograms.

transfer rate constant and transfer coefficient at recessed disk electrodes. Second, the experimental voltammetric response of recessed Pt UMEs tracks with simulation predictions, but the exact interpretation is nuanced. Finally, several considerations are necessary to improve measurement quality with recessed disk UMEs. These points are discussed individually below.

Rate Constant Overestimation

The employed finite element simulations show a clear trend in overestimation of charge transfer measurement parameters using the inlaid disk model with recessed disk UMEs. The phenomenon of rate constant overestimation at UMEs has been previously attributed to a "lagoon effect" in which electroreactant becomes trapped in the recession due to a smaller cavity entrance than electrode diameter.[24, 26] However, the simulations here explicitly address cases where cavity walls are normal to the electrode surface. Within these geometries, the extent of linear diffusion relative to normally-operative radial diffusion will determine the attenuation of the mass transport -limited current.[23, 30] In turn, the faster the electrode reaches the diffusion limit, the larger the overestimation of the rate constant.

A notable underestimation of the rate constant was observed for the nearly irreversible $1x10^{-5}$ cm s^{-1} rate constant. Even with a lower charge transfer rate constant, the transport phenomena as a function of recession depth should be similar for faster reactions. A likely explanation for this result is poor applicability of the quasi-reversible Zoski-Bond-Oldham expression to irreversible cases. The limitation of using a quasi-reversible kinetic model for reversible kinetics have been discussed elsewhere,[31] but no such description has been made for kinetic determinations near the irreversible limit. Under these conditions, absorption effects may become prominent. While this may lead to uncertainty in using the quasi-reversible expression for an apparent irreversible process, the overall trend in k_{fit}/k_{et} at the largest of electrodes tracks with that of smaller electrodes.

The insulator thickness to electrode radius ratio, d/r, plays a primary role in the interpretation of electron transfer kinetics via an inlaid disk model. For measurement of a quasi-reversible redox system at a 50 µm radius recessed UME, an insulating layer thickness of less than 500 nm is needed to measure rate constants within ~10% of the true value. Staying within that same error range at a 5 µm radius recessed UME would require insulating layer thicknesses no larger than 350 nm. Finally, at a 500 nm UME, a recession depth less than 75 nm would be required to avoid overestimating the rate constant by greater than 10%. This trend shows a much slower decrease in the insulator thickness necessary to maintain a certain error tolerance for smaller electrode radii. The physical origin of this trend is unclear, but is unusual in the fact that the 50 µm recession curves deviate from the inlaid disk case much less than smaller electrodes. A possible explanation stems from the complex radius dependence on the recessed steady-state current (e.g. *eq. 2.14*). Accordingly, the current magnitude difference between an inlaid-disk electrode and a recessed-disk electrode with a defined d will change for different electrode radii. When normalized, these differences manifest themselves in the curves shifts shown in Figure 2.2.

For the range of transfer coefficients explored here, the fitted value can be found within 10% of the true value if the recession depth is no larger than the electrode radius. While the tolerance for α_{et} based on UME geometry is much larger than for k_{et}, measurements of these parameters are typically coupled. As such, the more stringent insulator thickness and electrode radius requirements for accurate rate constant measurements should be preferentially followed. An interesting observation for the α analysis is the leveling of the error at 8-10% uncertainty with increasing d/r, demonstrating a limited range of α_{et} for a single k_{et} value. That is, at large recession depths linear diffusion becomes more prominent and mass-transport limitations constrain the potential window for useful kinetic measurements. Under these conditions, α_{et} may no longer be truly independent of k_{et}.[32]

Experimental Measurements

The voltammetric analyses of charge transfer at inlaid and recessed Pt UMEs were generally consistent with the finite element simulations. However, several distinct differences should be noted. First, the simulations did not account for capacitive effects related to the metal/insulator/solution junction. The resulting hysteresis magnitude defines bounds in which shifts in potential can be accurately resolved. It is clear from Figure 2.6 that the magnitude of the shift between inlaid and 2.4 µm recessed electrode is within the hysteresis from the capacitive current. For smaller shifts associated with faster charge transfer properties this aspect would decrease the accuracy of values for $E_{1/2}$. However, this capacitive current can be intentionally modulated by altering fabrication and experiment parameters. For example, reducing the scan rate or growing thicker insulating layers will decrease the hysteresis and increase the resolution between the voltammetric responses. Additionally, further optimizing the insulator material properties, such as the dielectric constant, can also be used to decrease the capacitive current magnitude.

Second, the redox couple and electrolyte composition can produce unintended effects for charge transfer measurements. For the $Fe^{2/3+}$ redox couple, several previous reports describe inner-sphere mechanisms involving coupled absorption steps.[29, 33-34] This contrasts with the simulations employed in this work, where only purely outer-sphere processes are considered. The charge transfer rate for this oxidation is also known to be highly dependent on the supporting electrolyte composition.[33] Phenomena such as anion-bridging from the background salt or leaching from the reference electrode can enhance the observed charge transfer rate. While those effects were not explicitly avoided based on the employed experimental setup, the reaction was sufficiently slow to observe an apparent shift in the voltammetric response. Further, the same electrolyte composition was used for all collected voltammograms for a reliable comparison between recession depths.

Third, the roughness of the electrode surface could impact the observed charge transfer kinetics. While k_{et} for $Fe^{2/3+}$ has been measured well below 0.01 cm s^{-1},[29] the experimental data suggest a rate constant closer to 0.1-0.5 cm s^{-1}. The SEM image in Figure 2.5 shows a significant amount of roughness that could increase the number of available active sites or expose planes more active for charge transfer. Facet and active site engineering of platinum and other noble metals is pertinent for improving charge transfer facility in electrocatalytic applications. However, a detailed characterization of the Pt surface was not performed here. Additionally, flaking can occur when thermally deposited metal is applied too thick. In this sense, exploring other deposition methods for electrode materials may provide more robust platforms for long-term analyses.

Recessed Electrode Considerations

The above tolerances highlight some important limitations and concerns for kinetic measurements at the smallest of recessed and inlaid disk sizes. First, for the fabrication of recessed UMEs by common photolithographic methods, the smallest recession depth is defined by the thinnest insulator thickness in which no tunneling occurs. Recent examples of photoelectrochemical charge transfer across semiconductor/insulator/electrolyte junctions demonstrate the ability for charge carriers to tunnel through insulating layers as thick as 50 nm.[35] While this specific value is highly dependent on quality/structure of the insulator, it is a reasonable example for a minimum thickness to avoid pinhole formation. Although this work does not explicitly approach dimension that small, it can be estimated from the results that the minimum radius of electrodes in which the apparent rate constant is within 10% of the true value would be no less than ~50 nm for $d = 50$ nm. Such small features typically represent the lower limit of common fabrication methods, but any attempts to make smaller UMEs through laser pulling or microfabrication to obtain high mass transport rates should be met with caution to avoid significant error in the determined kinetic parameters.

A second insight this work affords with regards to kinetic measurements is the importance of characterizing the electrode geometry. With the recent push to measure extremely fast rate constants through the fabrication of <20 nm electrodes,[17] accurately characterizing electrodes has become challenging. This is especially true for electrochemically etched and laser-pulled nanoelectrodes, where the full tip radii can be highly variable for the same set of preparation conditions and result in total diameters not much larger than the electrode active area.[15] The work described herein implies that any recession is bound to have a notable effect on the accuracy of rate constant measurements, especially at small size scales. In that sense, using photolithographic methods used to fabricate the recessed Pt UMEs in this work are advantageous to produce well-defined insulator thicknesses and electrode areas that can be easily characterized.

2.5. Conclusions

This work describes charge transfer reactions at recessed-disk UMEs in the context of diffusion at inlaid-disk UMEs. Finite element simulations demonstrate a decrease in the mass transport-limited current with increasing recession depth. Accordingly, significant overestimation of the heterogeneous charge transfer rate constant and transfer coefficient occurs with larger UME recessions. Experimental measurements with recessed Pt UMEs highlight these trends. Still, further work is necessary to expand the utility of microfabricated recessed UME platforms. First, simulation and experimental analysis of non-degenerate electrodes substrates (i.e. semiconductors) with various recessed geometries would be useful to decouple redox couple diffusion and charge carrier transport in understanding the influence of electrode recession on photoelectrochemical performance. Next, examining charge transfer processes at small (<500 nm) recessed UMEs would lend insight into the role of insulator charge screening on the observable electrochemical parameters. Finally, optimization of electrode and insulator composition and exploration of alternative fabrication methods (i.e. atomic layer deposition) would provide more flexibility over platform robustness and insulator properties and thickness. Overall, such work would be useful to advancing electroanalysis methods.

2.6. References

1. Steinhoff, G.; Hermann, M.; Schaff, W. J.; Eastman, L. F.; Stutzmann, M.; Eickhoff, M. *Appl. Phys. Lett.* **2003,** *83*, 177.

2. Wang, J.; Golden, T. *Anal. Chim. Acta* **1989,** *217*, 343.

3. Fujishima, A.; Honda, K. *Nature* **1972,** *238*, 37.

4. Smith, W. A.; Sharp, I. D.; Strandwitz, N. C.; Bisquert, J. *Energ. Environ. Sci.* **2015,** *8*, 2851.

5. Hamann, T. W.; Gstrein, F.; Brunschwig, B. S.; Lewis, N. S. *Chem. Phys.* **2006,** *326*, 15.

6. Hamann, T. W.; Brunschwig, B. S.; Lewis, N. S. *J. Phys. Chem. B* **2006,** *110*, 25514.

7. Royea, W. J.; Hamann, T. W.; Brunschwig, B. S.; Lewis, N. S. *J. Phys. Chem. B* **2006,** *110*, 19433.

8. Mirkin, M. V.; Richards, T. C.; Bard, A. J. *J. Phys. Chem.* **1993,** *97*, 7672.

9. Ekanayake, C. B.; Wijesinghe, M. B.; Zoski, C. G. *Anal. Chem.* **2013,** *85*, 4022.

10. Kim, J.; Bard, A. J. *J. Am. Chem. Soc.* **2016,** *138*, 975.

11. Dayton, M. A.; Ewing, A. G.; Wightman, R. M. *Anal. Chem.* **1980,** *52* , 2392.

12. Sun, Y. Y. T.; Mirkin, M. V. *Anal. Chem.* **2016,** *88*, 11758.

13. Bond, A. M.; Oldham, K. B.; Zoski, C. G. *J. Electroanal. Chem.* **1988,** *245*, 71.

14. Oldham, K. B.; Myland, J. C.; Zoski, C. G.; Bond, A. M. *J. Electroanal. Chem.* **1989,** *270*, 79.

15. Shao, Y. H.; Mirkin, M. V.; Fish, G.; Kokotov, S.; Palanker, D.; Lewis, A. *Anal. Chem.* **1997,** *69*, 1627.

16. Woo, D. H.; Kang, H.; Park, S. M. *Anal. Chem.* **2003,** *75*, 6732.

17. Li, Y. X.; Bergman, D.; Zhang, B. *Anal. Chem.* **2009,** *81*, 5496.

18. Kounaves, S. P.; Deng, W.; Hallock, P. R.; Kovacs, G. T. A.; Storment, C. W. *Anal. Chem.* **1994,** *66*, 418.

19. Feeney, R.; Kounaves, S. P. *Anal. Chem.,* **2000,** *72*, 2222.

20. Lindner, E.; Cosofret, V. V.; Buck, R. P.; Johnson, T. A.; Ash, R. B.; Neuman, M. R.; Kao, W. Y. J.; Anderson, J. M. *Electroanalysis* **1995,** *7*, 864.

21. Guo, J. D.; Lindner, E. *Anal. Chem.* **2009,** *81*, 130.

22. Guo, J. D.; Lindner, E. *J. Electroanal. Chem.* **2009,** *629*, 180.

23. Bartlett, P. N.; Taylor, S. L. *J. Electroanal. Chem.* **1998,** *453*, 49.

24. Oldham, K. B. *Anal. Chem.* **1992,** *64*, 646.

25. Chen, J. Y.; Aoki, K. *Electrochem. Commun.* **2002,** *4*, 24.

26. Baranski, A. S. *J. Electroanal. Chem.* **1991,** *307*, 287.

27. Acharya, S.; Lancaster, M.; Maldonado, S. *Anal. Chem.* **2018,** *90*, 12261.

28. Sun, P.; Mirkin, M. V. *Anal. Chem.* **2006,** *78*, 6526.

29. Samec, Z.; Weber, J. *J. Electroanal. Chem.* **1977,** *77*, 163.

30. Bond, A. M.; Luscombe, D.; Oldham, K. B.; Zoski, C. G. *J. Electroanal. Chem.* **1988,** *249*, 1.

31. Simonov, A. N.; Morris, G. P.; Mashkina, E. A.; Bethwaite, B.; Gillow, K.; Baker, R. E.; Gavaghan, D. J.; Bond, A. M. *Anal. Chem.* **2014,** *86*, 8408.

32. Weaver, M. J.; Anson, F. C. *J. Phys. Chem.* **1976,** *80*, 1861-1866.

33. Weber, J.; Samec, Z.; Marecek, V. *J. Electroanal. Chem.* **1978,** *89*, 271.

34. Bochmann, H. G.; Vielstich, W. *Electrochim Acta* **1988,** *33*, 805.

35. Kim, H. J.; Kearney, K. L.; Le, L. H.; Haber, Z. J.; Rockett, A. A.; Rose, M. J. *J. Phys. Chem. C* **2016,** *120*, 25697.

CHAPTER 3

Semiconductor Ultramicroelectrodes (SUMEs): Platforms for Studying Charge-Transfer Processes at Semiconductor/Liquid Interfaces

Reprinted with permission from Acharya, S.; Lancaster, M.; Maldonado, S. Semiconductor Ultramicroelectrodes (SUMEs): Platforms for Studying Charge-Transfer Processes at Semiconductor/Liquid Interfaces *Anal. Chem.* **2018**, *90*, 12261-12269. Copyright 2018 American Chemical Society.

3.1. Introduction

The topic of semiconductor electrochemistry has been critical to advancing fundamental electrochemical concepts, including the nature of charged solid/liquid interfaces, heterogeneous reaction kinetics, photochemical processes, and corrosion/passivation.[1] Semiconductor electrochemistry also is at the heart of many long-standing applied technologies such as semiconductor wet etching,[2-4] ion-sensitive field effect transistor sensors,[5-6] and photoelectrochemical energy conversion strategies.[7-9] Paradoxically, though, the ability to interpret readily, quantitatively, and unambiguously even the most basic voltammetric responses for charge transfer between a semiconductor electrode and a dissolved redox species is still a challenge.[10-17]

Unlike in a metal, the surface concentration of charge carriers in a semiconductor electrode is a complex function of the applied potential.[18-19] This aspect substantially convolutes the influences of charge-transfer kinetics and mass transport on voltammetry with semiconductor electrodes, rendering the established methods for analyzing voltammetry data useless. Although the rotating disk motif can impart well-defined mass transport conditions to macroscopic semiconductor electrodes,[15, 20-22] such platforms are sufficiently cumbersome that repetitive studies where bulk (e.g. doping, mobility, charge-carrier lifetimes) and surface (e.g. roughness, chemical functionality, trap state density) properties are systematically varied are precluded. Consequently, new electrochemical strategies are needed to advance fundamental and applied understanding of charge transfer at semiconductor/electrolyte junctions.

A surprisingly under-explored concept in semiconductor electrochemistry is to employ semiconductor ultramicroelectrodes (SUMEs). The mass transport to small electrodes is well understood,[23-26] potentially making it possible to model and fit the steady-state voltammetric responses of SUMEs comprehensively. Accordingly, the purpose of this report is to demonstrate and validate a specific type of SUME platform amenable for detailed study and widespread use for any semiconductor material. Specifically, we demonstrate that a small, circular pinhole photolithographically patterned in a thin dielectric coating on an otherwise flat, clean single-crystalline semiconductor substrate can act as a recessed disk ultramicroelectrode (Figure 3.1). This design is advantageous because (*1*) it can be used with any semiconductor material available in planar form, (*2*) it obviates the need to mechanically process (polish) the semiconductor surface, and (*3*) it can be mass-produced for repetitive measurements. Further, this design is amenable to precise and facile control of electrode dimensions, a factor that can be exploited intentionally if care is taken during fabrication.

Herein, this report shows the quantitative and analytical utility of pinhole SUME platforms for studying charge-transfer processes at semiconductor/electrolyte contacts. Several aspects of SUMEs are discussed. First, an explicit description of how the doping concentration, charge-transfer kinetics, mass transport, and the extent of depletion within the semiconductor impact voltammetric responses of n-type SUMEs is described. Additionally, this work presents the experimentally measured responses of SUMEs prepared with single-crystalline n-Si, highlighting their sensitivity towards the dynamic nature of the Si/water interface. Finally, the responses of n-Si SUMEs are analyzed to elucidate measurements of interfacial charge-transfer rate constants of Si in aqueous electrolytes.

3.2. Background

At sufficiently slow scan rates, the voltammetric response of an ultramicroelectrode far from any physical obstruction attains a steady-state *J-E* response that follows spherical rather than linear diffusional transport. Because the current tends to a limiting value when diffusion outpaces kinetics, the steady-state shape necessarily describes the competition between precisely defined mass transport and charge-transfer kinetics. One approach to interpret the voltammetric responses of disk ultramicroelectrodes is through finite-element[27] or numerical modeling[28] of the transport. Although descriptive and quantitative, this approach does not readily afford simple

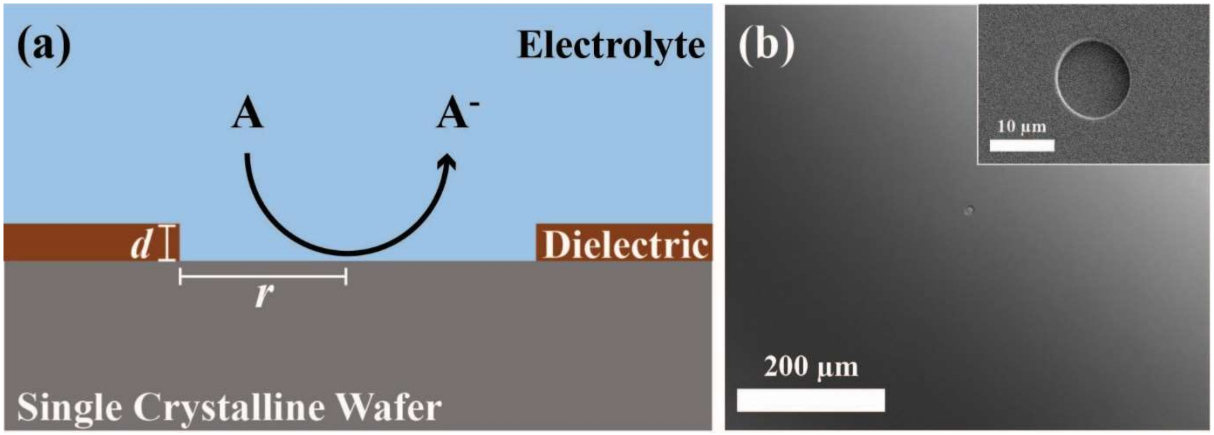

Figure 3.1. (a) Cross-sectional view of an idealized SUME platform based on a defined pinhole in a thin dielectric coating on a planar semiconductor electrode. (b) Large-area optical image of an n-Si SUME with $r = 5$ µm. Inset: Scanning electron micrograph at higher magnification of the same SUME.

prediction of the features of a SUME electrode. A more convenient alternative method is through the analytical expressions developed by Zoski and co-workers for disk ultramicroelectrodes.[29-30] In their analysis, the normalized current (i.e. dividing the measured current by the mass transport-limited cathodic current, $J_{L,c}$) follows *eq 3.1*,

$$\frac{J}{J_{L,c}} = \frac{1}{\theta\left[1+\frac{\pi}{\theta\kappa}\left(\frac{2\kappa\theta+3\pi}{4\kappa\theta+3\pi^2}\right)\right]} \qquad (3.1)$$

where θ & κ are dimensionless numbers that relate to the diffusion of the redox species and the governing rate constants at the electrode/electrolyte interface as shown in *eqs 3.2* and *3.3*.

$$\theta = 1+\frac{D_A}{D_{A^-}}\frac{k_b}{k_f} \qquad (3.2)$$

$$\kappa = \frac{\pi r k_f}{4D_A} \qquad (3.3)$$

In *eqs 3.2* and *3.3,* D_A and D_{A-} are the diffusion coefficients of the oxidized and reduced form of the redox couple, k_f is the rate constant for the reduction of A to A^-, and k_b is the rate constant for the oxidation of A^- to A. Typically, the potential dependence is ascribed by applying the Butler-Volmer formalism to the values of k_f and k_b.[25] However, this approach assumes that the densities of charge carriers are constant and that the rate constants depend on potential. In a nondegenerately doped semiconductor electrode operating under depletion conditions, the opposite is true and a different approach is needed to evaluate *eqs 3.1-3.3*.[1, 31]

For a nondegenerately doped n-type semiconductor electrode in the dark, the following expressions for k_f and k_b are appropriate in an unpoised electrolyte containing just one type of dissolved, reducible species, A. (Analogous expressions can be written for oxidation of A^- in the dark at a p-type semiconductor).

$$k_f = k_{et} n_s\left(E\right) \qquad (3.4)$$

$$k_b = k_{et}^{-1} = k_{et} n_{s,E^{0'}} = k_{et} N_{cb} e^{\frac{q}{k_B T}\left(E_{cb}-E^{0'}\right)} \qquad (3.5)$$

$$n_s(E) = n_{s,E^{0'}} e^{\frac{-q}{\gamma k_B T}\left(E-E^{0'}\right)} \qquad (3.6)$$

$$n_{s,E^{0'}} = N_{cb} e^{\frac{q}{k_B T}\left(E_{cb}-E^{0'}\right)} \qquad (3.7)$$

In these equations, $n_s(E)$ is the surface concentration of electrons (majority carriers) at potential E, $n_{s,E^{0'}}$ is the surface concentration of electrons at the formal potential ($E^{\circ`}$) of the redox species, N_{cb} is the effective density of states at the conduction band edge, E_{cb} is the conduction band edge potential, k_{et} (cm^4 s^{-1}) is the rate constant for electron transfer from the conduction band edge of the semiconductor, and γ is the ideality factor of the semiconductor/electrolyte interface. All other terms have their usual meanings. Two implicit assumptions in *eqs 3.4-3.7* is that all the applied potential drops within the space charge region of the semiconductor and that charge-transfer occurs exclusively through one band (i.e. the conduction band for n-type materials). Additionally, *eq 3.6* as written has no lower bounds on the value of $n_{s,E^{0'}}$, but in practice other physical processes (e.g. thermal generation of carriers at defects) could impose a practical limit on the smallest possible majority carrier concentration at the surface.[32]

With *eqs 3.1-3.7,* the steady-state voltammetric response of an n-type SUME can be readily understood as a function of E_{cb}, k_{et}, $E^{\circ`}$, and $\gamma$ in the same manner that a single voltammetric response of a metal ultramicroelectrode is routinely modeled for the values of the charge transfer coefficient ($\alpha$), the standard rate constant ($k_{et}$), and $E^{\circ`}$.[25, 29-30] Importantly, although the term γ superficially has an analogous effect in describing current-potential responses as α does in Butler-Volmer kinetic theory, its meaning here is physically different. That is, γ is a quantitative measure of the quality of the semiconductor/electrolyte interface[33-34] and has a value of precisely '1' when all of the applied potential is used to drive interfacial charge-transfer by thermionic emission of majority carriers at the band edge. Several distinct factors (e.g. potential drop at the double layer,[35] mass transport resistance,[36] the presence of charge traps at the surface[4]) can elicit $\gamma > 1$.

Figure 3.2 displays the predicted trends in voltammetric responses using the Bond, Zoski, and Oldham approach[25] described above for n-type Si SUMEs with $N_d = 1 \times 10^{15}$ cm^{-3}. In these figures, the conduction band edge potential is denoted by the vertical dashed lines. Figure 3.2a illustrates the response for an n-type Si SUME as a function of $E^{\circ`}$. The most obvious and striking feature is that in strong contrast to metal ultramicroelectrodes, the normalized voltammetric responses are wholly *independent* of $E^{\circ`}$ when $E^{\circ`}$ is far from E_{cb} if all other model parameters are the same. The rationale is that in semiconductor electrodes, the surface concentration of majority carriers (electrons) depends on the potential with respect to E_{cb} rather

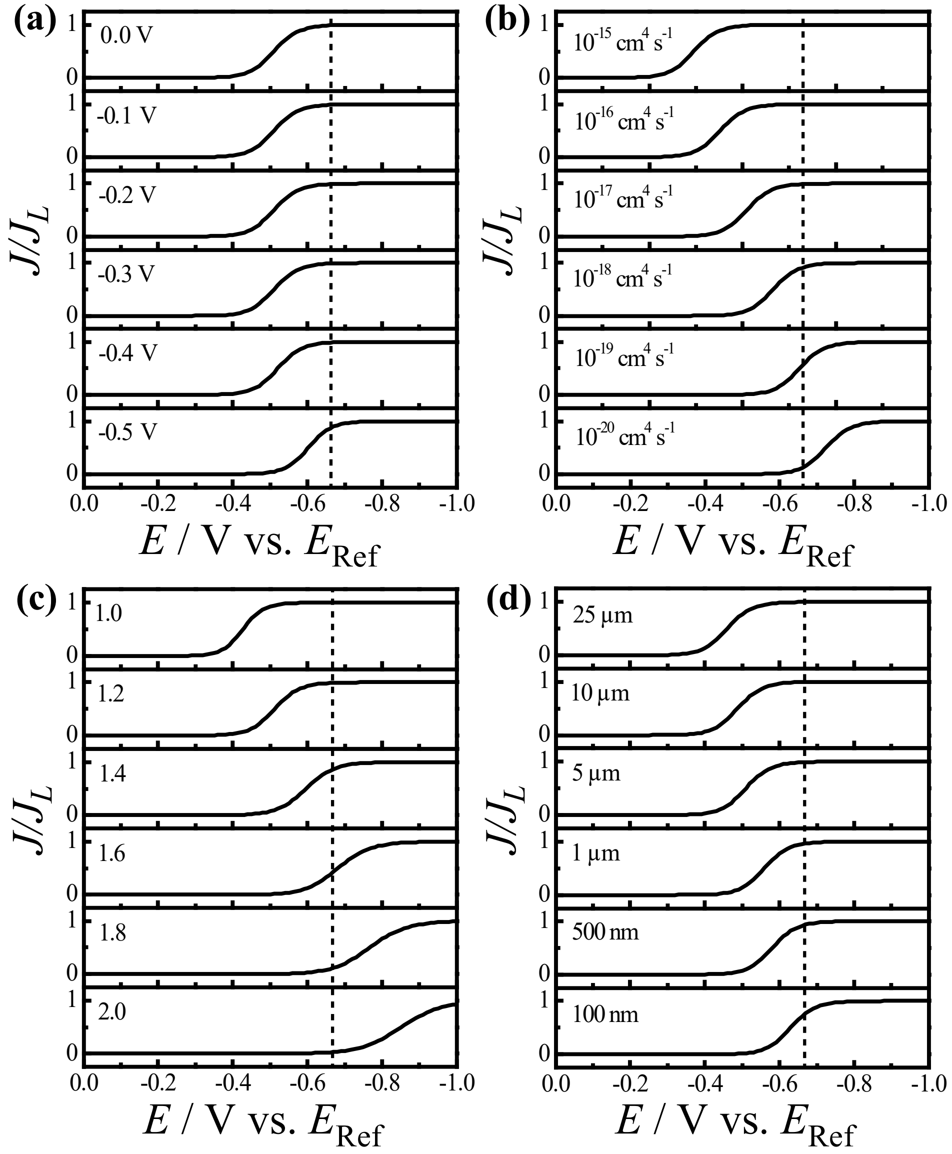

Figure 3.2. Modeled steady-state voltammetric responses of nondegenerately doped n-type SUMEs ($N_d = 1 \times 10^{15}$ cm^{-3}) based on equations S*1*-S*7* as a function of variation in the electron transfer rate constant (k_{et}), the standard potential of the redox couple ($E^{\circ'}$), the ideality factor (γ), and the disk radius (r). (a) Variation in $E^{\circ'}$ with $E_{cb} = -0.68$ V, $k_{et} = 10^{-17}$ cm^4 s^{-1}, $\gamma = 1.2$, and $r = 5$ μm. (b) Variation in k_{et} with $E_{cb} = -0.68$ V, $\gamma = 1.2$, $E^{\circ'} = 0$ V, and $r = 5$ μm. (c) Variation in γ with $E_{cb} = -0.68$ V, $k_{et} = 10^{-17}$ cm^4 s^{-1}, $E^{\circ'} = 0$ V, and $r = 5$ μm. (d) Variation in r with $E_{cb} = -0.68$ V, $k_{et} = 10^{-17}$ cm^4 s^{-1}, $\gamma = 1.2$, and $E^{\circ'} = 0$ V.

than $E^{\circ`}$.[1, 37] As a result, the position of a single voltammetric response for a SUME gives little information on $E^{\circ`}$ but can be understood more readily in relation to E_{cb}. This feature has been a confounding aspect of conventional voltammetry with semiconductor macroelectrodes,[10-14, 16-17] but is clear in the responses of SUMEs. In fact, for a nondegenerately doped SUME, voltammetric responses that are near $E^{\circ`}$ imply that $E^{\circ`}$ is near E_{cb}.

Figure 3.2b shows the predicted response at an n-type SUME for various redox couples with the same $E^{\circ`}$ values but different k_{et} values. Here, the position of the normalized voltammetric response with respect to the band edge is *strongly* sensitive to the value of k_{et}. Hence, the mere position of the current-potential response of a SUME is an indicator of the respective charge-transfer rate constant. Figure 3.2c presents the predicted sensitivity of n-type SUMEs towards variations in γ. Two aspects are readily apparent when γ is larger than 1. First, the voltammetric response is broadened significantly and the current onset is less steep, e.g. the potential at $J/J_L = 0.5$ occurs further from the potential of current onset when $\gamma > 1$. Accordingly, the shape of the voltammetric response is an immediate indicator of the quality of semiconductor/electrolyte interface. Second, the broadening incurred by $\gamma > 1$ shifts the entire, normalized voltammetric response towards more negative potentials. This aspect means that estimation of k_{et} from the position of the voltammetric response cannot be performed without also assessing the value of γ. Figure 3.2d highlights how the normalized steady-state current-potential curves shift as a function of r. Smaller values of r result in higher attainable absolute current densities and also shift the normalized current-potential responses towards more negative potentials. Again, estimation of k_{et} from the position of the voltammetric response also cannot be performed without direct knowledge of r beforehand.

3.3. Experimental

Chemicals and Materials

Hexaammineruthenium (III) chloride ($Ru(NH_3)_6Cl_3$, 98%, Fisher), methyl viologen dichloride hydrate (98%, Sigma-Aldrich), cobalt (III) sepulchrate trichloride (95%, Sigma-Aldrich), $K_4Fe(CN)_6 \cdot 3H_2O$ (Alfa Aesar, 98%), KCl (99.65%, Fisher), KNO_3 (99%, Acros Organics), acetone (ACS grade, Fisher), 2-propanol (ACS grade, Fisher), buffered hydrofluoric acid (BHF, Transene), Nano-strip (Cyantek® KMG 539400 Nano-Strip 2X®), Microposit S1813 photoresist (Shipley) and Megaposit SPR 220 3.0 photoresist (Microchem) were used as received. Degenerately doped n-type Si(111) 4 in wafers (0.525 mm, ρ = 0.003 Ω·cm, MTI Corp.) and n-type Si(100) 4 in wafers (0.5 mm, ρ = 4.5 Ω·cm, SunEdison) were used for fabrication of SUMEs. All electrolyte solutions were made with >18 MΩ·cm resistivity water (Barnstead Nanopure).

SUME Fabrication

All substrate wafers were subject to the RCA cleaning process with a final dip in BHF for 30 seconds prior to initial use. The wafers were immediately introduced into a Spin Rinse Drier (Verteq SRD, Class One Equipment) and transferred into a low pressure chemical vapor deposition (LPCVD) furnace (Tempress Systems) for 150 nm silicon oxynitride (SiO_xN_y) deposition at a rate of 2.2 nm min^{-1} and T = 850 °C. Alternatively, for thicker insulator deposition, 600 nm silicon oxide (SiO_2) was deposited on the wafers by plasma-enhanced chemical vapor deposition (PECVD) (Ultradep 2000, GSI Lumonics) at a deposition rate of 18.6 nm min^{-1} and T = 350 °C, followed by rapid thermal annealing (Jetfirst RTP 150, Jipelec) in N_2 (g) at T = 800 °C for 5 min. Back ohmic contacts were formed by depositing Ti(10 nm)/Au(120 nm) using an e-beam evaporator (Evovac, Angstrom Engineering). Immediately prior to this step, back side SiO_xN_y from the LPCVD deposition was wet etched in BHF for 15 minutes (etch rate = 10 nm/min) while the SiO_xN_y on the top surface was protected by spincoating 1.5 µm of S1813 with a softbake at T = 110 °C for 4 min. Following back contact deposition, the top protective S1813 film was removed by immersing the wafer in Nano-Strip. The substrates were vapor primed with hexamethyldisilazane (HMDS) in a YES-310TA (E) oven and SPR 220 3.0 was then immediately spincoated to an average thickness of 2.18 µm. The films were soft baked for 90 seconds at T = 115 °C. Projection photolithography (GCA Autostep 200, RZ Enterprises, Inc.) was used to expose (365 nm) the coated substrate through custom photolithography masks containing dies with r =1.5, 5, and 10 µm features at the center of individual dies. The pattern was then transferred to the underlying SiO_xN_y or SiO_2 film by reactive ion etching (RIE) (APS Dielectric Etch Tool, STS) with C_4F_8 (g). The etch rate was adjusted to 177.6 nm min^{-1} for SiO_xN_y and to 353.4 nm min^{-1} for SiO_2. To prevent any possible plasma damage to the Si surface in the SUME region, the RIE etch was stopped with 10-20 nm of SiO_xN_y or SiO_2 left in the features, which was then removed by wet etching in BHF. The wafers were diced into individual dies and the SPR 220 3.0 film was dissolved off in acetone and rinsed in 2-propanol prior to further use.

Electrochemical Measurements

All voltammetric experiments were performed using CHI420A and CHI760C (CH Instruments) potentiostats in a custom-built, dark Faraday cage. The fabricated SUMEs were etched in BHF immediately before being placed in an open-air Teflon cell and sealed with a Viton o-ring (ID = 2.9 mm, McMaster-Carr). A three-electrode configuration with a Ag/AgCl (Sat'd KCl) reference and a flame-cleaned Pt wire counter electrode was used throughout.

Impedance (Mott-Schottky) measurements were taken using a Solartron 1286 electrochemical interface coupled to a model 1250 impedance analyzer (Ametek). A 10 mV sinusoidal AC potential with frequencies from 10 Hz to 52 kHz was applied over DC potentials ranging from -0.15 V to 0.7 V. Immediately before each measurement, bare n-Si electrodes (0.19 cm^2) were etched in BHF for 1 min. The impedance data were fit with the Mott-Schottky equation to determine the flat-band potential of the semiconductor/electrolyte contact, E_{fb}

$$C_{sc}{}^{-2} = \frac{2}{q\varepsilon\varepsilon_o N_d A^2}\left(E_{applied} - E_{fb} - \frac{k_B T}{q}\right) \tag{3.8}$$

where q is the unit coulombic charge, ε is the static dielectric constant of the bulk semiconductor, ε_o is the permittivity of free space, N_d is the bulk dopant concentration, A is the area of electrode exposed to solution, $E_{applied}$ is the applied DC bias, k_B is Boltzmann's constant, and T is temperature. From E_{fb}, the conduction band energy was calculated using the effective density of states in the conduction band, N_{cb}

$$E_{cb} = E_{fb} + k_B T \ln\left(\frac{N_d}{N_{cb}}\right) \tag{3.9}$$

where $N_{cb} = 2.8 \times 10^{19}$ cm^{-3} for Si. The reported conduction band energies were averages from three different electrodes with the error corresponding to the standard deviations of those measurements. To influence the band energetics at the semiconductor/electrolyte interface, both macroscopic and microscopic n-Si electrodes were immersed in 5 mM $K_4Fe(CN)_6$ under ambient light for 5 min, followed by corresponding impedance and voltammetry measurements, respectively. Optical images of fabricated n-Si UMEs were taken on an Infinity 3 camera (Lumenara) mounted on an Olympus BX60 optical microscope. Scanning electron micrographs were acquired with a LEO 1455VP SEM (Zeiss) equipped with an Everhart-Thornley detector (ETD) and tungsten filament source (Ted Pella) operated at 10 kV.

Equivalent Rotation Rates for Attaining the Same Mass Transfer Coefficients of the SUMEs in this work

The mass transfer coefficient of a recessed disk ultramicroelectrode can be compared to the corresponding value for a rotating disk electrode at a given rotation rate. Table 3.1 lists the necessary rotation rates needed to reach the same flux conditions as the SUMEs presented in the text (*vide infra*).

Reorganization Energy Calculation

The total reorganization energy for a redox couple at a semiconductor electrode, λ_{sc}, can be considered as the sum of inner-sphere, $\lambda_{sc,i}$, and outer-sphere, $\lambda_{sc,o}$ components[38]

$$\lambda_{sc} = \lambda_{sc,i} + \lambda_{sc,o} \tag{3.10}$$

which represent changes in bond lengths/angles and changes in solvation around the outer-coordination sphere, respectively. In the case of heterogenous charge-transfer reactions, the inner sphere contribution at a Si electrode can be approximated by half the inner-sphere reorganization energy for the corresponding homogeneous self-exchange reaction, $\lambda_{se,i}$.[38] The value $\lambda_{se,i}$, in turn, can be calculated by subtracting the self-exchange outer-sphere reorganization energy ($\lambda_{se,o}$) from the self-exchange total reorganization energy (λ_{se}), giving

$$\lambda_{sc} = \frac{\lambda_{se} - \lambda_{se,o}}{2} + \lambda_{sc,o} \tag{3.11}$$

where λ_{se} for $Ru(NH_3)_6^{3+}$, MV^{2+}, and $Co(sep)_3^{3+}$ are measurable quantities of 1.6,[39] 0.6,[40] and 2.6 eV,[40] respectively. $\lambda_{se,o}$ can be separately estimated by *eq 3.12*[38]

$$\lambda_{se,o} = \frac{q}{4\pi\varepsilon_0}\left(\frac{1}{a_i} - \frac{1}{R_h}\right)\left(\frac{1}{n_{H_2O}^2} - \frac{1}{\epsilon_{H_2O}}\right) \tag{3.12}$$

where ε_0 is the permittivity of free space, a_i is the ionic radius of the redox probe (3.4,[41] 3.6,[40] and 4.5 Å[40] for $Ru(NH_3)_6^{3+}$, MV^{2+}, and $Co(sep)_3^{3+}$, respectively), R_h is the distance between the reactants (taken to be $2a_i$), n_{H2O} is the refractive index of water (1.34[42]), and ϵ_{H2O} is the static dielectric constant of water (78.46).[42] Similarly, $\lambda_{sc,o}$ can be calculated by *eq 3.13,*[43]

$$\lambda_{sc,o} = \frac{q}{8\pi\varepsilon_0}\left[\frac{1}{a_i}\left(\frac{1}{n_{H_2O}^2} - \frac{1}{\epsilon_{H_2O}}\right) - \frac{1}{2a_i}\left(\left(\frac{n_{Si}^2 - n_{H_2O}^2}{n_{Si}^2 + n_{H_2O}^2}\right)\frac{1}{n_{H_2O}^2} - \left(\frac{\epsilon_{Si} - \epsilon_{H_2O}}{\epsilon_{Si} + \epsilon_{H_2O}}\right)\frac{1}{\epsilon_{H_2O}}\right)\right] \tag{3.13}$$

where n_{Si} and ϵ_{Si} are the refractive index (3.8)[44] and static dielectric constant (11.7)[42] of Si, respectively.

Table 3.1. Mass transport-limited current density and equivalent RDE rotation rate for n-Si SUMEs[a]

r / µm	$J_{L,c}$ / mA cm^{-2}	Equiv. RDE Rate / rpm
10	1.64	2317
5	3.83	12663
1.5	12.5	135450

[a] Assuming a kinematic viscosity of 8.8 x 10^{-3} cm^2 s^{-1}

Calculation of Potential Drop Across the Semiconductor/Liquid Interface.

In depletion, a common assumption is all of the applied potential, $E_{applied}$, is dropped entirely across the space charge region of the semiconductor. In practice, the applied potential is actually distributed across both the semiconductor space charge region and the solid/liquid interface. For a semiconductor electrode, these two potential drops arise from the respective capacitances being linked in series. The corresponding fractions of the applied potential that are distributed across each can be determined numerically.[31, 35] The absolute value of the space charge capacitance for lightly doped Si in depletion and weak accumulation conditions can be determined from the following,[35]

$$C_{sc} = \left(\frac{q^2 N_d \varepsilon \varepsilon_0}{2 k_B T} \right)^{1/2} \left(e^{\frac{q(\Delta E_{sc})}{k_B T}} - 1 \right) \left(e^{\frac{q(\Delta E_{sc})}{k_B T}} - \frac{q(\Delta E_{sc})}{k_B T} - 1 \right)^{-1/2} \qquad (3.14)$$

where ΔE_{sc} is the built in potential within the space charge region and all the other terms are as defined previously. This expression simplifies to *eq 3.8* for just depletion conditions. Using a double layer capacitance of 5 μF cm^{-2}, the fraction of the applied potential dropped across the space charge region in Si for the systems reported here was determined and is shown Figure 3.3. These values were then used in the fitting analyses for the second column of fitted k_{et} and γ values in Table 3.2.

3.4. Results

n-Si SUME Response Characteristics

Figure 3.4 highlights the measured doping- and size-dependent voltammetric responses of n-Si SUMEs with r = 1.5, 5, and 10 μm in an aqueous 0.1 M KCl electrolyte with dissolved $Ru(NH_3)_6^{3+}$ ($E^{\circ`}$ = -0.145 V vs. E(Ag/AgCl)). These curve shapes are dependent on the heterogeneous charge transfer rate constant, k_{et}, the conduction band energy, E_{cb}, and the surface quality, γ, which describes the dominant mode of recombination at the interface. Figure 3.4a shows a comparison of sigmoidal voltammetric responses for two separate Si SUMEs with r = 5 μm but different doping levels (i.e. non-degenerate vs degenerate doping). Tunneling of charge-carriers from the bulk through the narrow width of the depletion layer in the semiconductor is extensive in degenerately doped semiconductors, resulting in response characteristics similar to metallic electrodes.[45] The positions of the steady-state responses for the

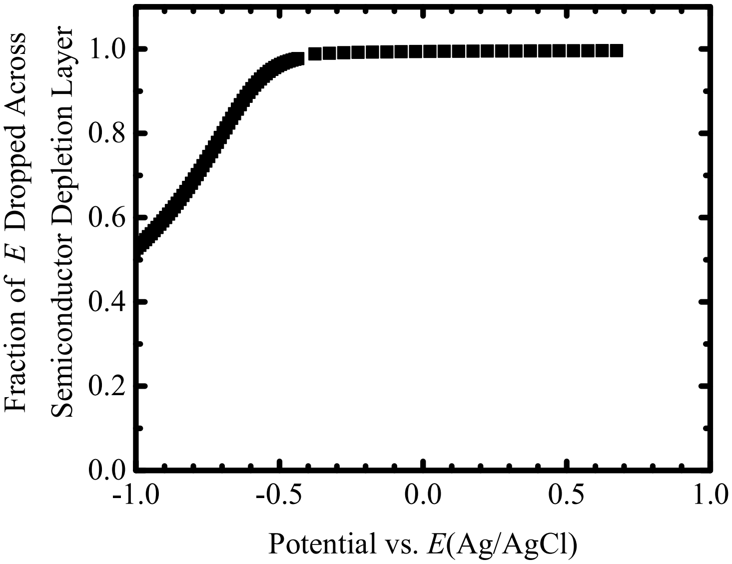

Figure 3.3. Fraction of potential dropped across space charge region in n-Si with $N_d = 1.6 \times 10^{15}$ cm^{-3} immersed in water with an ionic strength of 0.1 M as a function of the applied potential.

Table 3.2. Relevant Parameters for and Results of Data Fitting of Steady-State Voltammetric Responses for the Reduction of Outer-Sphere Redox Couples at n-Si in 0.1 M KCl(aq)[a]

Redox Couple	$E°`$/ V vs. E(Ag/AgCl)[b]	λ_{sc} / eV[c]	k_{et}[d]/ cm^4 s^{-1}	γ[d]	k_{et}[e] / cm^4 s^{-1}	γ[e]
$Ru(NH_3)_6^{3+}$	-0.145	0.91	(5.9 ± 1.2) x 10^{-16}	1.5 ± 0.1	(2.9 ± 0.8) x 10^{-16}	1.5 ± 0.8
MV^{2+}	-0.625	0.64	(1.1 ± 0.3) x 10^{-22}	1.2 ± 0.1	(1.8 ± 0.3) x 10^{-22}	1.3 ± 0.1
$Co(sep)_3^{3+}$	-0.450	1.38	(3.5 ± 4.6) x 10^{-23}	1.8 ± 0.1	*NA*	*NA*

[a] Data obtained with n-Si SUMEs with r = 5 μm

[b] Values obtained from Reference [70]

[c] Calculation of reorganization energies described earlier in text

[d] Results from fitting raw data

[e] Results from fitting data corrected for potential drop across the semiconductor/liquid interface as detailed above

non-degenerately and degenerately doped SUMEs were significantly different. The voltammetric response of the degenerately doped n-Si SUME was centered at $E_{applied}$ = -0.25 V, i.e. close to the formal potential of $Ru(NH_3)_6^{3+}$ as expected for a metallic ultramicroelectrode.[46] In contrast, the response of the non-degenerately n-Si SUME was shifted significantly to more negative potentials. Based on the trends shown in Figure 3.2 and a value of E_{cb} = -0.677 V (*vide infra*), these data implied $k_{et} > 10^{-17}$ cm^4 s^{-1}.

A common feature in both degenerately doped and non-degenerately doped Si SUME responses was appreciable capacitive currents, even at a scan rate of only 0.005 V s^{-1}. This residual capacitive current arose from the large total junction area (~ 0.07 cm^2) of the thin dielectric layer with the electrolyte. Similar stray capacitances were previously observed in metal-insulator-electrolyte nanoband electrodes when the dielectric does not fully screen the charge between the underlying electrode and electrolyte.[47-48]

Figure 3.4b compares the responses of n-Si SUMEs with different values of r in the same electrolyte, where the steady-state current magnitudes clearly tracked with r. Similarly, the normalized current-potential responses (Figure 3.4b inset) shifted as predicted from Figure 3.2. The mass transport-limited current density tracked linearly with $(4d+\pi r)^{-1}$ (Figure 3.4c), in accord with predictions for recessed disk ultramicroelectrodes described by *eq 3.15*,[29]

$$J_{L,c} = mq\left[A\right] = \frac{4D}{4d+\pi r}q\left[A\right] \qquad (3.15)$$

where m is the mass transfer coefficient, $[A]$ is the concentration of the species being reduced in solution, D is the diffusion coefficient of the oxidized species, r is the electrode radius, and d is the dielectric thickness. The attainable mass transport rate at each SUME can be compared with the corresponding rotation rate needed for a rotating disk electrode to reach the same value (assuming a kinematic viscosity of 8.8 x 10^{-3} cm^2 s^{-1}, Table 3.1).[49] Notably, at r = 1.5 µm, the equivalent rotation rate (~140,000 rpm) is significantly larger than what is typically achievable with mechanical rotators, underscoring a potent advantage of SUMEs for enabling measurements at high current densities. However, for SUMEs with smaller r values, the dielectric thickness was similarly adjusted to maintain ratios of $d/r < 1$. That is, for SUMEs with r = 10 µm, a dielectric thickness of 0.6 µm was used while for SUMEs with r = 1.5 µm a thinner dielectric

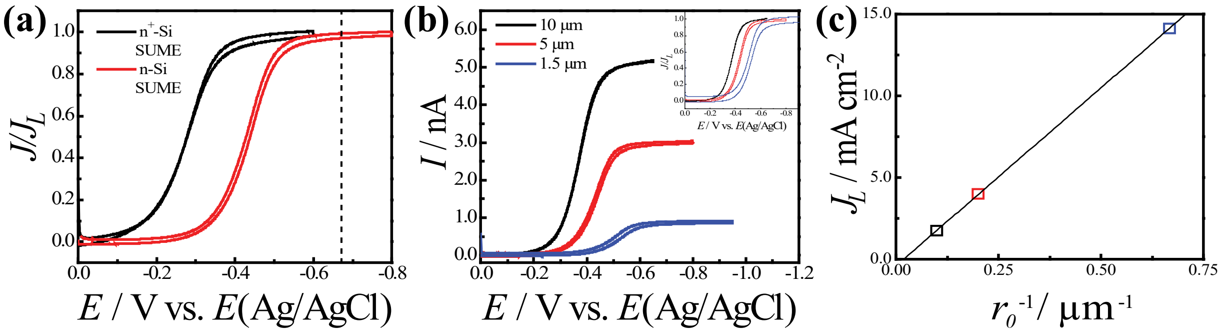

Figure 3.4. (a) Normalized experimental voltammetric responses of 5 μm n$^+$-Si and n-Si SUMEs to 2 mM Ru(NH$_3$)$_6^{3+}$. The dashed line indicates the conduction band location determined from separate impedance measurements. Scan rate: at 5 mV s^{-1} (b) Size-dependent voltammetry for n-Si SUMEs in 2 mM Ru(NH$_3$)$_6^{3+}$. The inset shows the normalized version of these plots. Scan rate: 5 mV s^{-1}. (c) Plot showing the mass transport-limited current density for the curves in (b) as a function of inverse radius.

thickness of 0.150 μm was employed. Doing so resulted in the background capacitance being more pronounced in the voltammetry for the smallest SUMEs.

Sensitivity of SUME Response Towards Conditions at the Semiconductor/Liquid Interface

Some aspects of the steady-state voltammetric response for the reduction of $Ru(NH_3)_6^{3+}$ changed over time. Figure 3.5a shows the normalized voltammetric responses for a non-degenerately doped n-Si SUMEs as a function of time after first immersion of the electrode in the aqueous electrolyte. Cyclic sweeps were performed every 40-50 min with the electrode held in solution at open circuit between scans. Over the course of nearly 5 h, the shape of the current-potential response was unchanged while the response shifted to progressively more negative potentials, suggesting either a change in k_{et} and/or a shift in E_{cb}. Using the potential where the current was half the value of the mass transport-limited current, $E_{1/2}$, as a metric, Figure 3.5b shows the voltammetric responses shifted by just 45 mV over nearly 5 h. Corresponding measurements with degenerately doped n^+-Si SUMEs also showed time-dependent voltammetric responses. However, the shape of the normalized current-potential response changed noticeably in addition to shifting towards more negative potentials, reminiscent of metal ultramicroelectrodes with a tunneling barrier at the electrode surface.[50]

Figure 3.6 tracks the effect of intentional oxidation of n-Si SUMEs on the voltammetric response for the reduction of $Ru(NH_3)_6^{3+}$. Following the process of Morrison,[51] a chemical surface oxide was grown quickly by soaking freshly etched n-Si SUMEs in aqueous solutions of $K_4Fe(CN)_6$ for 5 minutes. Figure 3.6a specifically presents impedance measurements of the potential-dependence of the squared reciprocal capacitance of macroscale n-Si electrodes before and after treatment. A freshly etched n-Si electrode yielded linear data over nearly two orders of magnitude that indicated the conduction band edge was positioned at $E_{applied} = -0.677 \pm 0.023$ V in 0.1 M KCl(aq). After treatment in the ferrocyanide solution, the reciprocal capacitance measurements showed a plateau at positive potentials, consistent with the formation of a thick surface oxide.[52] The x-axis intercept implied a significant band edge shift to $E_{applied} = -0.96$ V. Figure 3.6b shows the corresponding steady-state voltammetric responses for the reduction of $Ru(NH_3)_6^{3+}$ with n-Si SUMEs before and after treatment in the same manner. After surface oxidation, the steady-state voltammetric response of the n-Si SUME changed significantly. The

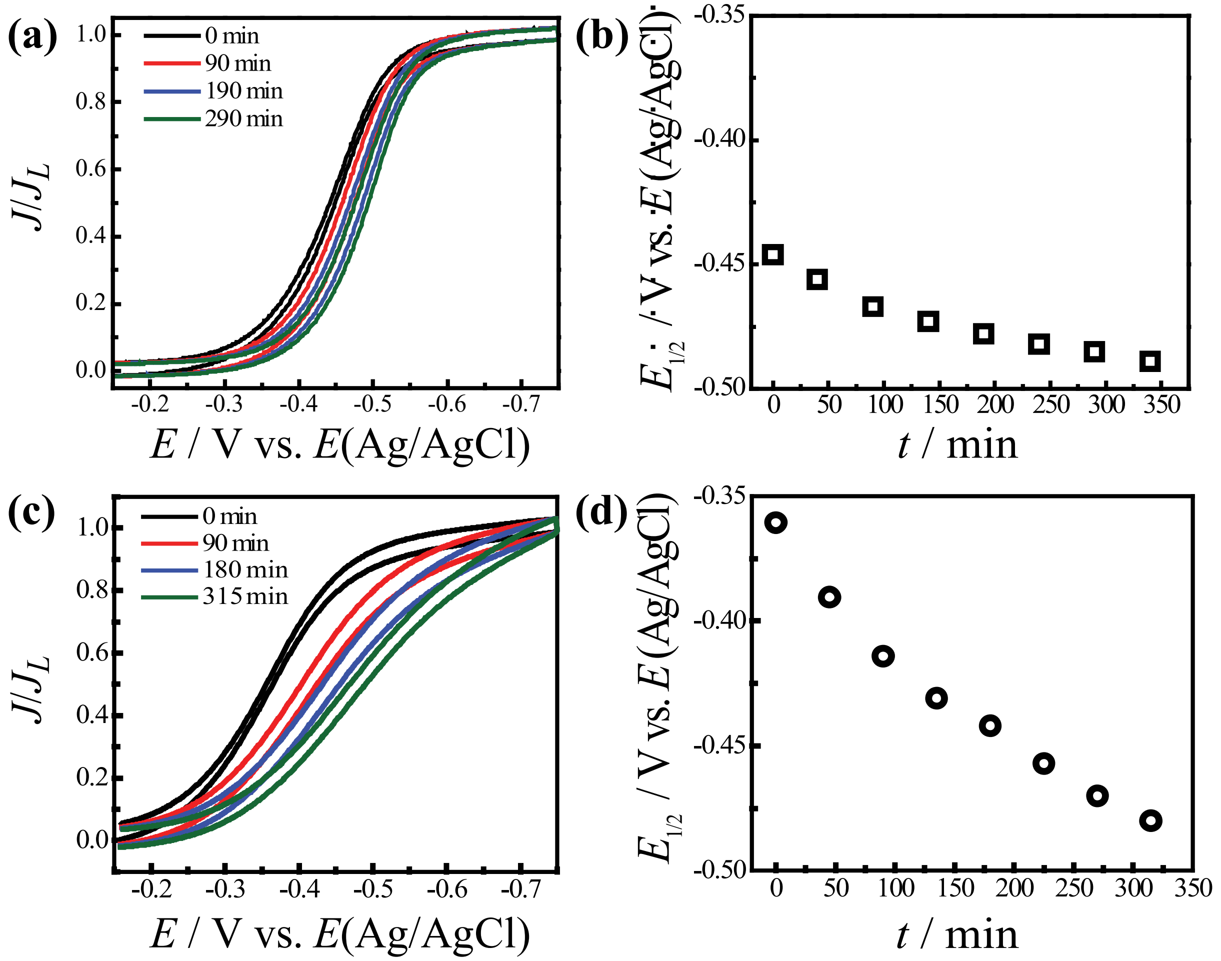

Figure 3.5. Time-dependence of normalized steady-state voltammetric responses of (a) non-degenerately doped and (c) degenerately doped Si SUMEs in 0.1 M KCl containing 2 mM $Ru(NH_3)_6^{3+}$ over time. Scan rate: 10 mV s^{-1}, r = 5 μm. Half-wave potentials of the SUME response for (b) non-degenerately doped and (d) degenerately doped Si SUMEs as a function of time.

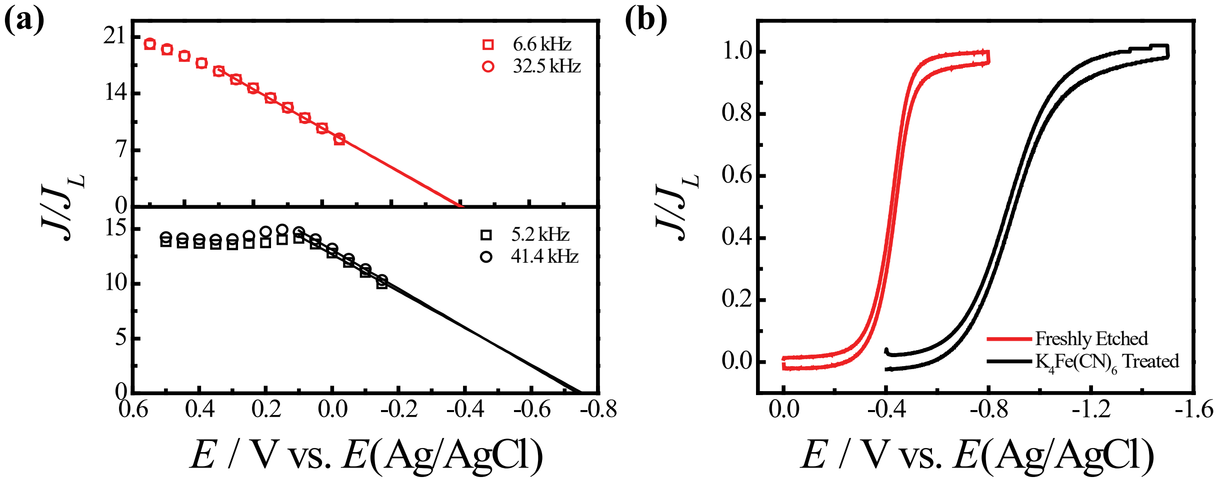

Figure 3.6. (a) Mott-Schottky plots for freshly etched and oxidized 0.19 cm^2 n-Si electrodes in 0.1 M KCl. (b) Voltammetric responses of freshly etched and treated non-degenerately doped n-Si SUMEs in 0.1 M KCl containing 2 mM $Ru(NH_3)_6^{3+}$. Scan rate: 10 mV s^{-1}, $r = 5$

voltammetric response shifted by more than 400 mV. More notably, the voltammetric shape broadened significantly.

Kinetic Analyses with SUMEs

For an ideal interface between a non-degenerate semiconductor and liquid electrolyte with a dissolved outer-sphere redox species, the rate of charge transfer should have a first order dependence on both the acceptor concentration in solution and the surface concentration of electrons, *eq 3.16*.[1]

$$J(E) = qk_{et}n_s(E)[A] \qquad (3.16)$$

The sensitivity of the voltammetric responses of n-Si SUMEs towards the reduction of $Ru(NH_3)_6^{3+}$ at different concentrations was determined. Figure 3.7 shows the steady-state voltammetric responses collected with a n-Si SUME with $r = 5$ µm over a range of concentrations of $Ru(NH_3)_6^{3+}$. At every concentration, a sigmoidal shape was obtained with the limiting currents within 5% of the expected mass transport-limited current predicted by *eq 3.15*. A test of *eq 3.16* requires observation of a linear correlation between current and concentration at a fixed potential. Accordingly, Figure 3.7b shows a plot of the measured current densities as a function of the concentration of $Ru(NH_3)_6^{3+}$ at several potentials near the onset of the voltammetric response, i.e. far from the mass transport-limited regime. At every potential, the current-concentration slope was linear but with a distinct magnitude due to the potential dependence of $n_s(E)$, in agreement with *eq* 3.16. Based on these observations, the steady-state voltammetric responses at n-Si SUMEs for three putatively outer-sphere redox couples were analyzed to determine their respective k_{et} values.

Table 3.2 summarizes the relevant electrochemical properties for $Ru(NH_3)_6^{3+}$, methylviologen dication (MV^{2+}), and $Co(sep)_3^{3+}$. The color-coded arrows and the dashed vertical line on the x-axis of Figure 3.8 denote $E°`$ for each redox species and E_{cb} in this electrolyte, respectively. The reorganization energies for heterogeneous reduction at n-Si listed in Table 3.2 were determined from published values of the reorganization energies for self-exchange reactions and the method described by Marcus (*vide supra*).[43] $Ru(NH_3)_6^{3+}$ and MV^{2+} have comparably small reorganization energies but differ substantially in $E°`$. $Co(sep)_3^{3+}$ has an intermediate $E°`$ value but a considerably larger reorganization energy. Figure 3.8 displays representative measurements of the steady-state voltammetric responses for n-Si SUMEs with r

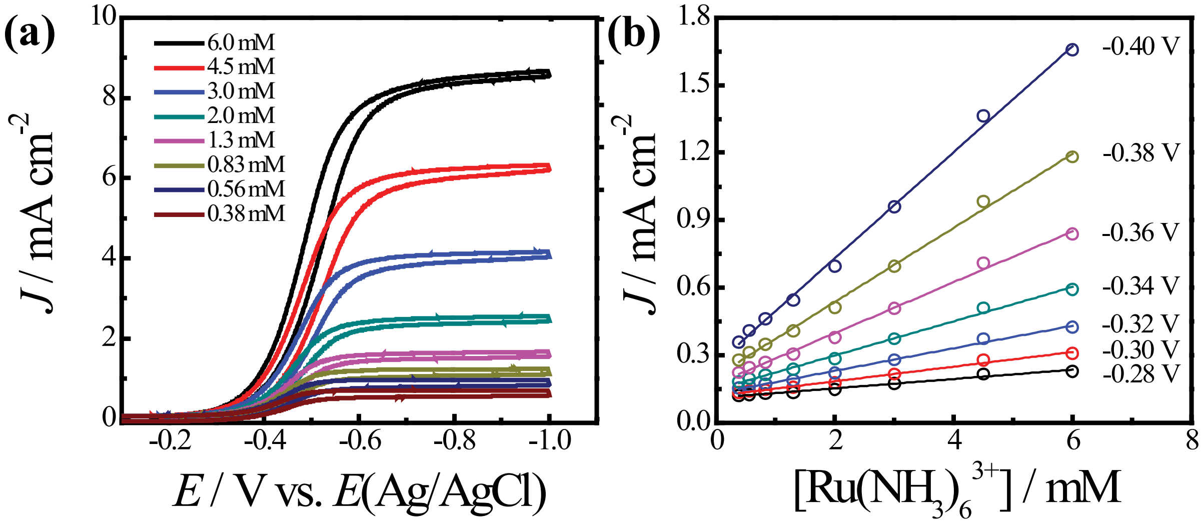

Figure 3.7. (a) Concentration-dependent voltammetric response to $Ru(NH_3)_6^{3+}$ for a 5 µm n-Si SUME. The scan rate was 10 mV s^{-1}. (b) Plot of the voltammetric wave position at $E_{applied}$ = -0.28, -0.30, -0.32, -0.34, -0.36, -0.38, and -0.40 V vs. E(Ag/AgCl) as a function of concentration.

= 5 μm for these redox couples, with overlaid fits from *eqs 3.1-3.7* with only k_{et} and γ as adjustable parameters (Table 3.2). Fits for the data for $Ru(NH_3)_6^{3+}$ and MV^{2+} were performed both without and with correction for the change in the fraction of the applied potential that was dropped within the semiconductor at potentials more negative than the flat-band potential (i.e. mild accumulation). That is, when the majority carrier density is large enough to make the space-charge capacitance comparable to or larger than the Helmholtz capacitance (Figure 3.3),[31, 35] a larger fraction of the applied potential is dropped at the semiconductor/liquid interface instead of within the semiconductor. For the 10^{15} cm^{-3} doping density used here, the effect is comparatively small. When this aspect was included, the fits yielded slightly lower k_{et} values (Table 3.2). Nevertheless, the fits for MV^{2+} and $Co(sep)_3^{3+}$ in Figure 3.8 yielded substantially smaller k_{et} values than for $Ru(NH_3)_6^{3+}$ (Table 3.2) regardless of the use of this correction.

The switching potential was determined to have an observable impact on the hysteresis of voltammograms measured with aqueous n-Si SUMEs. That is, while the switching potential has no influence on the shape of the voltammetric response in the forward scan, it systematically shifts the voltammetric response towards more positive potentials in the reverse scan (Figure 3.9). This phenomenon is ascribed to hydrogen implantation during the reduction of H^+ at Si interfaces.[29] It is unclear whether hydrogen implantation dopes the near surface of Si towards a more degenerate condition or shifts the band edges towards more positive potentials. Notably, although not shown in Figure 3.9, this effect was temporary. That is, continued cycling while keeping the switching potential less negative than -1.0 V resulted in an eventual restoration of voltammetry as shown in Figures 3.9a and 3.9b.

3.5. Discussion

The collective data speak to three points. First, SUMEs based on the shallow recessed disk motif show tractable steady-state voltammetric response characteristics. Second, such SUMEs are useful for assessing the interfacial character of semiconductor/solution contacts. Third, quantitative kinetic measurements with these SUMEs are readily possible. These points are discussed below.

Practical Attributes of Pinhole SUMEs

SUMEs comprised of an intentional pinhole with defined dimensions in a thin dielectric coating on a semiconductor substrate offers several tangible advantages for study. First, such

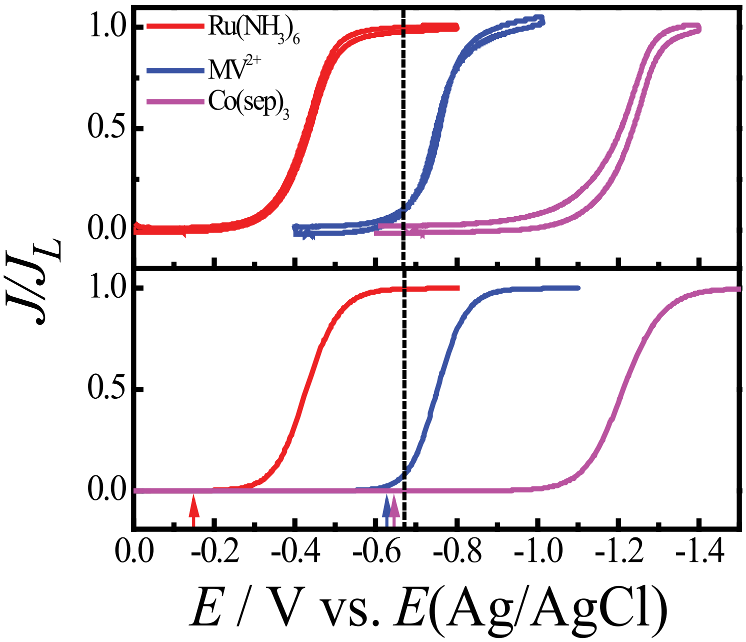

Figure 3.8. Normalized voltammetric responses of n-Si SUMEs with r = 5 μm in separate 0.1 M KCl aqueous solutions containing either (red) 2 mM $Ru(NH_3)_6^{3+}$, (blue) 2 mM MV^{2+}, or (purple) 2 mM $Co(sep)_3^{3+}$. The corresponding best fit line for each measurement is shown below each voltammogram. The dashed line indicates the conduction band edge determined from separate impedance measurements. Color-coded arrows show the standard potential for each redox couple. Scan rate: 5 mV s^{-1}.

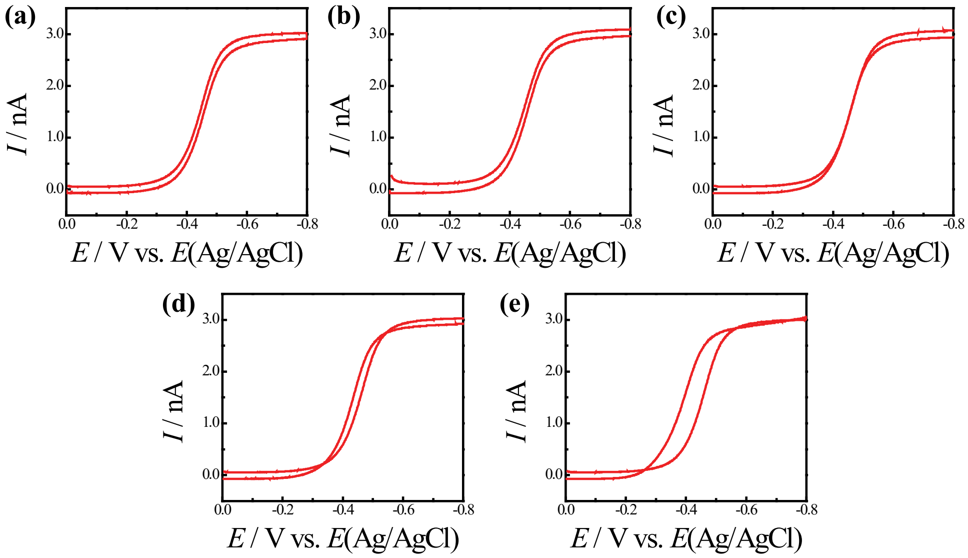

Figure 3.9. Voltammetric responses of a n-Si SUME (r = 5 μm) immersed in a 0.1 M KCl(aq) solution containing 2 mM $Ru(NH_3)_6^{3+}$ as a function of switching potentials: (a) -0.8 V (b) -1.0 V (c) -1.4 V (d) -1.8 V and (e) -2.2 V. Scan rate: 5 mV s^{-1}

SUMEs are naturally compatible with the use of semiconductor single-crystalline wafers/epifilms where the relevant material properties (e.g. doping levels/profiles, charge-carrier mobilities, crystallinity) are fully known. Accordingly, it was straightforward to compare and understand the response characteristics of degenerately and non-degenerately doped SUMEs in Figure 3.4. In contrast, such studies are not feasible with the more ‘traditional’ design of an ultramicroelectrode where a thin (semiconductor) filament is encased in an insulating shroud.[23, 30] This motif has been previously attempted with ZnO nanorod SUMEs with limited success.[53] The difficulty lies in knowing (and controlling) the semiconductor material properties precisely since they strongly influence heterogeneous charge transfer.[18, 22] Further, since the radius of thin semiconductor filament can strongly affect the shape of the depletion layer within the semiconductor in complex manners, a detailed understanding of current flow in a semiconductor filament ultramicroelectrode is substantially complicated.[54-55]

Second, the steady-state current-potential responses of the SUME platforms described here are readily interpretable. As detailed in Figure 3.2, the current-potential responses are dependent on k_{et}, r, $E^{\circ\prime}$, and E_{cb} based on the defined interplay between kinetic and mass transport-limited current fluxes at small disk electrodes. Interpretation of current-potential data is not always as easy or even feasible for other electrochemical strategies that probe current flow at small areas. For example, scanning electrochemical microscopy (SECM)[56-57] has been used to assess current flow at semiconductor/liquid contacts.[45] However, understanding the feedback current in SECM of semiconductors is made difficult by contributions from the lateral surface conductivity (i.e. along the plane of the semiconductor/electrolyte interface). That is, unlike in a metal, the charge conductivity of a semiconductor can be very different along the surface plane as compared to normal to the surface plane.[18] If sufficiently high, surface conductivity could cause the feedback current in SECM to be sensitive to redox processes (e.g. corrosion)[58-59] occurring away from the area probed by the tip. Since lateral surface conductivity of a semiconductor is strongly sensitive to the extent of depletion/inversion/accumulation in the semiconductor,[60-61] deciphering the SECM feedback response at a semiconductor is not straightforward.[62]

Third, the SUME platforms shown here are compatible with use in any solvent/electrolyte system. Although the studies here were limited to aqueous electrolytes, nothing prohibits the use of these SUMEs in non-aqueous electrolytes, where richer tests of charge-transfer theory are possible.[15, 63-64] In fact, the lower surface tension of non-aqueous solvents may facilitate better wetting into the recessed disk cavity.[42] This same aspect complicates the use of scanning electrochemical cell microscopy (SECCM)[65] for making small area semiconductor/electrolyte contacts. In that method, a small junction is made by wetting a substrate with a microscopic hanging liquid drop that has counter and reference electrodes, as first described by Koval and co-workers[66] and more recently advanced by Unwin and co-workers.[65] The difficulty in controlling the stability, wetting, and spreading of non-aqueous liquids is well-documented[67] and a major impediment to its use for studying the details of semiconductor electrochemistry.

Still, certain aspects of the pinhole SUME platform merit mention. First, the specific composition and design of the dielectric layer should be further developed. If other 'low *k*' dielectric films are employed, the background capacitance might be further be minimized. Fortunately, the pinhole SUME platform is compatible with any substrate, insulator (e.g. SiN_x, SiO_xN_y, SiO_2, Al_2O_3, PDMS, etc.), and deposition method (e.g. spin-coating, chemical vapor deposition, atomic layer deposition) provided the dielectric can be properly patterned. The dielectric layer used here resulted in a noticeable level of background capacitance, particularly for the smallest r value. Although not disruptive in this work, it is conceivable such a background capacitance could obfuscate the use of SUMEs with smaller r values. The issue is that thicker dielectric layers will decrease the background capacitance but necessarily increase the recession depth of the SUME. Deeper recession depths complicate mass transport since inside the recession mass transport will be linear rather than radial.[24, 27, 68] Although several works show that moderate recession depths ($d/r \sim 1$) are not prohibitive for quantitative study,[26, 68-69] further analyses are needed to determine when the normalized steady-state voltammetric responses appreciably deviate from the data fitting approach of Bond, Oldham, and Zoski. Specifically, more work is needed to determine what is the critical threshold d/r value that skews the data away appreciably from the response of an inlaid disk ultramicroelectrode. Nevertheless, any over-estimation of the k_{et} values reported here due to the recession is likely minimal. For a solution of 2 mM $Ru(NH_3)_6^{3+}$, the recessed SUMEs with $r = 5$ μm have a current density of 3.83 mA cm^{-2}, compared to the expected 3.98 mA cm^{-2} for an equivalent inlaid disk case.

Second, using the photolithographic fabrication approach, care was needed to avoid compromising the exposed semiconductor electrode surface. Specifically, a previous work similarly attempted to make arrays of ultramicroelectrodes on Si through a combination of photolithographic patterning and dry etching.[70] However, they reported behavior more consistent with metal electrodes rather than the unique characteristics of a non-degenerate semiconductor electrode detailed here. Issues in their fabrication, including reliance on destructive dry etches, likely destroyed the electronic quality of their semiconductor surface. In this work, the semiconductor surfaces were protected during the low-selectivity reactive-ion etching (RIE) process by leaving a thin insulting layer on top of the SUME active area and wet-etching it off before the first measurement. Purposely leaving this thin layer prevented unintentional dry etching of the SUME surface and allowed wet-etching to occur without appreciable undercutting. The tractability of the measurements made with the SUME platforms suggests these preventative steps preserved the integrity of the surface in two ways. First, the current for the reduction of outer-sphere redox probes was first-order with concentration. Second, the ideality factors obtained with the aqueous contacts are equivalent or lower than ideality factors measured with macroscopic electrodes under similar conditions.[71]

Sensitivity of the SUME Responses Towards the Semiconductor/Solution Interface

The measured steady-state current-potential responses for the reduction of $Ru(NH_3)_6^{3+}$ at n-Si SUMEs shown here acted as a probe of the Si/water interface. The subtle, negative shift in the voltammetry in Figure 3.5 strongly implies that the surface of n-Si in water progressively changed over time. The most plausible cause was the growth of an appreciable surface oxide, as the oxidation of Si in water is well known.[72] Chemical oxidation of non-degenerate Si by water yields a ~2 Å oxide (SiO_x) over 300 min[72] which could act as an additional tunneling barrier that slows heterogeneous charge transfer. Assuming that the observed 45 mV shift corresponded to solely a diminution in k_{et}, that shift implied a decrease in k_{et} by a factor of ~5. Such attenuation is consistent with tunneling through a thin SiO_x layer.[73,74] The changes seen with n^+-Si SUMEs further corroborates the contention that the voltammetric changes tracked the slow growth of surface oxide. The current flow at degenerately doped semiconductor interfaces is predominantly by tunneling of majority carriers through the space-charge region rather than thermionic emission at the band edge.[22] Accordingly, such current flow should be strongly affected by introducing another tunneling process. That is, a surface oxide imposes a second tunneling process in series, thereby lowering the probability that a charge-carrier escapes from the semiconductor into the solution and introducing an additional overpotential penalty for attaining the same current density. If the slow growth of surface oxide was instead just changing E_{cb}, tunneling through the space-charge layer within the semiconductor would be largely unaffected since small changes in band edge energetics do not alter the space-charge layer thickness. Hence, the voltammetric responses from both the non-degenerately and degenerately doped Si SUMEs are consistent with a thin surface oxide growing over time.

In contrast, the voltammetry data in Figure 3.6 for n-Si SUMEs illustrate the response characteristics when a thick surface oxide is present. The short 5 min immersion in aqueous ferrocyanide significantly distorted the steady-state voltammetry for the reduction of $Ru(NH_3)_6^{3+}$. In this case, the voltammetry shifted substantially, implying more than an order of magnitude attenuation of k_{et}. The clear change in γ further indicated that this oxide sufficiently impeded charge transfer and the resultant voltammetric response did not yield any info on pristine Si/water interfaces. In total, the combined data of Figures 3.5 and 3.6 argue that the electrochemical response for the reduction of $Ru(NH_3)_6^{3+}$ is strongly and tractably sensitive to the evolving chemistry of a Si/water interface. Further, these data indicate that over short timescales (e.g. $t < 5$ min), the voltammetric responses of freshly etched n-Si SUMEs for the reduction of outer-sphere redox probes like $Ru(NH_3)_6^{3+}$ are sufficiently stable to permit analyses of charge-transfer kinetics, even in water.

Quantitative Kinetic Measurements with SUMEs

The utility of SUMEs for kinetic measurements are clear in the presented data. The pinhole SUME platform enabled reliable, rapid, and verifiable measurement of k_{et} for dissolved redox couples from simple steady-state voltammetry. Interpretable data was even obtained with dilute concentrations as low as 10^{-4} M. For macroscopic electrodes, mass-transfer resistance even at 10^{-3} M is often severe enough to distort the current-potential response, complicating measurements with sparingly soluble redox couples. With SUMEs and the data fitting approach presented here, the interplay between charge-transfer kinetics and mass transfer is sufficiently defined that quantitative measurements are possible at any concentration.

The magnitude of the value of k_{et} measured here (10^{-16} cm^4 s^{-1}) stands in contrast to the much smaller (10^{-22} cm^4 s^{-1}) rate constant value for the reduction of $Ru(NH_3)_6^{3+}$ at Si electrodes in water previously inferred from microwave photoconductivity measurements.[75] However, the measurements here were direct, reproducible, and conformed well to expectations from the Marcus-Gerischer framework for heterogeneous charge transfer,[38, 76]

$$k_{et} = k_{et,\max} e^{\frac{-\left(\left(E_{cb} - E^{0'}\right) + \lambda_{sc}\right)^2}{4\lambda k_B T}} \qquad (3.17)$$

where $k_{et,max}$, is the rate constant at optimal exoergicity. The value of $k_{et,max}$ is believed to have a value of 10^{-16} - 10^{-17} cm^4 s^{-1}.[37] Given the reorganization energy, λ_{sc}, for $Ru(NH_3)_6^{3+}$ in water (Table 3.2) and the value of E_{cb} relative to $E^{\circ`}$, the measured rate constant for electron transfer from the band edge of freshly etched Si to freely dissolved $Ru(NH_3)_6^{3+}$ in water is expected to be very close to $k_{et,max}$, consistent with what was measured here. This point merits special attention since it counters a long-standing conventional wisdom in semiconductor electrochemistry. Specifically, the instability of Si in water has long been assumed to preclude the possibility of tractable and quantitative voltammetric measurement of charge-transfer kinetics. This measurement, in conjunction with the meta-stability of the Si/water interface (*vide supra*), clearly establish that voltammetry with n-Si electrodes yields results in accord with the dominant microscopic theory of charge transfer.

Measurements of k_{et} for MV^{2+} and $Co(sep)_3^{3+}$ are also generally in agreement with *eq 3.17* but their interpretation is more nuanced. Both redox couples elicited voltammetric responses that were shifted to even more negative potentials than the response for $Ru(NH_3)_6^{3+}$. This observation implies substantially smaller values of k_{et} for both these redox couples, in accord with the predictions from *eq 3.17* since both the reduction of MV^{2+} and $Co(sep)_3^{3+}$ occur with a much smaller driving force than their respective λ_{sc} values (Table 3.2). Still, the specific values of each respective rate constant are convoluted because of two factors. First, both have some degree of chemical 'interference'. The potential window for the voltammetric response for the $MV^{2+/+}$ process was limited by the onset of the current response for the $MV^{+/0}$ reduction. Separately, the current response for the $Co(sep)_3^{3+/2+}$ redox couple was shifted sufficiently negative that concurrent cathodic hydrogenation of Si likely occurred to some extent (i.e. H_2 diffuses into Si surfaces at extreme negative potentials in water).[77-78] We separately saw evidence of this when the n-Si SUMEs were biased more negative than -1.0 V (Figure 3.9). This process likely contributed to the notable hysteresis in the voltammetric response for the $Co(sep)_3^{3+/2+}$ couple. Second, some or all of the voltammetric responses for the reduction of MV^{2+} and

$Co(sep)_3^{3+}$ occurred at potentials negative of the conduction band edge, i.e. the n-Si SUMEs were operating under progressively more accumulated conditions. In this regime, the potential-dependence of n_s is more complex since the Boltzmann approximation is less accurate and the Fermi-Dirac function must be used. That is, the applied potential is distributed across both the space charge layer of the semiconductor and the double layer in solution, imparting some potential dependence to E_{cb}. The presented analyses apply rigorously to non-degenerately doped semiconductors operating under depletion and mild accumulation conditions but it is less clear how the specific shapes of the steady-state voltammetric responses should appear when the electrode becomes strongly accumulated. Accordingly, more precise estimates of the values of k_{et} for the reduction $Co(sep)_3^{3+}$ specifically require further theoretical development.

3.6. Conclusions

This work describes a comprehensive overview of the operation of non-degenerately doped SUMEs functioning under depletion conditions and a basis for evaluating their response characteristics. Akin to metal ultramicroelectrodes, SUMEs have the familiar steady-state current-potential profiles but their interpretation requires a kinetic framework different than the Butler-Volmer formalism. With this proviso and unlike the current responses from macroscopic semiconductor electrodes, the electrochemical behaviors of SUMEs towards putative outer-sphere redox couples in solution are understandable. The utility of these platforms for enabling voltammetry to inform on the static and dynamic features of semiconductor/liquid junctions has been demonstrated. Continued work in the following areas are necessary to further advance the analytical utility of pinhole SUMEs for systems based on semiconductor/liquid interfaces. First, fabrication of SUMEs with values of r smaller than the average separation distance between surface traps/defects could increase the probability of realizing semiconductor electrodes with $\gamma \rightarrow 1$. Second, global fitting of SUME steady-state voltammetric responses for multiple outer-sphere redox couples should be explored to determine whether semiconductor band edge energetics can be identified without requiring separate impedance-based measurements. Third, further refinement of the modeling for fitting data under strong accumulation and strong inversion conditions is warranted. Doing so would further enable more comprehensive tests of Marcus theory at semiconductor/solution interfaces. Additionally, the present work only describes the current-potential responses of SUMEs in the dark. Under illumination, the voltammetric characteristics of pinhole SUMEs should also prove useful if their respective sensitivities towards the method of photogeneration, the interfacial charge-transfer kinetics, and the transport of charges can be readily distinguished. Such data would be germane to the field of photoelectrochemistry generally and potentially the operation of discrete semiconductor photocatalysts specifically.

3.7. References

1. Gerischer, H. *Electrochim. Acta* **1990,** *35*, 1677.

2. Meek, R. L.; Schumaker, N. E. *J. Electrochem. Soc.* **1972,** *119*, 1148.

3. Youtsey, C.; Adesida, I.; Bulman, G. *Appl. Phys. Lett.* **1997,** *71*, 2151.

4. Minks, B. P.; Vanmaekelbergh, D.; Kelly, J. J. *J. Electroanal. Chem.* **1989,** *273*, 133.

5. Rothberg, J. M.; Hinz, W.; Rearick, T. M.; Schultz, J.; Mileski, W.; Davey, M.; Leamon, J. H.; Johnson, K.; Milgrew, M. J.; Edwards, M.; Hoon, J.; Simons, J. F.; Marran, D.; Myers, J. W.; Davidson, J. F.; Branting, A.; Nobile, J. R.; Puc, B. P.; Light, D.; Clark, T. A.; Huber, M.; Branciforte, J. T.; Stoner, I. B.; Cawley, S. E.; Lyons, M.; Fu, Y. T.; Homer, N.; Sedova, M.; Miao, X.; Reed, B.; Sabina, J.; Feierstein, E.; Schorn, M.; Alanjary, M.; Dimalanta, E.; Dressman, D.; Kasinskas, R.; Sokolsky, T.; Fidanza, J. A.; Namsaraev, E.; McKernan, K. J.; Williams, A.; Roth, G. T.; Bustillo, J. *Nature* **2011,** *475*, 348.

6. Steinhoff, G.; Hermann, M.; Schaff, W. J.; Eastman, L. F.; Stutzmann, M.; Eickhoff, M. *Appl. Phys. Lett.* **2003,** *83*, 177.

7. Fujishima, A.; Honda, K. *Nature* **1972,** *238*, 37.

8. Gratzel, M. *Nature* **2001,** *414*, 338.

9. Smith, W. A.; Sharp, I. D.; Strandwitz, N. C.; Bisquert, J. *Energy Envir. Sci.* **2015,** *8*, 2851.

10. Kohl, P. A.; Bard, A. J. *J. Electrochem. Soc.* **1979,** *126*, 598.

11. Kohl, P. A.; Bard, A. J.. *J. Am. Chem. Soc.* **1977,** *99*, 7531.

12. Frank, S. N.; Bard, A. J. *J. Am. Chem. Soc.* **1975,** *97*, 7428.

13. Nagasubramanian, G.; Wheeler, B. L.; Fan, F. F.; Bard, A. J. *J. Electrochem. Soc. 129*, 1742.

14. Chazalviel, J. N.; Truong, T. B. *J. Electroanal. Chem.* **1980,** *114*, 299.

15. Koval, C. A.; Torres, R. *J. Am. Chem. Soc.* **1993,** *115*, 8368.

16. Koval, C. A.; Austermann, R. L.; Turner, J. A.; Parkinson, B. A. *J. Electrochem. Soc.* **1985,** *132*, 613.

17. Koval, C. A.; Austermann, R. L. *J. Electrochem. Soc.* **1985,** *132*, 2656.

18. Sze, S. M.; Ng, K. K., *Physics of Semiconductor Devices*. 3rd ed.; John Wiley & Sons: Hoboken, NJ, 2006.

19. Streetman, B. G.; Banerjee, S. K., *Solid State Electronic Devices*. 6th ed.; Pearson Education: Upper Saddle River, NJ, 2006.

20. Decker, F.; Fracastoro-Decker, M.; Badawy, W.; Dolbhafter, K.; Gerischer, H. *J. Electrochem. Soc.* **1983,** *130*, 2173.

21. Bruckenstein, S.; Rosamilia, J. M.; Miller, B. *J. Phys. Chem.* **1985,** *89*, 677.

22. Koval, C. A.; Howard, J. N. *Chem. Rev.* **1992,** *92*, 411.

23. Zoski, C. G. *Electroanalysis* **2002,** *14*, 1041.

24. Bond, A. M.; Luscombe, D.; Oldham, K. B.; Zoski, C. G.. *J. Electroanal. Chem.* **1988,** *249*, 1.

25. Oldham, K. B.; Myland, J. C.; Zoski, C. G.; Bond, A. M. *J. Electroanal. Chem.* **1989,** *270*, 79.

26. Oldham, K. B. *Anal. Chem.* **1992,** *64*, 646.

27. Bartlett, P. N.; Taylor, S. L. *J. Electroanal. Chem.* **1998,** *453*, 49.

28. Amatore, C.; Oleinick, A. I.; Svir, I. *Anal. Chem.* **2009,** *81*, 4397.

29. Bond, A. M.; Oldham, K. B.; Zoski, C. G. *J. Electroanal. Chem.* **1988,** *245*, 71.

30. Sun, Y. Y. T.; Mirkin, M. V. *Anal. Chem.* **2016,** *88*, 11758.

31. Royea, W. J.; Kruger, O.; Lewis, N. S. *J. Electroanal. Chem.* **1997,** *438*, 191.

32. Morrison, S. R., *Electrochemistry at Semiconductor and Oxidized Metal Electrodes*. 1 ed.; Springer US: New York, 1980.

33. Zettler, R. A.; Cowley, A. M. *IEEE Trans. Electron Dev.* **1969,** *16*, 58.

34. Lepselter, M. P.; Sze, S. M. *Bell Labs Tech. J.* **1968,** *47*, 195.

35. Natarajan, A.; Oskam, G.; Searson, P. *J. Phys. Chem. B* **1998,** *102*, 7793.

36. Hens, Z.; Gomes, W. P. *J. Phys. Chem. B* **1997,** *101*, 5814.

37. Lewis, N. S. *J. Phys. Chem. B* **1998,** *102*, 4843.

38. Marcus, R. A. *J. Chem. Phys.* **1965,** *43*, 679.

39. Frese, K. W. *J. Phys. Chem.* **1981,** *85*, 3911.

40. Royea, W. J.; Hamann, T. W.; Brunschwig, B. S.; Lewis, N. S. *J. Phys. Chem. B* **2006,** *110*, 19433.

41. Vijaikanth, V.; Li, G. C.; Swaddle, T. W. *Inorg. Chem.* **2013,** *52*, 2757.

42. *CRC Handbook of Chemistry and Physics*. 99 ed.; CRC Press: 2018.

43. Marcus, R. A. *J. Phys. Chem.* **1991,** *95*, 2010.

44. Green, M. A.; Keevers, M. J. *Prog. Photovoltaics* **1995,** *3*, 189.

45. Horrocks, B. R.; Mirkin, M. V.; Bard, A. J. *J. Phys. Chem.* **1994,** *98*, 9106.

46. Li, Y. X.; Bergman, D.; Zhang, B. *Anal. Chem.* **2009,** *81*, 5496.

47. Lanyon, Y. H.; Arrigan, D. W. M. *Sens. Actuators B Chem.* **2007,** *121*, 341.

48. Lanyon, Y. H.; De Marzi, G.; Watson, Y. E.; Quinn, A. J.; Gleeson, J. P.; Redmond, G.; Arrigan, D. W. M. *Anal. Chem.* **2007,** *79*, 3048.

49. Tsushima, M.; Tokuda, K.; Ohsaka, T. *Anal. Chem.* **1994,** *66*, 4551.

50. Hill, C. M.; Kim, J.; Bodappa, N.; Bard, A. J. *J. Am. Chem. Soc.* **2017,** *139*, 6114.

51. Loo, B. H.; Frese, K. W.; Morrison, S. R. *Surf. Sci.* **1981,** *109*, 75.

52. Groner, M. D.; Koval, C. A. *J. Electroanal. Chem.* **2001,** *498*, 201.

53. Rodman, S.; Spitler, M. T. *J. Phys. Chem. B* **2000,** *8*, 9438.

54. Foley, J. M.; Price, M. J.; Feldblyum, J. I.; Maldonado, S. *Energy Environ. Sci.* **2012,** *5*, 5203.

55. Hagedorn, K.; Forgacs, C.; Collins, S.; Maldonado, S. *J. Phys. Chem. C* **2010,** *114*, 12010.

56. Zoski, C. G. *J. Electrochem. Soc.* **2016,** *163*, H3088.

57. Amemiya, S.; Bard, A. J.; Mirkin, M. V.; Unwin, P. R. *Annu. Rev. Anal. Chem.* **2008,** *1*, 95.

58. Mandler, D.; Bard, A. J. *J. Electrochem. Soc.* **1990,** *137*, 2468.

59. Zhang, J.; Jia, J.; Han, L.; Yuan, Y.; Tian, Z. Q.; Tian, Z. W.; Zhan, D. *J. Phys. Chem. C* **2014,** *118*, 18604.

60. Shiue, C. C.; Sah, C. T. *Phys. Rev. B* **1979,** *19*, 2149.

61. Hongtao, Y.; Hidekazu, S.; Ye, J.; Sungjae, Y.; Hasniah, A.; Atsushi, T.; Masashi, K.; Yoshihiro, I. *J. Am. Chem. Soc.* **2010,** *132*, 18402.

62. Shreve, G. A.; Karp, C. D.; Pomykal, K.; Lewis, N. S. *J. Phys. Chem.* **1995,** *99*, 5575.

63. Fajardo, A. M.; Lewis, N. S. *Science* **1996,** *274*, 969.

64. Fajardo, A. M.; Lewis, N. S. *J. Phys. Chem. B* **1997,** *101*, 11136.

65. Ebejer, N.; Schnippering, M.; Colburn, A. W.; Edwards, M. A.; Unwin, P. R. *Anal. Chem.* **2010,** *82*, 9141.

66. Howard, J. N.; Koval, C. A. *Anal. Chem.* **1991,** *63*, 2777.

67. Sharel, P. E.; Kang, M.; Wilson, P.; Meng, L. C.; Perry, D.; Basile, A.; Unwin, P. R. *Chem. Commun.* **2018,** *54*, 3053.

68. Baranski, A. S. *J. Electroanal. Chem.* **1991,** *307*, 287.

69. Shao, Y. H.; Mirkin, M. V.; Fish, G.; Kokotov, S.; Palanker, D.; Lewis, A. *Anal. Chem.* **1997,** *69*, 1627.

70. Li, T.; Dong, H.; Fu, X.; He, M.; Li, Y.; Hu, W. *Small* **2014,** *10*, 878.

71. Hamann, T. W.; Lewis, N. S. *J. Phys. Chem. B* **2006,** *110*, 22291.

72. Morita, M.; Ohmi, T.; Hasegawa, E.; Kawakami, M.; Ohwada, M. *J. Appl. Phys.* **1990,** *68*, 1272.

73. Bard, A.; Faulkner, L., *Electrochemical Methods: Fundamentals and Applications*. 2nd ed.; John Wiley & Sons: New York, 2001.

74. Depas, M.; Vanmeirhaeghe, R. L.; Laflere, W. H.; Cardon, F. *Solid·State Electron.* **1994,** *37*, 433.

75. Peter, L.; Ushiroda, S. *J. Phys. Chem. B* **2004,** *108*, 2660.

76. Royea, W. J.; Fajardo, A. M.; Lewis, N. S. *J. Phys. Chem. B* **1997,** *101*, 11152.

77. Mandal, K. C.; Ozanam, F.; Chazalviel, J. N. *Appl. Phys. Lett.* **1990,** *57*, 2788.

78. Philipsen, H. G. G.; Ozanam, F.; Allongue, P.; Kelly, J. J.; Chazalviel, J. N. *Surf. Sci.* **2016,** *644*, 180.

CHAPTER 4

Quantitative Analysis of Semiconductor Electrode Voltammetry: Theoretical and Operational Framework for Understanding Data from Semiconductor Ultramicroelectrodes (SUMEs)

4.1. Introduction

The operation of a semiconductor electrode immersed in a liquid electrolyte is germane to the design of artificial photosynthetic reactors.[1-4] A detailed understanding of heterogeneous charge transfer at the semiconductor/electrolyte contact is accordingly useful. By definition, the current-potential (*J*-*E*) responses of a properly constructed 3-electrode cell employing a semiconductor working electrode are rich with information on the semiconductor, solution, and their interface. However, deciphering and interpreting voltammetric responses in even the simplest semiconductor electrochemical systems is challenging because the data are a convolution of effects from mass transport, electrostatics, charge-transfer kinetics, and (possibly) corrosion/oxidation reactions.[5-13] Accordingly, insight on the semiconductor/electrolyte interface is typically sought through indirect electroanalytical methods such as impedance[10, 14] or through alternative approaches (e.g. scanning probe microscopies,[15-16] time-resolved luminescence,[17-19] and X-ray spectroscopies[20-22]).

Semiconductor ultramicroelectrodes (SUMEs) are platforms that potentially simplify interpreting voltammetry.[23-24] Specifically, SUMEs can yield steady-state cyclic voltammetric data which is informative on semiconductor/solution interfaces. The advantages of SUMEs stem from the fact that the radial mass transport of species in the electrolyte to microelectrodes is extremely well-defined[25-26] and that the measured currents are sufficiently small to avoid *iR* losses even in resistive solutions,[27] facilitating direct analysis.

In a previous report,[23] the general efficacy of n-type SUMEs for the reduction of a series of putatively outer-sphere redox couples in water was reported. The standard potential, $E°`$, of each redox couple was presumably positive enough to render n-Si SUMEs in some level of depletion.

Through a simplified framework that assumed that the concentration of majority carriers (electrons) at the surface, n_s, is a simple function of the applied potential, heterogeneous charge-transfer rate constants for SUMEs in depletion were estimated directly from the corresponding *J-E* data. The inferred values were nominally in line with existing microscopic charge-transfer theories,[28-32] validating the SUME platform and illustrating the possibility of more precise studies of heterogeneous charge transfer. However, not all of the data could be precisely fit, particularly when the SUMEs operated under accumulation conditions. Specifically, a phenomenological 'non-ideality' factor was used to gauge the validity of the assumption, as is common in the electrochemical and solid-state semiconductor heterojunction literatures.[29, 33-36]

The intent of this report is to describe how the analysis of the *J-E* data from SUMEs in the absence of illumination does not require 'non-ideality' factors or the assumption that k_{et} and n_s are wholly independent of potential. Instead, the form of the *J-E* responses has direct relations to all identifiable physicochemical properties of the semiconductor, the electrolyte, and their interface. Herein, this report presents the relevant theory and methodology needed to generate working curves of *J-E* data for an n-type SUME. This study details explicitly how changes in various prominent physical parameters including $E°$`, the conduction band edge (E_{cb}), the reorganization energy for charge transfer (λ_{sc}), and surface state density (N_{ss}) control the observable, steady-state voltammetric responses. In addition, the influence of less intuitive parameters such as electrolyte concentration, semiconductor doping density (N_d), surface state potential (E_{ss}), and surface state capacitance (C_{ss}) are described. A brief demonstration of how this cumulative approach enables the analysis of Si SUME voltammetry in accumulation is presented.

4.2. Framework

The sigmoidal, steady-state voltammetric behavior of an inlaid-disk SUME at slow scan rates is dictated by the interplay of kinetic consumption at the semiconductor/electrolyte interface and radial diffusional replacement of redox species from the bulk solution. This competition affords estimation of charge-transfer kinetics through the analytical expression advocated by Zoski, Bond, and Oldham,[25]

$$\frac{J}{J_{L,c}} = \frac{1}{\theta\left[1+\frac{\pi}{\kappa\theta}\left(\frac{2\kappa\theta+3\pi}{4\kappa\theta+3\pi^2}\right)\right]} \qquad (4.1)$$

where $J_{L,c}$ is the mass transport-limited cathodic current and θ & κ are dimensionless numbers that relate to the diffusion of the redox species and the governing rate constants at the electrode/electrolyte interface, respectively. The expressions for θ & κ contain the diffusion coefficients of the oxidized and reduced forms of the redox couple (D_A and D_{A-}, respectively) and the rate constants for the reduction of A to A^- & the oxidation of A^- to A (k_f and k_b, respectively).

$$\theta = 1 + \frac{D_A}{D_{A^-}} \frac{k_b}{k_f} \tag{4.2}$$

$$\kappa = \frac{\pi r k_f}{4 D_A} \tag{4.3}$$

These expressions are general but can be specifically related to any electrode/electrolyte interface through elaboration of k_f and k_b. For an n-type SUME, k_f and k_b can be defined in the following way assuming only charge transfer through the conduction band,

$$k_f = k_{et} n_s \tag{4.4a}$$

$$k_b = k_{et} n_{s,0} \tag{4.4b}$$

where $n_{s,0}$ is the surface density of electrons at $E^{\circ`}$ and k_{et} has units of $cm^4\ s^{-1}$. A key insight for understanding data from SUMEs is that both k_{et} and n_s can depend on the applied potential in complex yet predictable manners. The *general* dependence of each term with applied potential is detailed for the first time below.

The General Potential Dependence of n_s

The value of n_s depends explicitly on the potential drop within the space charge layer of the semiconductor, i.e. the difference between the E_F and the flat-band potential, E_{fb}. Experimentally, E_F can be adjusted by an applied potential, $\Delta E_{applied}$. In a semiconductor electrode operating under depletion conditions, the expectation is that E_F changes by the exact magnitude of $\Delta E_{applied}$. This statement is tantamount to stating $\Delta E_{applied}$ is dropped only across the space-charge region within the semiconductor.

This assumption is generally invalid for most systems in two ways. First, as has been noted in several different works across the past 3+ decades,[37-40] the applied potential (in a three electrode cell) is formally partitioned across the semiconductor, the electrolyte, and possibly their interface. Specifically, for an ideal, planar semiconductor/liquid contact with no surface layer, $\Delta E_{applied}$ is always distributed across the space-charge layer in the semiconductor, the double (Helmholtz) layer of ions at the semiconductor/solution interface, and the outer, diffuse layer of ions (Figure 4.1).[39] The fraction of $\Delta E_{applied}$ that is dropped across each region is given by *eq. 4.5*,

$$1 = \frac{\Delta E_{sc}}{\Delta E_{applied}} + \frac{\Delta E_{dl}}{\Delta E_{applied}} + \frac{\Delta E_{H}}{\Delta E_{applied}} \tag{4.5}$$

Determination of the magnitude of each fractional potential drop requires knowledge of each region's ability to store charge, Q, as a function of potential, i.e. their respective capacitance values since $C \equiv Q/\Delta E$.

Since the capacitances of each region (C_{sc}, C_H, and C_{dl}, respectively) are physically and effectively in series to one another (Figure 4.1), the total electrode capacitance, C_{total}, is given by *eq. 4.6*,

$$1 = \frac{C_{total}}{C_{sc}} + \frac{C_{total}}{C_{H}} + \frac{C_{total}}{C_{dl}} \tag{4.6}$$

The similar functional forms of *eqs. 4.5* and *4.6* indicate that the fractional potential drop across each region is equal to the fractional contribution of the capacitance of each region to the total capacitance. An equivalent statement is that the sum of the specific charges stored in each region must always equal the total charge applied to the system by the principle of charge conservation.[37, 39] *Eqs. 4.5* and *4.6* state that when C_{sc} is much smaller than C_{dl} and C_H, $C_{total}/C_{sc} \approx 1$ and therefore $\frac{\Delta E_{sc}}{\Delta E_{applied}} \approx 1$. In this case, $\Delta E_{applied}$ directly correlates with E_F. However, when C_{sc} is larger than or even comparable to C_{dl} or C_H, $\Delta E_{applied}$ will not directly correlate with E_F. Hence, to identify E_F accurately within the semiconductor at any applied potential so as to gauge n_s throughout a voltammogram, knowledge of all capacitance values is needed.

Expressions that generally describe how C_H and C_{dl} are influenced by solvent type and ionic strength are available.[41] In this work, the Gouy-Chapman-Stern model was employed with following expressions,[41]

$$C_H = \frac{\varepsilon_{interface}\varepsilon_0}{\delta} \tag{4.7}$$

$$C_{dl} = \frac{1}{\cosh\left(\frac{q\Delta E_{dl}}{2k_B T}\right)\sqrt{\frac{2\varepsilon_{CH_3OH}\varepsilon q^2 \mu}{k_B T}}} \approx \frac{1}{\sqrt{\frac{2\varepsilon_{CH_3OH}\varepsilon_0 q^2 \mu}{k_B T}}} \qquad (4.8)$$

where δ is the thickness of the Helmholtz layer, ε_{CH_3OH} is the relative dielectric constant for methanol, $\varepsilon_{interface}$ is the relative dielectric constant of the electrode/electrolyte interface, and μ is the ionic strength for a 1:1 salt. In these expressions, the simplifying assumption is that neither capacitance depends appreciably on the applied potential.

In contrast, the space charge capacitance is considered to change with applied potential. However, notably, the simple expressions for C_{sc} commonly used for semiconductor electrodes that assume Boltzmann statistics apply for carrier concentrations are not generally accurate at all applied potentials. Rather, the formal description of the space charge capacitance is given by *eq. 4.9*,[42]

$$C_{sc} = \sqrt{k_B T N_d \varepsilon\varepsilon_0}\,\frac{\delta F_s}{\delta E} \qquad (4.9)$$

where F is a unit-less function that describes the occupancy of majority carriers (electrons) at the majority carrier (conduction) band edge.[42] F_s is this function evaluated at the semiconductor/solution interface. This expression is valid under any applied bias in depletion and accumulation provided the value of F_s can be determined.

The second aspect that complicates the relation between the applied potential and n_s is that Boltzmann statistics do not universally apply. Rather, the value of n_s is explicitly defined as the integral of the product of the density of states ($N(E)$) at each potential (E) and the occupancy of those states ($F(E)$) at each potential over the potential range spanned by the conduction band. For an n-type electrode, the integral that describes n_s is the Fermi-Dirac integral of 1/2 order,

$$n_s = \int_{E_{cb}}^{-\infty} N(E)F(E)dE = N_{cb}\frac{2}{\pi^{1/2}}\int_{E_{cb}}^{-\infty}\frac{\left(\frac{q}{k_B T}(E_{cb}-E)\right)^{1/2}}{1+e^{\frac{q}{k_B T}(E_F-E)}}dE = N_{cb}\frac{2}{\pi^{1/2}}F_{1/2}(E_F-E_{cb}) \qquad (4.10)$$

where N_{cb} is the effective density of states at the bottom of the conduction band, $F_{1/2}(E_F\text{-}E_{cb})$ is the Fermi-Dirac integral of ½ order with the potential difference between E_F and E_{cb} as the controlling

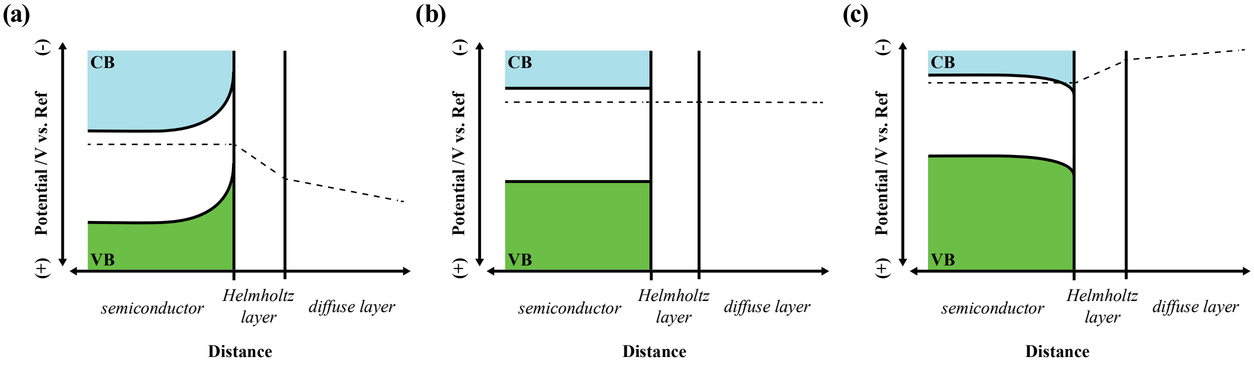

Figure 4.1. Potential distribution across the semiconductor space charge region, Helmholtz layer, and diffuse layer for (a) depletion, (b) flat-band, and (c) accumulation conditions. Distances are not drawn to scale.

variable. When $\frac{q}{k_BT}(E_{cb}-E_F)$ is << -3 (i.e. depletion), the Fermi-Dirac integral is well approximated by the Boltzmann function and the expression for n_s is simplified, i.e. $n_s = N_{cb}e^{\frac{q}{k_BT}(E_{cb}-E_F)}$.[43] When $\frac{q}{k_BT}(E_{cb}-E_F)$ is >-3, the Boltzmann approximation significantly overestimates $F_{1/2}(E_F-E_{cb})$. Instead, the explicit value of $F_{1/2}(E_F-E_{cb})$ must be evaluated and the full form of *eq. 4.10* must be used.

The Potential Dependence of n_s in the Presence of a Surface State

If a population of surface states exist within the semiconductor bandgap, the value of n_s is perturbed by the possibility of filling/removing carrier density from them. Specifically, the fraction, f, of monoenergetic surface states occupied by electrons is given by *eq. 4.11*,[44]

$$f = \frac{k_{ss}n_s}{k_{ss}n_s + k_{ss}^{-1}N_{cb}e^{\frac{q}{k_BT}(E_{cb}-E_{ss})}} \approx \frac{1}{1+\frac{N_{cb}e^{\frac{q}{k_BT}(E_{cb}-E_{ss})}}{n_s}} = \frac{1}{1+e^{\frac{q}{k_BT}(E_F-E_{ss})}} \qquad (4.11)$$

where k_{ss} and k_{ss}^{-1} are the rate constants (cm^{-3} s^{-1}) for filling/removing electrons from/to the conduction band to/from the surface states, respectively, and E_{ss} is the potential of the surface state. This expression assumes that the rates of charge transfer between surface states and redox species in solution are negligible. A further simplifying assumption is that k_{ss} and k_{ss}^{-1} are equivalent in magnitude if they only depend on the thermal velocity of electrons in Si (~10^7 cm s^{-1})[43, 45] and the area of the surface state is the size of a Si atom (10^{-15} cm^2).

The capacitance of a population of monoenergetic surface states, C_{ss}, arises from the potential dependence of *f*,[46]

$$C_{ss} = qN_{ss}\frac{df}{dE} \qquad (4.12)$$

where N_{ss} is the total density (cm^{-2}) of surface states. *Eq. 4.12* has a similar functional form as *eq. 4.9* since the physical nature of the capacitances are the same. That is, majority carriers from the bulk reach the surface and can either populate the majority carrier band at the band edge or the population of surface states.

The surface state capacitance contributes to the total capacitance as follows,[42, 47]

$$1 = \frac{C_{total}}{C_{sc}+C_{ss}} + \frac{C_{total}}{C_H} + \frac{C_{total}}{C_{dl}} \qquad (4.13)$$

since electrons that reach the interface from the bulk can either populate the conduction band or surface states. Accordingly, the potential drop across the space-charge region of the semiconductor and surface states are equal. Hence, *eq. 4.13* does not change the form or meaning of *eq. 4.5*.

The General Potential Dependence of k_{et}

In contrast to the *J-E* data for metal electrodes, the *J-E* responses for semiconductor electrodes cannot be accurately described by the Butler-Vomer formalism because charge-transfer can only occur through discrete states (i.e. at the band edges and/or through surface states) rather than across a continuum of states as in a metal.[31, 48-50] The Marcus-Gerischer model more accurately describes heterogeneous electron transfer from a discrete state (e.g. E_{cb}) to a dissolved, outer-sphere redox couple,[33, 49, 51]

$$k_{et} = k_{et,\max} e^{\frac{-\left(\left(E_{cb} - E^{0'}\right) + \lambda_{sc}\right)^2}{4\lambda_{sc} k_B T}} \qquad (4.14)$$

where $k_{et,max}$ is the rate constant for electron transfer at optimal exoergicity (~10^{17} cm^4 s^{-1}),[10, 31] k_B is Boltzmann's constant, T is temperature, and λ_{sc} is the reorganization energy for the redox process at the semiconductor/electrolyte interface. The value of k_{et} can be attenuated by a factor of $e^{-\beta l}$ if tunneling through a surface barrier layer (e.g. oxide) occurs, where β is a constant representing the material-dependent energy barrier for tunneling and l is the layer thickness. A common assertion for semiconductors is that k_{et} is independent of potential since all terms in *eq. 4.14* are constants. However, this point is not accurate in practice. When a fraction of the applied potential drops across the solution, the value of E_{cb} (from the perspective of a species in solution) varies. An alternate, equivalent statement is the band edge potentials become 'unpinned', altering the externally observable value of E_{cb}. Since the potential difference between E_{cb} and $E°$` is no longer fixed, k_{et} necessarily changes at every applied potential. To be clear, though, there is no justification *a priori* to assume this potential dependence can be described by a general analytical expression.[37] Instead the potential-dependence is system-specific based on the interplay of the relevant capacitance values. The salient feature of this potential dependence is that, while tedious to identify, it can be incorporated without changing the meaning of *eq. 4.14*.

4.3. Methods

Calculations

The approach used to generate working *J-E* curves for semiconductor electrodes can be summarized as follows. *Eqs. 4.5-4.9* and *4.11-4.13* were used to calculate iteratively the potential dropped within the semiconductor at any applied potential for a given semiconductor/electrolyte system. This information was then used to calculate both n_s and k_{et} at every applied potential using *eqs. 4.10* and *4.14*, which were then used in *eqs. 4.1-4.4* to predict *J-E* behaviors for SUMEs. For these calculations, the flat band potential, E_{fb}, was used as the reference point for calculations, since there is no space-charge capacitance at this potential. Accordingly, this specific potential value has the same physical meaning for charges both within the semiconductor and ions in the electrolyte. Relevant parameters used in the presented calculations are shown in Table 4.1.

The value of C_{sc} at any applied potential was determined using the following expression for F_s,[42]

$$F_s = (2)^{1/2}\left(\frac{4}{3}\pi^{-1/2}\frac{N_{cb}}{N_d}F_{3/2}\left(E_F - E_{cb}\right) - \frac{q(E_{fb} - E_F)}{k_B T} - 1\right)^{1/2} \qquad (4.15)$$

where $F_{3/2}(E_F\text{-}E_{cb})$ is the Fermi-Dirac integral of 3/2 order with the potential difference between E_F and E_{cb} as the controlling variable. Accordingly, the explicit expression for C_{sc} that is valid in both depletion and accumulation is,

$$C_{sc} = \sqrt{\frac{q^2\varepsilon\varepsilon_0 N_d}{2k_B T}}\left(\frac{2\pi^{-1/2}\frac{N_{cb}}{N_d}F_{1/2}\left(E_F - E_{cb}\right) - 1}{\left(\frac{4}{3}\pi^{-1/2}\frac{N_{cb}}{N_d}F_{3/2}\left(E_F - E_{cb}\right) - \frac{q(E_{fb} - E_F)}{k_B T} - 1\right)^{1/2}}\right) \qquad (4.16)$$

It is important to note that $3/2F_{1/2}(E_F\text{-}E_{cb})$ is explicitly the derivative of $F_{3/2}(E_F\text{-}E_{cb})$.[52]

The utility of *eq. 4.16* hinges on evaluating the integrals represented by $F_{1/2}(E_F\text{-}E_{cb})$ and $F_{3/2}(E_F\text{-}E_{cb})$. Unfortunately, they have no known analytical solutions.[53] Nevertheless, two strategies still allow the use of *eq. 4.16* for the purpose of this work. First, when $\frac{q(E_{cb}-E_F)}{k_B T}$ is << -3, $F_{3/2}(E_F\text{-}E_{cb})$ has a limiting value of $\frac{3}{4}\pi^{1/2}e^{\frac{q(E_{cb}-E_F)}{k_B T}}$ and $F_{1/2}(E_F\text{-}E_{cb})$ approaches $\frac{\pi^{1/2}}{2}e^{\frac{q(E_{cb}-E_F)}{k_B T}}$. In this case, the expression for C_{sc} simplifies to either form of *eq. 4.17*, depending on how negative the term ‘$E_{cb} - E_F$’ is.

$$C_{sc}=\sqrt{\frac{q^2\varepsilon\varepsilon_0 N_d}{2k_BT}}\left(\frac{e^{\frac{q\left(E_{fb}-E_F\right)}{k_BT}}-1}{\left(e^{\frac{q\left(E_{fb}-E_F\right)}{k_BT}}-\frac{q(E_{fb}-E_F)}{k_BT}-1\right)^{1/2}}\right) \quad (4.17a)$$

$$C_{sc}=\frac{-\sqrt{\frac{q^2\varepsilon\varepsilon_0 N_d}{2k_BT}}}{\left(-\frac{q(E_{fb}-E_F)}{k_BT}-1\right)^{1/2}} \quad (4.17b)$$

Eq. 4.17b is the well-known Mott-Schottky expression.[54] Second, when $\frac{q\left(E_{cb}-E_F\right)}{k_BT}$ is ≥ -3, the values of $F_{1/2}(E_F\text{-}E_{cb})$ and $F_{3/2}(E_F\text{-}E_{cb})$ can be approximated. Although tabulated numerical values[52, 55] and polynomial fits[53] for evaluating these functions are available in the literature, an approach based on Prony's method (i.e. fitting a function through a series of damped complex exponentials)[56] is most useful here.[57] In this tactic, a given approximating expression can be integrated/differentiated to give values for higher/lower order forms of the Fermi-Dirac integral.[58] That is, the values of the 1/2 and 3/2 Fermi-Dirac integrals can be referenced to each other for better accuracy than disconnected polynomial approximations.[58] Previous work has shown that four term exponential series are sufficient for precise estimation of Fermi-Dirac integral evaluation over a defined range of the controlling variable.[57] Accordingly, in this work, the following expressions were used to approximate these integrals,

$$F_{1/2}\left(E_F-E_{cb}\right)=\int_{E_{cb}}^{-\infty}\frac{\left(\frac{q}{k_BT}\left(E_{cb}-E\right)\right)^{1/2}}{1+e^{\frac{q}{k_BT}(E_F-E)}}dE\approx\sum_{i=1}^{4}X_ie^{a_i(E_F-E_{cb})};\text{when}\,\frac{q\left(E_{cb}-E_F\right)}{k_BT}>-3 \quad (4.18a)$$

$$F_{3/2}\left(E_F-E_{cb}\right)=\int F_{1/2}\left(E_F-E_{cb}\right)dE\approx\sum_{i=1}^{4}M_ie^{m_i(E_F-E_{cb})};\text{when}\,\frac{q\left(E_{cb}-E_F\right)}{k_BT}>-3 \quad (4.18b)$$

where X_i and M_i are the pre-exponential coefficients and a_i & m_i are the exponential term coefficients for the i^{th} terms in the 1/2 and 3/2 approximations, respectively. Table 4.2 summarizes the values of the coefficients used for specific ranges of '$E_F\text{-}E_{cb}$' values.

Table 4.1. Relevant parameters for working curve generation

Parameter	Variable	Value(s)	Units
SUME Radius	r	5	µm
Dopant Density	N_d	10^{15} or 10^{18}	cm^{-3}
Standard Potential	$E^{0'}$	0.4 - -0.4	V vs. E_{cb}
Conduction Band Edge	E_{cb}	-1	V (sets reference scale)
Reorganization Energy	λ	0.5 – 1.25	N/A
Rate constant at optimal exoergicity	$k_{et, max}$	6×10^{-17}	$cm^4 s^{-1}$
Surface state capacitance	C_{ss}	$10^{-8} - 5 \times 10^{-6}$	$F cm^{-2}$
Surface state density	N_{ss}	$10^{13} - 10^{18}$	cm^{-2}
Surface state energy	E_{ss}	0 – 0.3	V vs. E_{fb}
Surface layer thickness	l	0 – 0.6	nm
Tunneling Coefficient	β	0.1	nm^{-1}

Table 4.2. Coefficients for Fermi-Dirac integral approximations

$F_{1/2}$		$F_{3/2}$	
Coefficient	Value	Coefficient	Value
X_1	10.716	M_1	3700.6
X_2	-58.207	M_2	-4958.8
X_3	-2.6791	M_3	2633.2
X_3	50.847	M_4	-1373.9
a_1	-0.30	m_1	0.034
a_2	-0.01	$m2$	0.018
a_3	-0.51	$m3$	-0.062
$a4$	0.04	m_4	-0.093

Two approaches were explored to describe the capacitance of surface states. For the case of a single surface state, the derivative of the simplified form of *eq. 4.11* is shown in *eq. 4.19*,

$$C_{ss} = -qN_{ss}\frac{e^{\frac{q}{k_BT}(E_F - E_{ss})}}{\left(1+e^{\frac{q}{k_BT}(E_F - E_{ss})}\right)^2} \qquad (4.19)$$

This capacitance has a strong dependence on E_F, reaching a maximum when $E_F = E_{ss}$ and approaching zero when either $\left|E_F\right| >> \left|E_{ss}\right|$ or $\left|E_F\right| << \left|E_{ss}\right|$. The second approach to model surface state capacitance was to assume a continuum of surface states. In this case, the continuum effected a constant capacitance value that was independent of the applied potential, i.e. C_{ss} = constant.

Experimental

Experimental voltammetric data were acquired with a $r = 5$ µm n-Si SUME with a bulk carrier density of 1.6 x 10^{18} cm^{-3} (MTI Corp.). Fabrication details can be found in a previous report.[23] The electrolyte consisted of either vacuum-dried 2 mM cobaltocenium hexafluorophosphate (CoCp^+, 98%, Sigma-Aldrich) or benzyl viologen dichloride (BV^{2+}, 97%, Sigma-Aldrich) with 500 mM LiCl (>99%, Fisher) dissolved in anhydrous methanol (99.8% Sigma-Aldrich). Data were collected with a CHI420A (CH Instruments) potentiostat in a custom-built, dark Faraday cage housed in a N_2-filled glovebox. The SUME was held in a Teflon cell, sealed with a Viton o-ring, and contained separate Pt wire counter and reference electrodes. The voltammetry of ~10 mM ferrocene ($\text{Fc}^{0/+}$), spiked into solution, was used to calibrate the potential axis following each measurement.

4.4. Results

Influence of Dopant Concentration on SUME Voltammetry

Figure 4.2 highlights the dependences of the voltammetric responses of ideal n-type Si SUMEs (i.e. $N_{ss} = 0$, no surface barrier layer) with N_d, $E°`$, and $\lambda_{sc}$ in depletion ($E_{cb} - E°` = -0.3$ V) and accumulation ($E_{cb} - E°` = +0.3$ V) conditions. Figure 4.2a shows the corresponding steady-state responses predicted for SUMEs with increasing dopant density. Relative to E_{fb}, the voltammetric responses both in depletion and accumulation generally shift to more positive potentials as the dopant density is increased. The voltammetric shape (i.e. broadness) is also

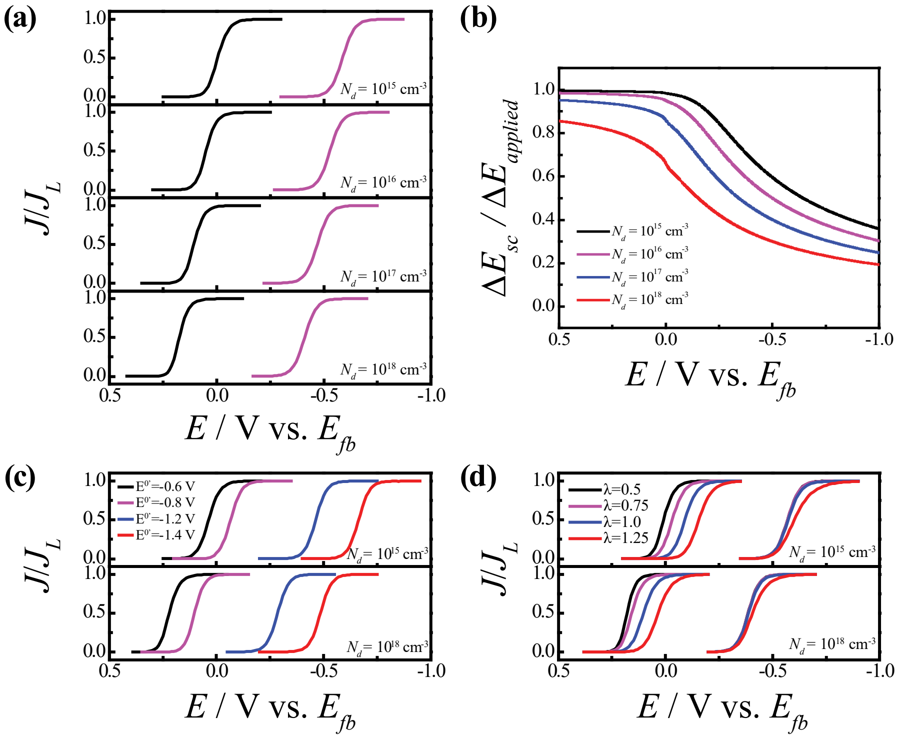

Figure 4.2. Modeled steady-state voltammetric responses and potential distributions of pristine low- and high-doped r = 5 μm n-Si SUMEs as a function dopant density (N_d), reorganization energy (λ_{sc}), and the standard potential of the redox species in solution ($E^{\circ`}$) under depletion and accumulation. (a) Variation in $N_d$ with $E_{cb}$ = -1.0 V, $E^{\circ`}$= -0.7 and -1.3 V, and λ_{sc} = 0.6. (b) Potential distribution for variation in N_d with the same parameters as in (b). (c) Variation in $E^{\circ`}$ for $E_{cb}$ = -1.0 V and $\lambda_{sc}$ = 0.6. (d) Variation in $\lambda_{sc}$ for $E^{\circ`}$ = -0.7 and -1.3 V and E_{cb} = -1.0 V.

slightly sensitive towards changes in dopant density, with a more pronounced effect in depletion. It should be noted that no changes on this magnitude will be observed in the voltammetric response as function of dopant density when plotted vs. an external, fixed reference potential. More importantly, these changes in the voltammetric behavior have nothing to do with 'non-ideal' surface conditions, but rather arise due to the nature of the distribution of the applied potential.

Figure 4.2b shows the corresponding fraction of the applied potential that is specifically dropped across the space-charge region under these same conditions. For lightly doped substrates, all the potential is dropped across the space-charge region when E_F is more positive of the flat-band potential. For heavily doped SUMEs, this fraction decreases to ~0.6 of the total applied potential when E_F is slightly more positive than the flat-band potential. For applied potentials more negative than E_{fb}, the fraction of the applied potential dropped in the semiconductor substantially decreases. The fall off is progressively more pronounced for SUMEs with higher dopant concentrations.

Influence of the Formal Potential of an Outer-Sphere Redox Couple on SUME Voltammetry

Figure 4.2c details the influence of $E°`$ of the redox species relative to $E_{fb}$. For the depletion case, the position of the steady-state current-potential response only depends on $E°`$ as it approaches E_{fb}. That is, the position of the voltammetric response in depletion depends on the operative value of k_{et}.[23] For the accumulation case, the position of the voltammetric response *does* track with $E°`$, with the sigmoidal response occurring right near $E°`$.

Influence of Reorganization Energy on SUME Voltammetry

Figure 4.2a presents the influence of λ_{sc}. The voltammetric response noticeably broadens and shifts to more negative potentials at larger reorganization energies. Generally, the broadening in depletion is substantial for both low and high dopant densities and the influence of λ_{sc} is more pronounced than the broadening from changes in dopant density. In accumulation, the voltammetric response is also broadened, but the effect is less pronounced over the same range of λ_{sc} values and at higher dopant densities.

Influence of a Surface States on SUME Voltammetry

Figure 4.3 describes the voltammetric responses of 'non-ideal' n-type SUMEs. In this case, the electrode interface is covered by a 0.2 nm tunneling barrier (e.g. a native oxide) with a uniform, potential-independent capacitance, C_{ss}. Figure 4.3a shows the impact of changing C_{ss} on the

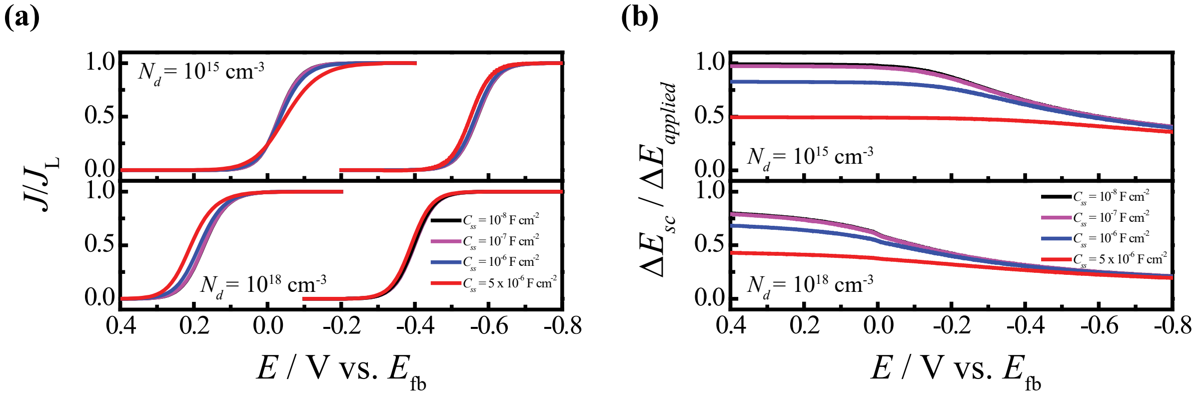

Figure 4.3. Modeled (a) steady-state voltammetric response and (b) applied potential distribution of low- and high-doped $r = 5$ µm n-Si SUMEs including a surface layer with a potential-independent capacitance, C_{ss}. For both plots, C_{ss} is varied with $E_{cb} = -1.0$ V, $E^{\circ`} = -0.7$ and -1.3 V, and $\lambda_{sc} = 0.6$. The layer thickness, l, and the tunneling coefficient, β, were set at 0.2 nm and 0.1 nm^{-1}, respectively.

voltammetry. For low-doped SUMEs under depletion conditions, the voltammetric response occurs over a progressively larger potential range as C_{ss} is increased. At low dopant concentrations and the largest C_{ss} value (= 5 x 10^{-6} F cm^{-2}), the foot and plateau of the sigmoid are separated by ~300 mV. At high dopant concentrations, this separation shrinks to ~200 mV. Under accumulation conditions, the broadening of the voltammetric response is still observable but much more subtle. The fraction of the applied potential dropped across the space-charge region are shown in Figure 4.3b. For low-doped SUMEs operating under depletion, this plot is essentially the same as the data in Figure 4.2b when $C_{ss} < 10^{-7}$ F cm^{-2}. For larger C_{ss} values, the fraction of the applied potential when E_F is more positive than E_{fb} drops precipitously. A similar trend occurs for high-doped SUMEs.

The same analysis was performed for SUME surfaces with a monoenergetic population of surface states centered at $E = +0.1$ V vs E_{fb}. These data are shown in Figures 4.4a and 4.4b. Here, $N_{ss} = 10^{15}$ cm^{-2} was considered the maximum possible density since this value corresponds to every surface atom being a surface state. Figure 4.4a describes the dependence of the voltammetric response of low- and high-doped SUMEs with the density of surface states. For any dopant concentration, no obvious change is observed when $N_{ss} < 10^{13}$ cm^{-2}. In depletion, the voltammetry is highly sensitive to $N_{ss} > 10^{13}$ cm^{-2} . Increasing the surface-state density impacts the voltammetry in two ways. First, the rise of the current is less sharp, resulting in a much broader current profile. Second, the curve position shifts to more positive potentials. Under these conditions, the changes are obvious at large doping levels but nondescript at small doping levels.

Figure 4.4b shows the corresponding potential distributions for low- and high-doped SUMEs. When $N_{ss} \geq 10^{13}$ cm^{-2}, the fraction of the applied potential decreases specifically only at potentials where the capacitance of the surface states was appreciable. At other applied potentials, there is no change relative to what is shown in Figure 4.2b.

Figure 4.5a and 4.5c highlight the effect of the value of E_{ss} on the form of the voltammetry for $N_{ss} = 10^{14}$ cm^{-2} and 10^{15} cm^{-2}. For the low dopant concentration and lower surface state density under depletion, a slight increase in current near the foot of the response was observed as the trap state energy approached E_{fb}. For the higher doped SUME under depletion, a slight shift in the curve position was observed. No noticeable change was observed for charge transfer under accumulation. For higher surface state densities, severe broadening of the voltammetry was

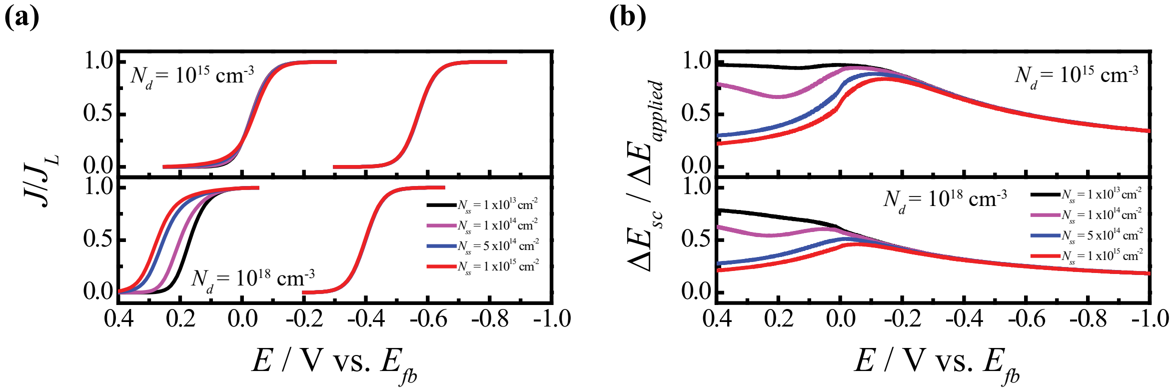

Figure 4.4. Modeled (a) steady-state voltammetric response and (b) applied potential distribution of low- and high-doped $r = 5$ µm n-Si SUMEs considering trap states with a defined density, N_{ss}. For both plots, N_{ss} is varied with $E_{cb} = -1.0$ V, $E^{\circ`} = -0.7$ and -1.3 V, $\lambda_{sc} = 0.6$, $l = 0.2$ nm, and $\beta = 0.1$ nm^{-1}. The trap state energy, E_{ss}, is located at 0.1 V for $N_d = 10^{15}$ cm^{-3} and 0.2 V for $N_d = 10^{15}$ cm^{-3}.

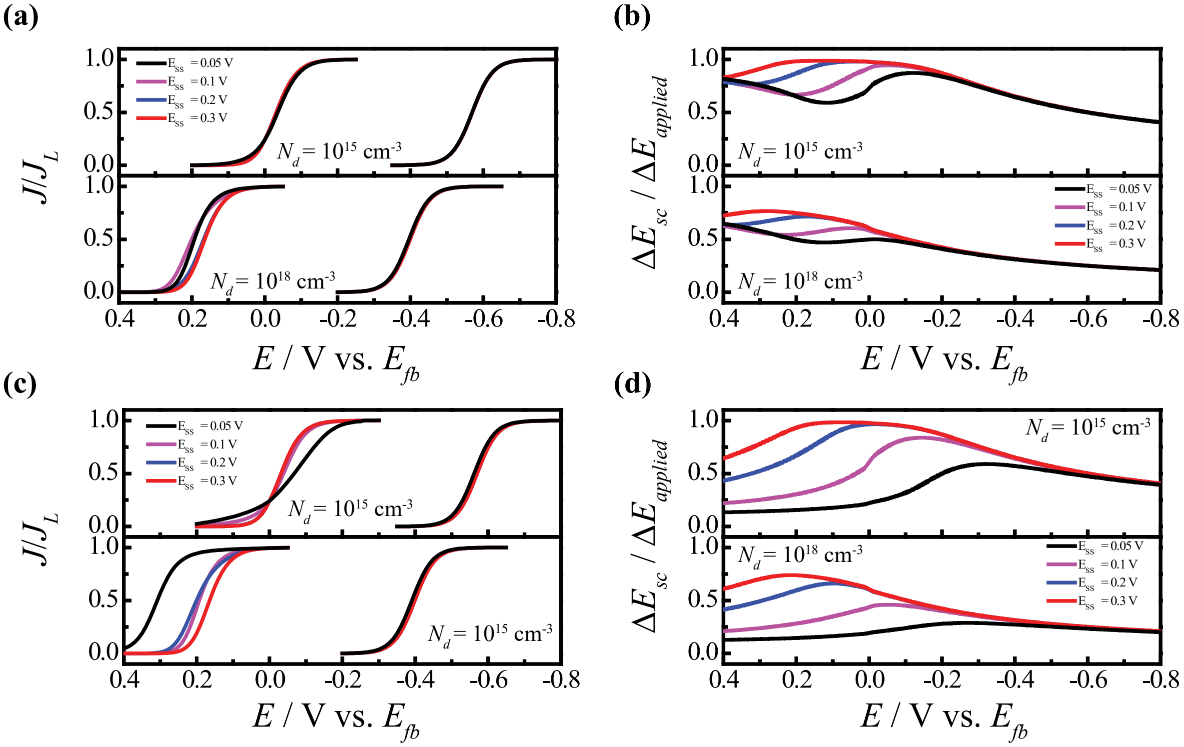

Figure 4.5. Modeled (a,c) steady-state voltammetric responses and (b,d) applied potential distributions of low- and high-doped $r = 5$ μm n-Si SUMEs with varying E_{ss}. For (a) and (b) $N_{ss} = 10^{14}$ cm^{-2}, $E_{cb} = -1.0$ V, $E^{\circ`} = -0.7$ and $-1.3$ V, $\lambda_{sc} = 0.6$, $l = 0.2$ nm, and $\beta = 0.1$ nm$^{-1}$. For (c) and (d) $N_{ss} = 10^{15}$ cm$^{-2}$, $E_{cb} = -1.0$ V, $E^{\circ`} = -0.7$ and -1.3 V, $\lambda_{sc} = 0.6$, $l = 0.2$ nm, and $\beta = 0.1$ nm^{-1}.

noticeable for low-doped electrodes when the trap state was within 50 mV of E_{fb} in depletion. Again, no change was evident for the voltammetry for the redox species in accumulation. For heavily doped SUMEs, the voltammetric changes in depletion are significantly different. When the trap state potential is closer to E_{fb}, the curve shifts to more positive potentials and became broadened. However, the shift and change in broadness do not monotonically follow changes in E_{ss}. That is, broader curves and more positive onset potentials correspond to E_{ss} = 0.2 and 0.05 V vs. E_{fb}, but a sharper and more negative curve is predicted for E_{ss} = 0.1 V vs. E_{fb}.

The form of the fractional potential drop as a function of applied potential depended strongly on E_{ss} and N_{ss} (Figure 4.5b and 4.5d). As the surface trap is moved closer to E_{fb}, a broad decrease in the fraction of applied potential dropped across the space-charge region in the potential range around E_{ss}. This decrease was more pronounced for lower dopant concentrations and high trap state densities.

Influence of Tunneling Through a Surface Barrier on SUME Voltammetry

The effect of current attenuation by tunneling of majority carriers through a surface barrier layer was also considered (Figure 4.6) for lightly and highly doped n-type SUMEs as a function of surface layer thickness, *l*. In this treatment, the effect is the same as a diminution in $k_{et,\mathrm{max}}$. For lightly doped SUMEs, the voltammetric response is affected both in depletion and accumulation but not equivalently. As tunneling diminishes the current in depletion, the curves shift towards more negative potentials. The wave shape also changes, with the sigmoidal response exhibiting a rounder profile at potentials near the plateau current. For more heavily doped SUMEs under depletion, the rounding and broadening of the voltammetric response shape is more pronounced. Under accumulation, the rounding and overall voltammetric shape is identical for low and high doping concentrations.

Fitting of Experimental Data

The experimental voltammetric responses for a 5 µm n-Si SUME in contact with methanolic, 2 mM solutions of BV^{2+} and $CoCp^{+}$ are shown in Figure 4.7a and 4.7b, respectively. The capacitance apparent in the data is an artifact of the design of these n-Si SUMEs but otherwise not germane to the analysis. Using the method outlined above, good fits were obtained for both redox couples (fitting results provided in figure caption). For the $BV^{2/1+}$ and $BV^{1+/0}$ couples ($E°`$ = -0.8 and -1.25 V vs. $E(Fc^{0/+})$, respectively), consideration of N_{ss} and E_{ss} parameters was required

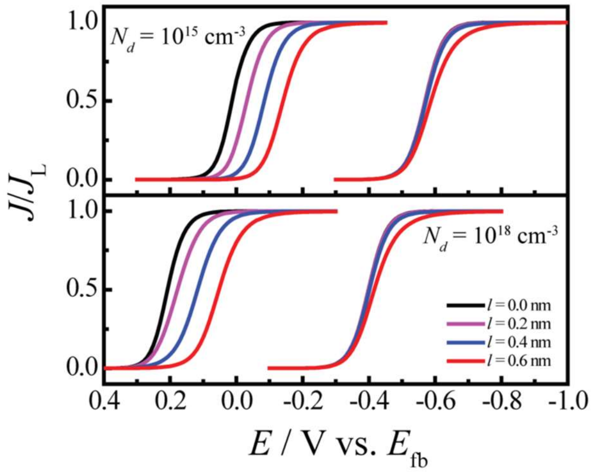

Figure 4.6. Modeled steady-state voltammetric responses of low- and high-doped r = 5 µm n-Si SUMEs with varying l. For both dopant densities, $N_{ss} = 5 \times 10^{14}$ cm^{-2}, E_{cb} = -1.0 V, $E^{\circ`}$ = -0.7 and -1.3 V, λ_{sc} = 0.6, E_{SS} = 0.2 V and β = 0.1 nm^{-1}.

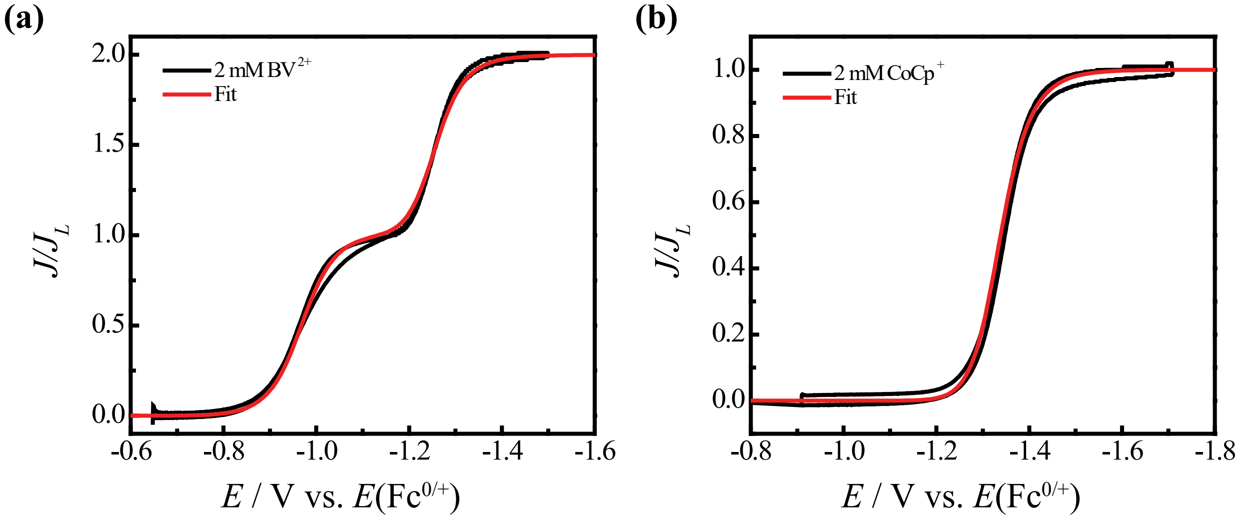

Figure 4.7. Voltammetric responses of high-doped, r = 5 µm n-Si SUMEs to (a) 2 mM BV^{2+} and (b) 2 mM CoCp$^+$ with corresponding fits. Fitted parameters are: (a) N_d = 1.6 x 10^{18} cm^{-3}, N_{ss} = 5 x 10^{14} cm^{-2}, E_{cb} = -1.21 V vs. E(Fc$^{0/+}$), $E°$` = -0.8 and -1.25 V vs. $E$(Fc$^{0/+}$), $\lambda_{sc}$ = 0.65 and 0.68, $E_{SS}$ = 0.019 V vs. $E_{fb}$, $l$ = 0.4 nm and $\beta$ = 0.1 nm$^{-1}$. (b) $N_d$ = 1.6 x 10$^{18}$ cm$^{-3}$, $E_{cb}$ = -1.12 V vs. $E$(Fc$^{0/+}$), $E°$` = -1.33 V vs. vs. E(Fc$^{0/+}$), and λ_{sc} = 1.1.

for accurate fitting resulting in a universal fit to E_{cb} (at $E_F = E_{fb}$) = -1.21 vs. $E(\mathrm{Fc}^{0/+})$. Conversely, operating under accumulation for the voltammetry of CoCp ($E°$` = -1.33 V vs. $E(\mathrm{Fc}^{0/+})$) and an apparent clean interface did not require surface traps to be considered for the fitting. The resulting band edge (at $E_F = E_{fb}$) was determined to be E_{cb} = -1.12 vs. $E(\mathrm{Fc}^{0/+})$.

4.5. Discussion

The presented work supports the following contentions. First, interpretation of the shape of steady-state *J-E* responses for SUMEs is significantly more nuanced than for conventional metal ultramicroelectrodes but the data is still tractable and informative. Second, the steady-state *J-E* responses for simple, 1e^- outer-sphere redox couples depends strongly on whether the semiconductor electrode is in depletion vs accumulation conditions. Analyzing both types of *J-E* responses in conjunction can provide qualitative and quantitative information on the semiconductor/electrolyte interface. Third, the framework presented here could be further refined to enrich the interpretation of SUME data. These points are elaborated below.

Factors that Influence the Shape of the J-E Response

The common practice in analyzing the *J-E* behavior of metal ultramicroelectrodes is to adopt the Butler-Volmer formalism for k_f & k_b and to fit the data using $E°$`, k_{et} (the standard rate constant, cm s^{-1}), and α_{et} (the transfer coefficient) as fitting parameters without consideration of any other physicochemical properties of the system.[26, 59] The global take-away from the working curves presented here is that a comprehensive analysis of data from SUMEs requires consideration of many factors. Importantly, all the terms in Table 4.1 required for fitting are common electrochemical properties that are either physically measurable and/or can be experimentally varied. Hence, despite the apparent complexity, the framework presented here is clear that arbitrary correction/'non-ideality' factors with no direct physical origin are not necessary to interpret or discuss raw SUME electrochemical data.

Because of the nuanced interplay of physicochemical and electrochemical factors in the *J-E* responses of SUMEs, simplified electroanalytical approaches like evaluating the Tomes criterion (i.e. analyzing the potential difference between the points where the current is ¾ and ¼ the steady-state plateau value)[41] or the method of Mirkin and Bard[60] are not useful or recommended. Similarly, a point-by-point evaluation of raw *J-E* data[41] from a SUME is not practical since the connection between the solution potential and the potential drop within the semiconductor must first be deconvoluted. Rather, interpreting SUME data requires curve fitting by specifying k_f and k_b using the constraints and expressions presented here. Although cumbersome, the working curves shown here are clear on the following point. Specifically, the interdependencies of complex functions like $F_{1/2}(E_F\text{-}E_{cb})$, $F_{3/2}(E_F\text{-}E_{cb})$, C_{ss}, and C_{sc} make it difficult to fit a SUME response with any arbitrary set of parameters if the purpose is to identify properties of interest. When common experimental conditions are properly specified (e.g. dielectric properties of the solvent, concentration of the electrolyte, $E°$` for the redox couple of interest), the form of the *J-E* responses can be assessed to understand λ_{sc}, E_{cb} (at the flat band condition), and the possible contribution of surface states & surface tunneling barriers. Non-linear least-squares fitting will be useful if the uncertainty in these parameters are weighted a priori (e.g. estimation of λ_{sc} through separate measurable quantities)[61-62] and bound by reasonable intuition (e.g. $N_{ss} \leq 10^{15}$ cm^{-2} since surface state density cannot be larger than surface atom density).

Comparison of J-E Responses in Depletion and Accumulation

A second global take-away from the presented curves is that the shapes of the *J-E* responses are much more sensitive to surface conditions in depletion than in accumulation. Simply, the *J-E* responses in accumulation generally occur at or very close to $E°$` when the reorganization energy for the redox process is small. This feature is similar to the responses of metal ultramicroelectrodes but noticeably different than SUME responses in depletion, where the *J-E* responses appear near $E_{cb}$ but do not directly relate to $E°$`.[23]

The similarity of SUMEs in accumulation to metal electrodes operationally occurs for two reasons. In accumulation, n_s is large ($\sim N_{cb}$) and does not increase substantially as E_F is made more negative because of the functional form of $F_{1/2}(E_F - E_{cb})$. Additionally, the majority of applied potential drops across the solution rather than within the semiconductor in accumulation, further limiting the change in n_s. As a result, the value of E_{cb} when $E_F = E_{fb}$ is not the most influential aspect that sets the voltammetric responses of SUMEs in accumulation. Nevertheless, the current still increases at more negative applied potentials in accumulation because k_{et} increases. The potential dependence in k_{et} occurs since E_{cb} is unpinned and shifts to more negative potentials. Notably, the unpinning of the band edges is not a problem to be avoided, as has been commonly and repeated asserted in the semiconductor electrochemical literature.[12-14, 63-66] Rather, it is a feature of redox responses in accumulation and can be diagnostic of the semiconductor/electrolyte interface. For example, this particular effect is the reason why redox couples with large reorganization energies but $E°`$ more positive than $E_{cb}$ yield $J$-$E$ responses with a different shape than redox couples with small reorganization and similar $E°`$ values.[23]

Diagnostically, the presented results illustrate two further useful aspects of experimentally collected steady-state J-E data from SUMEs. First, when an n-type SUME voltammetric response occurs at $E°`$, the semiconductor must be in accumulation. Careful analysis of SUMEs with different dopant concentrations can even be used to gauge the extent of accumulation. Accordingly, these data can be used to estimate the band edges either qualitatively through the general trends shown above or precisely through simultaneous fitting of multiple voltammograms. The use of several redox couples with different $E°`$ values (and small, known reorganization energies) provides an increasingly more precise indication of E_{cb}. Second, the shape of the J-E response in accumulation near the steady-state current plateau is informative on k_{et}. The less 'square' the J-E response is, the more the data implicate a diminution of k_{et}. The origin of this decrease can be discerned between a large reorganization energy and a tunneling barrier at the surface through careful fitting of the data.

Conversely, when the voltammetric response occurs at potentials appreciably more negative than $E°`$, SUMEs are likely in depletion at those potentials. In this case, the broadness of the sigmoidal response is not a consequence of the value of k_{et}. Rather, the broadness indicates the applied potential is being dropped somewhere else besides the space charge region of the semiconductor and the solution. The presented analysis indicates that when the potential drops across a population of monoenergetic surface states, the shape of the J-E response is perturbed in specific manners that relate to the potential and density of states. Notably, when the capacitance of such surface states has a maximum for values of E_{ss} far from E_{cb}, the presence of surface states exerts no influence on the shape of the J-E response. Only when the surface state capacitance occurs closer to the conduction band edge where large currents flow (as controlled by n_s and k_{et}) does the presence of a single population of surface states become significant. Further, this work makes clear that a continuum of surface states across the band gap only appreciably matters when the effective surface capacitance is $>10^{-7}$ F cm^{-2}. Interestingly, the 'distortions' in the voltammetry caused by a population of monoenergetic surface states vs. a continuum of surface states is distinct enough that the two cases can be distinguished. Accordingly, in principle it should be possible to identify the presence of discrete surface states and estimate their potential relative to E_{cb} when $E_F = E_{fb}$.

Limitations of the Analysis

There are four limitations in the presented framework that merit future consideration. First, the solution capacitance is not universally independent of potential. In addition to the cosh term in the Gouy-Chapman description of the diffuse layer, the form of the Helmholtz capacitance could change at extreme applied potentials.[41] A previous report argued that even at large negative applied potentials that pushes an n-type semiconductor into accumulation, the corresponding Frumkin effects are minimal.[39] The analysis presented here is in accordance with that, where the 'cosh' term, at most, represented a factor of ~5 at the most negative potentials.

Similarly, specific adsorption on the semiconductor electrode was not considered. The effect of non-specific adsorption on interpreting charge-transfer kinetics at metal electrodes is well documented.[67] There are fewer illustrative instances in the semiconductor electrochemical literature. However, two notable examples, including pyridinium/alkali cation adsorption on TiO_2 sensitized photoanodes[68] and capping ligands on II-VI quantum dots,[69] suggest this topic is worth further future development.

Second, the presented analysis assumes that all rate-limiting factors involve charge transfer processes. That is, the transport of charge-carriers in the bulk of the semiconductor is presumed to be sufficiently fast so as not to be limiting on the current. This assumption is reasonable for SUMEs prepared from single-crystalline semiconductor substrates, where charge-carrier mobilities can be large. For amorphous, polycrystalline, or low purity/grade semiconductor crystal substrates, it is possible that transport through the space-charge region in the semiconductor electrode is limiting. This condition is operative when the following inequality holds,[38]

$$\frac{\sqrt{2}L_D}{D_n} Daw\left(\sqrt{-\frac{q}{k_B T}\left(E_{cb}-E_F\right)}\right) >> \frac{1}{k_{et}[A]} \qquad (4.20)$$

where D_n is the diffusion constant for electrons in an n-type semiconductor and *Daw* is the Dawson integral for the term in parentheses. Although an analytical model has been previously proposed for predicting current flow for semiconductor electrodes with low charge-carrier mobilities,[70] a more common approach to assess such semiconductor electrodes is through finite-difference modeling.[71-74] Although outside the scope of this work, such models could prove useful for studying SUMEs composed of materials such as single-crystalline and polycrystalline metal oxide films and amorphous Si. In the same vein, the study of SUMEs where the doping concentration is not uniform in the semiconductor would again be best served with some sort of finite-difference modeling, with the presented framework as the boundary conditions of models that otherwise describe carrier drift & diffusion in the semiconductor bulk.

Third, the presented analysis considers charge transfer involving only majority carriers (electrons) through the conduction band edge. For n-type semiconductors with moderate to large band gaps, the prevailing data from n-type SUMEs are consistent with this premise since appreciable currents occur only at potentials near the conduction band edge.[23-24] Further, so long as the redox species does not have significant energetic overlap with the valence band, consideration of charge-transfer into/from just the conduction band edge is appropriate. However, the possibility of charge transfer into/from solution from/into surface states is more relevant but not explicitly considered here. Specifically, such charge transfer would alter both the expressions for k_f, k_b, and the potential-dependence of C_{ss}. Although the revisions to k_f and k_b are straightforward,[74] the change in potential-dependence of C_{ss} is less clear. Qualitatively, the effect of rapid charge transfer between the electrolyte and surface states will shift the potential at which C_{ss} is maximal.[71] Quantitative descriptions of this effect in terms of Marcus-Gerischer formalisms requires further development since the forward and reverse rate constants would also have a complex potential dependence. This scenario is of interest and will be the focus of a future work. However, at this stage, the primary point is inclusion of this fact would not necessarily alter the principal conclusions about the shapes of the J-E responses of SUMEs but might complicate interpretation of E_{ss} if that is inferred from data.

Fourth, the capacitance expressions used here do not directly accommodate size effects. Accordingly, the trends discussed in this work most naturally apply to SUMEs with radii on the micron scale, where the double layer in solution and the semiconductor space charge region are much smaller than the electrode. When the SUME radius is comparable in size or smaller than the width of the depletion layer, the potential drop within the semiconductor should change even if all other aspects are the same.[75] When the SUME radius is $\leq 10^{-8}$ m, i.e. on the order of the Helmholtz layer, the expressions for the Helmholtz capacitance and reorganization energy are likely different.[76-77] Accordingly, further development is needed to predict fully the J-E responses of extremely small, nanoscale SUMEs. Nevertheless, the basic methodology outlined here of first calculating the potential drop in the semiconductor and then determining n_s & k_{et} should still apply.

4.6. Conclusions

The presented work illustrates the premise that the steady-state *J-E* curves of semiconductor ultramicroelectrodes in the absence of illumination can be understood under any operating condition using a combination of the Marcus-Gerischer formalism for charge-transfer kinetics and full accounting of the electrostatics of the semiconductor/electrolyte interface. Using a curve fitting approach, the nuanced experimental data can be deconvoluted to assess pertinent aspects of the interface including charge-transfer rate constants, electrolyte composition, and surface condition without arbitrary, non-physical 'non-ideality' factors. The framework shown here suggests that voltammetric experiments performed where only a single parameter is varied (e.g. change in doping density, redox couples with multiple redox states that span a large potential range) can provide similar insight to methods such as electrochemical impedance, particularly with respect to the energetics of the band edges. The presented working curves motivate further collection and analysis of such experimental data. A detailed example of such studies is forthcoming.

4.7. References

1. Deutsch, T. G.; Koval, C. A.; Turner, J. A. *J. Phys. Chem. B* **2006,** *110*, 25297.

2. Gronet, C. M.; Lewis, N. S.; Cogan, G.; Gibbons, J. *Proc. Natl. Acad. Sci. U.S.A.* **1983,** *80*, 1152.

3. Gratzel, M. *Nature* **2001,** *414*, 338.

4. Goodey, A. P.; Eichfeld, S. M.; Lew, K. K.; Redwing, J. M.; Mallouk, T. E. *J. Am. Chem. Soc.* **2007,** *129*, 12344.

5. Groner, M. D.; Koval, C. A. *J. Electroanal. Chem.* **2001,** *498*, 201.

6. Howard, J. N.; Koval, C. A. *Anal. Chem.* **1994,** *66*, 4525.

7. Hamann, T. W.; Gstrein, F.; Brunschwig, B. S.; Lewis, N. S. *J. Am. Chem. Soc.* **2005,** *127*, 13949.

8. Hamann, T. W.; Gstrein, F.; Brunschwig, B. S.; Lewis, N. S. *J. Am. Chem. Soc.* **2005,** *127*, 7815.

9. Hamann, T. W.; Gstrein, F.; Brunschwig, B. S.; Lewis, N. S. *Chem. Phys.* **2006,** *326*, 15.

10. Pomykal, K. E.; Fajardo, A. M.; Lewis, N. S. *J. Phys. Chem.* **1996,** *100*, 3652.

11. Chazalviel, J. N. *J. Electrochem. Soc.* **1982,** *129*, 963.

12. Nagasubramanian, G.; Wheeler, B. L.; Bard, A. J. *J. Electrochem. Soc.* **1983,** *130*, 1680.

13. Nagasubramanian, G.; Wheeler, B. L.; Fan, F. R. F.; Bard, A. J. *J. Electrochem. Soc.* **1982,** *129*, 1742.

14. Horowitz, G.; Allongue, P.; Cachet, H. *J. Electrochem. Soc.* **1984,** *131*, 2563.

15. Tomita, E.; Matsuda, N.; Itaya, K. *J. Vac. Sci. Technol. A* **1990,** *8*, 534.

16. Itaya, K.; Tomita, E. *Surf. Sci.* **1989,** *219*, 515.

17. Streckert, H. H.; Ellis, A. B. *J. Phys. Chem.* **1982,** *86*, 4921.

18. Nakato, Y.; Tsumura, A.; Tsubomura, H. *Chem. Phys. Lett.* **1982,** *85*, 387.

19. Beckmann, K. H.; Memming, R. *J. Electrochem. Soc.* **1969,** *116*, 368.

20. Lewerenz, H. J.; Aspnes, D. E.; Miller, B.; Malm, D. L.; Heller, A. *J. Am. Chem. Soc.* **1982,** *104*, 3325.

21. Lichterman, M. F.; Hu, S.; Richter, M. H.; Crumlin, E. J.; Axnanda, S.; Favaro, M.; Drisdell, W.; Hussain, Z.; Mayer, T.; Brunschwig, B. S.; Lewis, N. S.; Liu, Z.; Lewerenz, H. J. *Energ. Environ. Sci.* **2015,** *8*, 2409.

22. Tufts, B. J.; Kumar, A.; Bansal, A.; Lewis, N. S. *J. Phys. Chem.* **1992,** *96*, 4581.

23. Acharya, S.; Lancaster, M.; Maldonado, S. *Anal. Chem.* **2018,** *90*, 12261.

24. Rodman, S.; Spitler, M. T *J. Phys. Chem. B* **2000,** *104*, 9438.

25. Bond, A. M.; Oldham, K. B.; Zoski, C. G. *J. Electroanal. Chem.* **1988,** *245*, 71.

26. Sun, Y. Y. T.; Mirkin, M. V. *Anal. Chem.* **2016,** *88*, 11758.

27. Wightman, R. M. *Anal. Chem.* **1981,** *53*, 1125.

28. Fajardo, A. M.; Lewis, N. S. *J. Phys. Chem. B* **1997,** *101*, 11136.

29. Farjardo, A. M.; Lewis, N. S. *Science* **1996,** *274*, 969.

30. Lewis, N. S. *Sol Energy Mater. Sol Cells* **1995,** *38*, 323.

31. Lewis, N. S. *J. Phys. Chem. B* **1998,** *102*, 4843.

32. Royea, W. J.; Fajardo, A. M.; Lewis, N. S. *J. Phys. Chem. B* **1997,** *101*, 11152.

33. Gao, Y. Q.; Georgievskii, Y.; Marcus, R. A. *J. Chem. Phys.* **2000,** *112*, 3358.

34. Gao, Y. Q.; Marcus, R. A. *J. Chem. Phys.* **2000,** *113*, 6351.

35. Chekir, F.; Lu, G. N.; Barret, C. *Solid-State Electronics* **1986,** *29*, 519.

36. Tung, R. T. *Appl. Phys. Rev.*. **2014,** *1*, 011304.

37. Natarajan, A.; Oskam, G.; Searson, P. C. *J. Phys. Chem. B* **1998,** *102*, 7793.

38. Hamnett, A., Chapter 2 Semiconductor Electrochemistry. In *Comprehensive Chemical Kinetics*, Compton, R. G., Ed. Elsevier: 1988; Vol. 27, pp 61.

39. Royea, W. J.; Kruger, O.; Lewis, N. S. *J. Electroanal. Chem.* **1997,** *438*, 191.

40. Allongue, P.; Cachet, H. *Solid State Commun.* **1985,** *55*, 49.

41. Bard, A. J.; Faulkner, L. R., *Electrochemical Methods: Fundamentals and Applications*. 2nd ed.; John Wiley & Sons, Inc.: Hoboken, NJ, 2001.

42. Many, A.; Goldstein, Y.; Grover, N. B., *Semiconductor Surfaces*. John Wiley & Sons: Amsterdam, 1965.

43. Sze, S. M.; Ng, K. K., *Physics of Semiconductor Devices*. 3rd ed.; John Wiley & Sons: Hoboken, NJ, 2007.

44. Hoffmann, P. M.; Searson, P. C. *J. Appl. Phys.* **1998,** *83*, 4309.

45. Yablonovitch, E.; Allara, D. L.; Chang, C. C.; Gmitter, T.; Bright, T. B. *Phys. Rev. Lett.* **1986,** *57*, 249.

46. Allongue, P.; Cachet, H. *J. Electrochem. Soc.* **1985,** *132*, 45.

47. Morrison, S. R., *Electrochemistry at semiconductor and oxidized metal electrodes* Plenum Press: New York, NY, 1980.

48. Gerischer, H., Semiconductor electrochemistry. **1968**.

49. Gerischer, H. *Surf. Sci.* **1969,** *13*, 265.

50.Gerischer, H. *J. Phys. Chem.* **1991,** *95*, 1356.

51. Gerischer, H. *Surf. Sci.* **1969,** *18*, 97.

52. McDougall, J.; Stoner, E. C. *Philos. Trans. Royal Soc.* **1938,** *237*, 67.

53. Van Halen, P.; Pulfrey, D. L. *J. Appl. Phys.* **1985,** *57*, 5271.

54. Degryse, R.; Gomes, W. P.; Cardon, F.; Vennik, J. *J. Electrochem. Soc.* **1975,** *122*, 711.

55. Blakemore, J. S. *Solid-State Electronics* **1982,** *25*, 1067.

56. Selvakumar, C. R. *Proc. IEEE* **1982,** *70*, 514.

57. AlQurashi, A.; Selvakumar, C. R. *Superlattices and Microstructures* **2018,** *118*, 308.

58. Aymerich-Humet, X.; Serra-Mestres, F.; Millán, J. *J. Appl. Phys.* **1983,** *54*, 2850.

59. Li, Y. X.; Bergman, D.; Zhang, B. *Anal. Chem.* **2009,** *81*, 5496-5502.

60. Mirkin, M. V.; Bard, A. J. *Anal. Chem.* **1992,** *64*, 2293.

61. Smith, B. B.; Koval, C. A. *J. Electroanal. Chem. Interfacial Electrochem.* **1990,** *277*, 43.

62. Marcus, R. A. *J. Phys. Chem.* **1990,** *94*, 1050.

63. Bard, A. J.; Bocarsly, A. B.; Fan, F. R. F.; Walton, E. G.; Wrighton, M. S. *J. Am. Chem. Soc.* **1980,** *102*, 3671.

64. Bocarsly, A. B.; Bookbinder, D. C.; Dominey, R. N.; Lewis, N. S.; Wrighton, M. S. *J. Am. Chem. Soc.* **1980,** *102*, 3683.

65. Dominey, R. N.; Lewis, N. S.; Wrighton, M. S. *J. Am. Chem. Soc.* **1981,** *103*, 1261.

66. Allongue, P.; Blonkowski, S.; Souteyrand, E. *Electrochim. Acta* **1992,** *37*, 781.

67. Fawcett, W. R. *J. Solid State Electrochem.* **2011,** *15*, 1347.

68. Wang, H.; Peter, L. M. *J. Phys. Chem. C* **2012,** *116*, 10468.

69. Hines, D. A.; Kamat, P. V. *J. Phys. Chem. C* **2013,** *117*, 14418.

70. Ullman, D. L. *J. Electrochem. Soc.* **1981,** *128*, 1269.

71. Iqbal, A.; Hossain, M. S.; Bevan, K. H. *Phys. Chem. Chem. Phys.* **2016,** *18*, 29466.

72. Iqbal, A.; Bevan, K. H. *MRS Commun.* **2018,** *8*, 466.

73. Chitambar, M.; Wang, Z.; Liu, Y.; Rockett, A.; Maldonado, S. *J. Am. Chem. Soc.* **2012,** *134*, 10670.

74. Anz, S. J.; Lewis, N. S. *J. Phys. Chem. B* **1999,** *103*, 3908.

75. Smit, G. D. J.; Rogge, S.; Klapwijk, T. M. *Appl. Phys. Lett.* **2002,** *81*, 3852.

76. Wang, H.; Pilon, L. *J. Phys. Chem. C* **2011,** *115*, 16711.

77. Spitler, M. T. *Electrochim. Acta* **2007,** *52*, 2294.

Chapter 5

Protection of $GaInP_2$ Photocathodes by Direct Photoelectrodeposition of MoS_x Thin Films

Reprinted with permission from Lancaster, M. et al. Protection of $GaInP_2$ Photocathodes by Direct Photoelectrodeposition of MoS_x Thin Films *ACS Appl. Mater. Interfaces* **2019**, *11*, 25112-25122. Copyright 2019 American Chemical Society.

5.1. Introduction

Direct conversion of solar energy to hydrogen utilizing aqueous electrolytes offers a promising means of producing an energy-dense, storable, and renewable fuel. Despite great interest in photoelectrochemical energy conversion over the past several decades, systems demonstrating stable, high current densities with sufficient photovoltage to split water have yet to emerge. One attractive photoelectrode material for hydrogen production is p-type $GaInP_2$.[1-4] $GaInP_2$ has a nearly optimal band gap (~1.8 eV)[1, 5-6] and can be integrated with lower band gap bottom absorbers (e.g. GaAs or GaInAs) to produce large photovoltages appropriate for unbiased water photoelectrolysis.[5, 7-10] However, the propensity for p-$GaInP_2$ to corrode in aqueous electrolytes and the relativity poor native electrocatalytic activity for H^+ reduction are key barriers for use in renewable hydrogen generation technologies.[11-15]

Numerous coating strategies have been explored and developed for improving semiconductor interface durability including sputtering,[16-18] atomic layer deposition (ALD),[19-22] spin-coating,[23-24] and (photo)electrodeposition.[25-27] For $GaInP_2$ photocathodes, the combination of an ALD-TiO_2 protective layer and a molecular catalyst improved the short-term stability and catalytic activity of the photoelectrode.[19] However, durability of this interface under light-limited operating conditions past 20 hours remains unclear. More recently, a dual catalyst/protective layer design was employed during the deposition of MoS_2 on p-$GaInP_2$.[16] A two-step method of sputtering Mo followed by sulfidization produced an active layer that improved the stability and was more electrocatalytic towards hydrogen evolution. Nevertheless, limited control of the sulfidization process led to unconverted elemental Mo that significantly decreased the observed photocurrent.

Low-temperature photoelectrodeposition offers several unique advantages for preparation of dual purpose (stabilization & electrocatalyst) protective layers on photoelectrodes. First, deposition rates can be precisely controlled by manipulation of the applied current or bias, allowing high fidelity over the deposit thickness. Second, low temperatures prevent interdiffusion and surface phase segregation, common problems for III-V semiconductors subjected to higher temperatures.[28-30] Third, electrochemical equipment needed for photoelectrodeposition are simple and low cost relative to the infrastructure needed for vacuum-based depositions.

In this work, the direct photoelectrodeposition of MoS_x thin films on p-$GaInP_2$ photocathodes is reported and the resulting photoelectrochemical properties are detailed. These earth-abundant catalysts have shown excellent catalytic activity and stability for hydrogen evolution,[31-34] but direct photoelectrodeposition on a planar, III-V photoelectrode surface has not been described. Specifically, the results from MoS_x photoelectrodeposition experiments directly on p-$GaInP_2$ are discussed, including the photoelectrodeposition conditions necessary to produce uniform, thin MoS_x films. Additionally, the structure and composition of these films are detailed and presented in context to the catalytic, optical, and photoelectrochemical properties. Finally, the enhanced stability of the coated p-$GaInP_2$ photoelectrodes relative to the bare material is shown.

5.2. Experimental

Chemicals and Materials

Ammonium tetrathiomolybdate (Acros, 99.95%), potassium sulfate (Acros, 99+%), sulfuric acid (OmniTrace®, EMD Millipore), and Triton X-100 (EMD Millipore) were used as received. All solutions were made with >18 MΩ·cm resistivity water (Milli-Q). Zn-doped p-$GaInP_2$ epilayers with nominal thicknesses of 1 μm and 1 x 10^{17} cm^{-3} dopant density were grown by metalorganic vapor phase epitaxy on p^+-GaAs(100) substrates, miscut 2° towards (110), as described elsewhere.[5] Run numbers for each epilayer are provided in the Supporting Information. Electroplated gold was used to form an ohmic contact to the GaAs substrate.

MoS_x Deposition

$GaInP_2$ epilayers were diced and etched in 18 M sulfuric acid for 1 minute before placing in an open-air, custom Teflon cell and sealing with a Viton o-ring. A three-electrode configuration with a Ag/AgCl (3 M KCl) reference (0.204 V vs. NHE) and a graphite counter electrode was utilized. The electrolyte consisted of 0.001 M ammonium tetrathiomolybdate ($(NH_4)_2MoS_4$) and

0.5 M potassium sulfate (K_2SO_4). Deposition occurred under 50 mW cm^{-2} fiber optic illumination (ThorLabs), as measured with a 1.81 eV band gap $GaInP_2$ reference cell calibrated to an AM1.5G spectrum. Current was applied via a SP-300 potentiostat (BioLogic) in a custom-built, dark Faraday cage. Post deposition, electrodes were placed on glass slides, contacted to conductive copper tape via silver print (GC Electronics), and sealed with epoxy (Loctite EA E-120HP) for photoelectrochemical characterization (See inset of Figure 5.9 for an image of an electrode).

Voltammetry and Durability

Linear-sweep voltammetry was collected with a Solartron 1287 electrochemical interface at a scan rate of 50 mV s^{-1}. All data are shown in 'polarographic' convention, with positive currents indicating cathodic processes. The samples were illuminated with a 300 W Xenon arc lamp (Newport) through a AM 1.5G filter (Oriel) outputting an incident photon intensity equivalent to 100 mW cm^{-2} as calibrated with the $GaInP_2$ reference cell. A single compartment, open-air quartz cell (Starna) containing 0.5 M H_2SO_4 and 0.001 M Triton X-100 (to minimize bubble formation) held the $MoS_x/GaInP_2$ sample in the center, flanked by a $Hg/HgSO_4$ reference electrode (Koslow Scientific) containing a 0.5 M H_2SO_4 filling solution (0.687 V vs. NHE) and a large-area Pt foil counter electrode on either side. Similarly, durability measurements were conducted in the same cell without Triton X-100 using a 250 W tungsten-halogen lamp (Oriel) with an infrared-blocking water filter (Newport). The H_2SO_4 electrolyte was refilled as needed over the course of the durability measurements. All potentials were measured/applied in a three-electrode configuration and are reported with respect to reversible hydrogen electrode.

External Quantum Yield and Reflectance

Quantum yield (incident photon-to-current efficiency) measurements were made between 300-700 nm at 10 nm intervals with a Newport 300 W Xenon arc lamp and a SpectraPro 150 monochromator (Acton Optics). The electrode potential was held at -0.3 V vs. E(RHE) with the photocurrents collected under 2-second light and 2-second dark intervals measured by a VersaStat 4 potentiostat (Princeton Applied Research) and read on a computer controlled by custom LabVIEW software. The monochromator output intensity at each wavelength was separately measured by a calibrated Si photodiode. Reflectance measurements were acquired in air on a Cary 6000i spectrophotometer (Agilent) equipped with an integration sphere using an incidence angle normal to the electrode surface.

Electron Microscopy

Scanning electron micrographs were obtained on a JEOL-7800FLV microscope equipped with a Schottky-type field emission source and an Everhart-Thornley detector at accelerating voltages of 10 kV. Corresponding elemental mapping was collected via an Oxford XMaxN energy-dispersive spectrometer. Scanning transmission electron micrographs were obtained with a FEI Tecnai F20 TEM equipped with a Gatan Enfinium EELS spectrometer and GIF Quantum K2 system at an accelerating voltage of 200 kV. The semi-collection angle was 16 mrad. An energy shift of 120 eV and a dispersion of 0.25 eV/channel were employed to obtain a strong signal-to-noise ratio. EEL spectra in STEM mode was recorded with a CCD camera. The acquisition time for each pixel was 0.5 seconds and the total acquisition time was 23 minutes. The pixel size was 1.4 nm^2. A Pd/Au capping layer was deposited on the sample via sputtering to prevent surface damage during TEM sample preparation. The TEM lamella was prepared by standard focused ion beam (FIB) lift-out techniques followed by Ga ion milling to reduce the final thickness to less than 100 nm.

X-ray Photoelectron Spectroscopy

X-ray photoelectron (XP) spectra were collected with a Kratos AXIS Ultra system operating at base pressures below 10^{-9} torr with a monochromatic Al Kα source (1486.6 eV). Pass energies of 160 eV and 20 eV were used to obtain survey and high-resolution spectra, respectively. Using CasaXPS software, a Shirley-type background correction was applied to the obtained spectra. Binding energies were calibrated to the binding energy for adventitious carbon (284.6 eV)[35] and peak intensities were normalized to that of the Mo 3d$_{5/2}$ peak at 229.14 eV. Peak shapes were set to GL(30), i.e. 30% Gaussian and 70% Lorentzian. For fitting of Mo 3d spectra, peak separation between Mo 3d$_{5/2}$ and 3d$_{3/2}$ doublets was set to 3.1 eV.[36] Peak areas ratios were defined by spin-orbit coupling. The full width at half maximum (*fwhm*) for every peak of the same element was constrained to be the same. For quantification, relative sensitivity factors from the Kratos library were imported into CasaXPS.

Raman Spectroscopy

Raman spectra were collected on a Renishaw inVia microscope using a Nikon 20x objective (NA=0.35) without any addition polarizing excitation/collection optical elements. A 532 nm laser was used as excitation source with an incident power of 35 mW over ~3 μm^2. For annealed samples, annealing was performed in a custom-built tube furnace at 550 °C under a steady flow (100 sccm) of argon (99.998%, Metro Welding Supply).

5.3. Results

MoS_x Photoelectrodeposition

Figure 5.1a highlights the voltammetric responses of bare p-$GaInP_2$ in 0.5 M K_2SO_4 with and without 0.001 M of the MoS_x precursor, $(NH_4)_2MoS_4$. In the absence of illumination, no appreciable current was observed in the potential range of 0.6 V to -0.4 V. Illuminating the electrode with 50 mW cm^{-2} of white light introduced two distinct features. First, a small peak at 0.3 V was observed, consistent with the reduction of surface oxides on p-$GaInP_2$.[13] Second, a large increase in cathodic current beginning at 0.1 V was observed for hydrogen evolution. With 0.001 M of the MoS_x precursor added to solution at the same light intensity, a large positive shift in the photocurrent onset was noted and the light-limited plateau current was attenuated by the deep red solution color. The first voltammetric wave corresponded to the reduction of MoS_4^{2-},[37]

$$MoS_4^{2-} + 2e^- + 2H_2O \rightarrow MoS_2 + 2SH^- + 2OH^- \tag{5.1}$$

however, no change in the electrode appearance was observed by eye. The following wave indicated hydrogen evolution from the deposited catalyst. Similarly, cycling the electrode without illumination in the precursor solution from 0.6 V to -0.4 V resulted in no alteration of the electrode appearance.

A galvanostatic deposition method was utilized to produce uniform thin films. Notably, potentiostatic depositions produced films with significant roughness and led to less reproducible thicknesses. Figure 5.1b shows a representative potential transient for a galvanostatic photoelectrodeposition of MoS_x on bare p-$GaInP_2$ at 0.3 mA cm^{-2} under 50 mW cm^{-2} illumination. After a rapid initial decrease from open-circuit potential, the electrode potential gradually drifted more negative until reaching a quasi-steady-state potential near 0.32 V. While no distinct nucleation feature was observed in the transient, the voltammetry shown in Figure 5.1a suggests the reduction of MoS_4^{2-} occurred at all potentials < 0.6 V, i.e. immediately after the charging current decay. A similar potential transient profile was also observed for longer depositions, as shown in Figure 5.2.

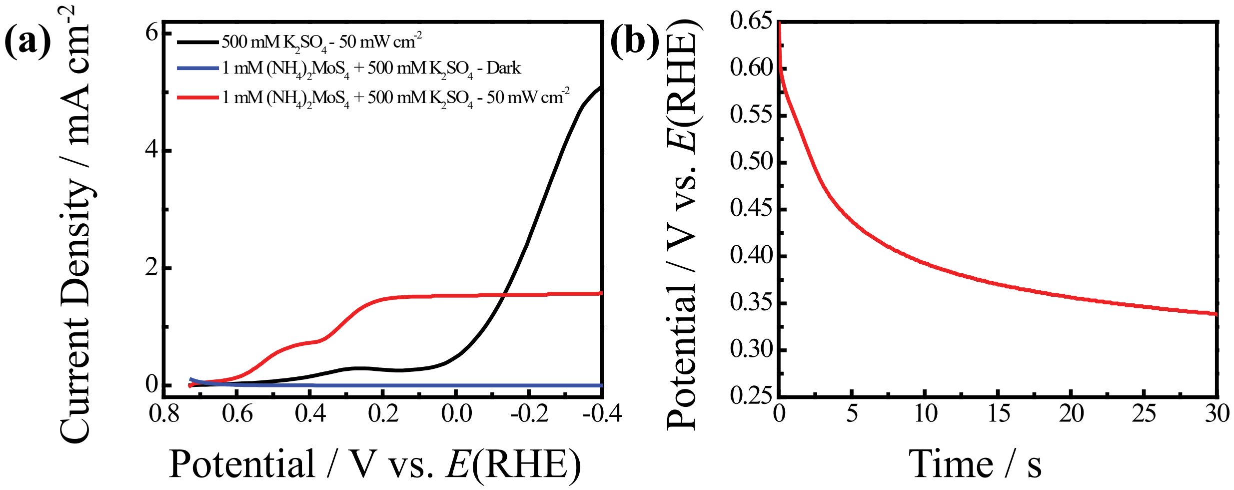

Figure 5.1. (a) Voltammetric responses of a bare p-GaInP$_2$ epilayer in 0.5 M K$_2$SO$_4$ under 50 mW cm^{-2} illumination (black), in 0.001 M (NH$_4$)$_2$MoS$_4$ + 0.5 M K$_2$SO$_4$ in the dark (blue), and in 0.001 M (NH$_4$)$_2$MoS$_4$ + 0.5 M K$_2$SO$_4$ under 50 mW cm^{-2} illumination (red). Scan rate: 50 mV s^{-1}. (b) Potential transient for the galvanostatic deposition of MoS$_x$ thin films on p-GaInP$_2$ under 50 mW cm^{-2} illumination. Applied current density: 0.3 mA cm^{-2}.

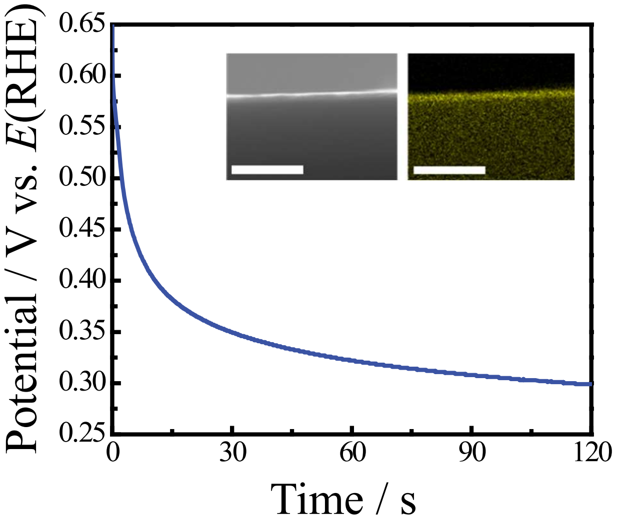

Figure 5.2. Potential transient for the galvanostatic deposition of MoS_x thin films on p-$GaInP_2$ under 50 mW cm^{-2} illumination. Solution pH: 6.1. Applied current density: 0.3 mA cm^{-2}. Insets: SEM image and corresponding Mo/S elemental map of the resulting deposit. Scale bars: 500 nm.

Structure and Composition of Deposited MoS_x Films

Electron microscopy coupled with spectroscopic techniques was used to determine the film thickness, composition, and structure. A representative cross-section, bright-field scanning transmission electron microscopy (STEM) image of a film on p-$GaInP_2$ photoelectrodeposited at 0.3 mA cm^{-2} for 30 seconds under 50 mW cm^{-2} illumination in 0.001 M $(NH_4)_2MoS_4$ is shown in Figure 5.3a. An ~8 nm thick MoS_x film was observed between $GaInP_2$ and the Pd/Au capping layer deposited during STEM sample preparation. STEM analysis on multiple MoS_x films grown on separate $GaInP_2$ substrates under the same conditions produced film thicknesses ranging between 8-10 nm. An additional ~0.75 nm thick layer was consistently observed between the $GaInP_2$ substrate and the MoS_x film and attributed to a surface oxide. A longer deposition time of 2 minutes produced thicker films on the order of 40 nm (Figure 5.2, inset). Figure 5.3b shows the corresponding dark field image of the MoS_x. A sharp interface is apparent below the capping layer, indicating a nominally smooth top surface over the imaged area. Additional STEM/EDS mapping in Figure 5.4 showed a distinct diminution in the Ga, In, and P signals in the region of the film. Figure 5.3c highlights sulfur content in the films. The S EELS map in Figure 5.3c collected from the S-$L_{2,3}$ edge at 165 eV confirmed that the films were sulfur-containing throughout. Analogous Mo mapping in Figure 5.5b was less clear on the absolute Mo content since the Mo-M_3 and Mo-M_2 edges strongly overlap with the tail of the C-K edge (Figure 5.5c). Nevertheless, the data were consistent that the as-deposited films were composed of S uniformly.

Separate assessment of the chemical oxidation states of Mo and S was performed via high resolution XPS. High resolution XP spectra (raw data, fits, and residuals) for the Mo 3d and S 2p regions are shown in Figures 5.6a,b (fitting details *vide supra*). In Figure 5.6a, the Mo 3d region was composed of three Mo doublets corresponding to three different oxidation states: Mo(IV), Mo(V), and Mo(VI). In addition, a single peak at 226.9 eV was observed corresponding to an S 2s signal.[2, 34] The Mo(IV) doublet and the S 2s signals suggest molybdenum disulfide.[2, 34, 36] The Mo(V) doublet was consistent with a ternary oxysulfide species (MoO_xS_y).[2, 36, 38] The doublet for Mo(VI) suggested some molybdenum oxide (MoO_3) also present.[2, 34]

The S 2p spectrum in Figure 5.6b was fit to several S oxidation states. The binding energies of these two sets of doublets were consistent with a mix of S^{2-} and S_2^{2-} anions present in MoS_x, widely reported for MoS_x materials with no long-range structural order, i.e. amorphous.[2, 34, 36, 38]

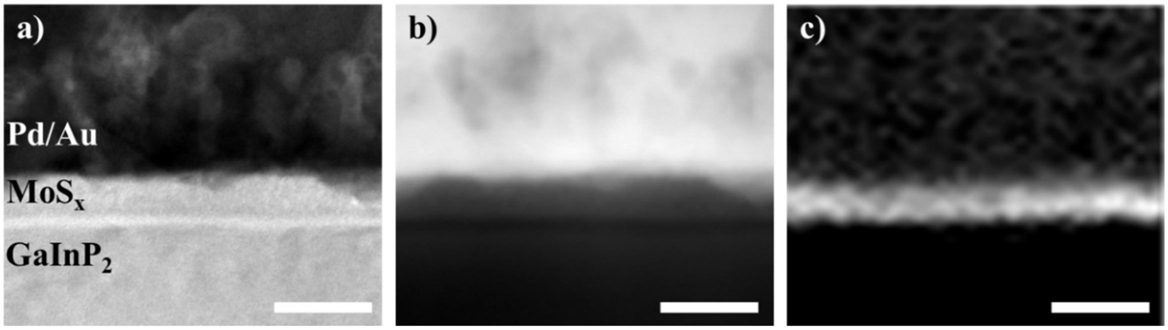

Figure 5.3. (a) Bright-field and (b) dark-field STEM images of the as-deposited MoS$_x$ thin film and GaInP$_2$ interface. (c) Corresponding S-L$_{2-3}$ edge EELS map of the MoS$_x$ deposit and GaInP$_2$ interface. Sulfur signal is shown in white against a black background. Scale bars: 10 nm.

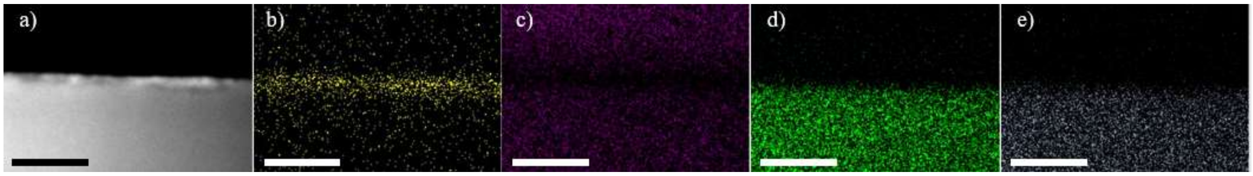

Figure 5.4. (a) STEM image of a $MoS_x/GaInP_2$ sample deposited for 30 seconds. (b) S-K/Mo-L (c) Ga-K (d) P-K and (d) In-L elemental maps. Scale bars: 50 nm.

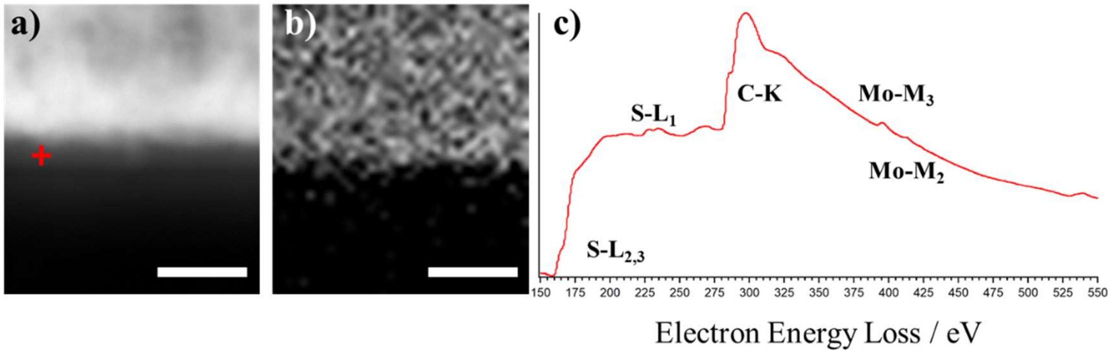

Figure 5.5. (a) Cross-section STEM image of a MoS_x thin film photoelectrodeposited on p-$GaInP_2$. The red arrow indicates the acquisition location of the EELS spectrum. Scale bar: 20 nm. (b). Mo-M_3 edge EELS map. Scale bar: 20 nm. (c) EELS map of MoS_x film.

Additionally, no elemental sulfur peaks were required to fit the S 2p spectrum. Combined, the relative intensities across Figure 5.6 suggested a large portion of the film is composed of MoS_2. Quantification of the Mo and S spectra suggested an approximate Mo:S ratio of 1:1.6, corresponding to a majority MoS_2 makeup with some oxide/oxysulfide species present. As such, the films are collectively referred to as MoS_x.

Separate analyses were performed to ascertain the crystallinity of the MoS_x film. All X-ray diffraction measurements on the as-prepared film yielded no evidence of crystallinity but the detection limit for the low total amount of material was not conclusive in this regard. Separate Raman analyses were performed to bolster this point. Raman spectra for bare p-$GaInP_2$, p-$GaInP_2$ with an as-deposited film, and p-$GaInP_2$ after film photoelectrodeposition and annealing for 30 min at 550 °C under Ar(g) are shown in Figure 5.7. For the bare sample, the three clear Raman peaks at 381, 364, and 330 cm^{-1} were observed, consistent with the two longitudinal optical phonon modes and one transverse optical phonon mode, respectively, for ordered $GaInP_2$.[39] The as-deposited sample shows an essentially identical spectrum, indicating the as-deposited films showed no Raman signatures in this bandwidth. The Raman spectrum after annealing featured an additional small peak at 405 cm^{-1}. This signal was consistent with the A_{1g} mode of crystalline MoS_2.[40]

Photoelectrochemical Properties of the MoS_x/p-$GaInP_2$ Photocathode

The photoelectrochemical properties of p-$GaInP_2$ before and after film photoelectrodeposition are shown in Figure 5.8. Figure 5.8a shows the steady-state linear sweep voltammograms of p-$GaInP_2$ before and after film deposition when immersed in 0.5 M H_2SO_4 and 0.001 M Triton X-100 under AM 1.5G illumination. The reversible potential for H^+/H_2 is indicated by the vertical, dashed line. Several key differences in the voltammetry of the two electrodes are apparent. First, the onset potential for the hydrogen evolution reaction is shifted significantly. At a current density of 1 mA cm^{-2}, the potential of the coated electrode is 460 mV more positive than prior to film deposition. Next, the light-limited photocurrent density of the coated p-$GaInP_2$ electrode is essentially unchanged relative to the bare p-$GaInP_2$ electrode (11.7 vs. 11.0 mA cm^{-2}, respectively). These features were consistent across two thin film electrodes prepared from different p-$GaInP_2$ epilayers (with similar material properties as shown), as shown in Figure 5.9. Figure 5.8b shows representative external quantum yield measurements for p-$GaInP_2$ before and

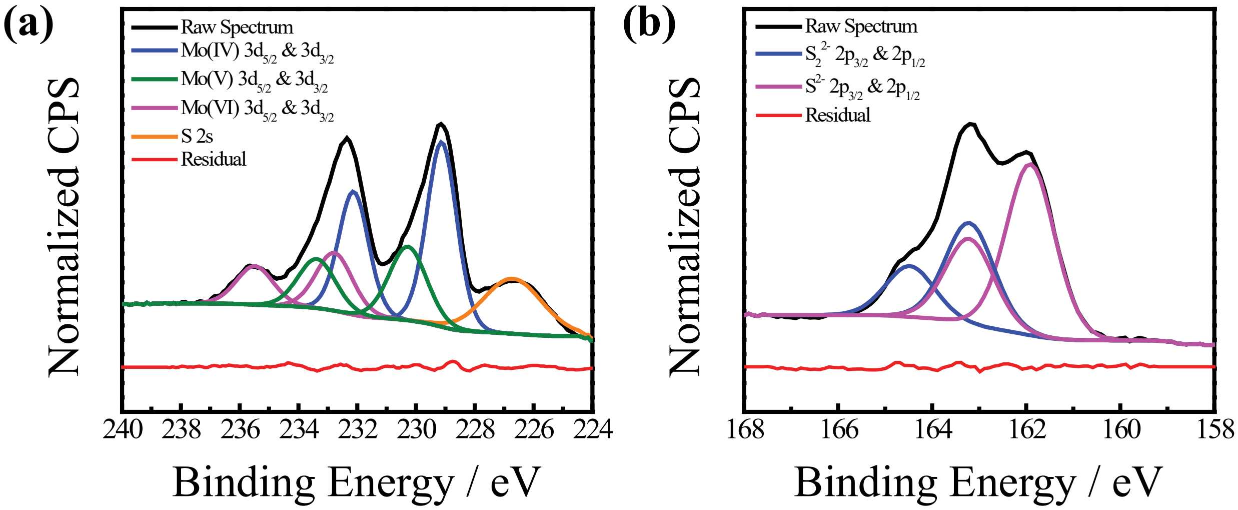

Figure 5.6. High resolution (a) Mo 3d and (b) S 2p XP spectra of the as-deposited MoS$_x$ thin film. Residuals are shown in red below the fitted spectra.

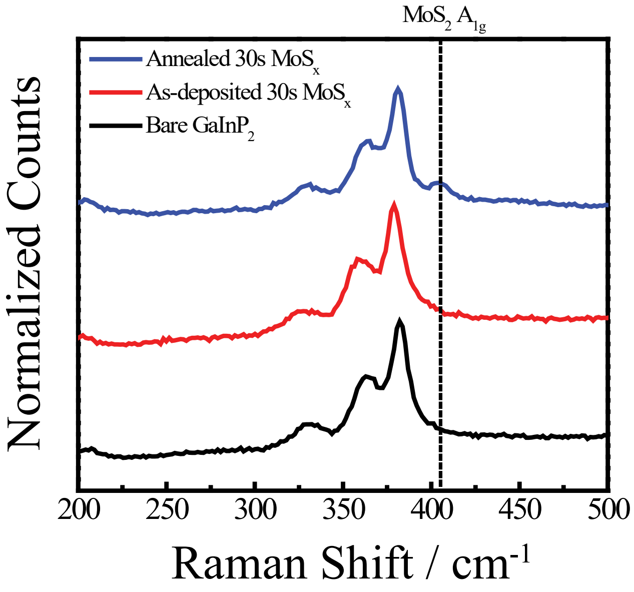

Figure 5.7. Raman spectra of bare $GaInP_2$, as-deposited $MoS_x/GaInP_2$, and annealed $MoS_x/GaInP_2$ electrodes. The dashed line indicates the location of the A_{1g} mode of crystalline MoS_2.

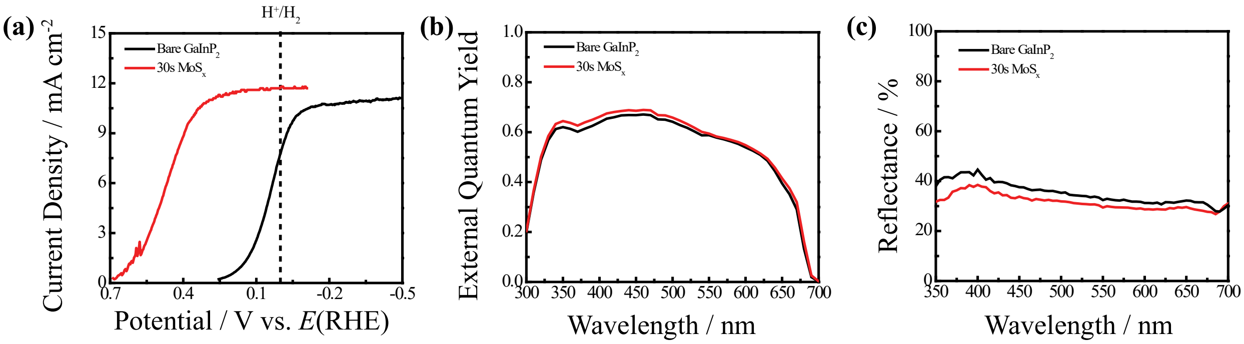

Figure 5.8. (a) Voltammetric responses of MoS_x/p-$GaInP_2$ and bare p-$GaInP_2$ photocathodes in 0.5 M H_2SO_4 + 0.001 M Triton X-100 under AM 1.5G illumination. Scan rate: 50 mV s^{-1}. The dashed line indicates the reversible potential for the hydrogen evolution reaction on this scale. (b) External quantum yield measurements for the same electrodes in 0.5 M H_2SO_4. Applied bias: -0.3 V vs. *E*(RHE) (c) Reflectance measurements of MoS_x/p-$GaInP_2$ and bare p-$GaInP_2$ electrodes acquired without electrolyte.

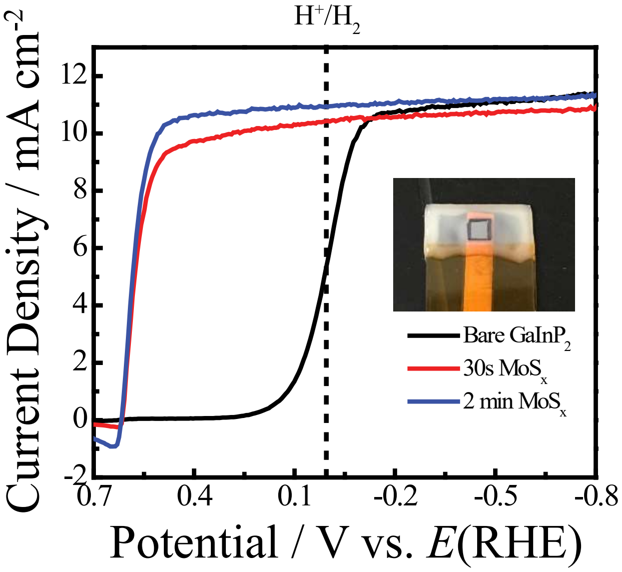

Figure 5.9. Voltammetric responses of MoS_x/p-$GaInP_2$ and bare p-$GaInP_2$ photocathodes in 0.5 M H_2SO_4 + 0.001 M Triton X-100 under AM 1.5G illumination. Scan rate: 50 mV s^{-1}. The dashed line indicates the reversible potential for the hydrogen evolution reaction on this scale. Inset: Epoxy electrode used for all photoelectrochemical characterization. Electrode areas ranged from 0.1-0.2 cm^2.

after film photoelectrodeposition. Despite a slight increase in the quantum yield at shorter wavelengths, there was no appreciable change in the quantum yield profile across the range of visible wavelengths. However, the reflectance data, depicted in Figure 5.8c, shows a measurable difference between the two types of electrodes. At all wavelengths shown, a 5-10% change in the reflectance was noted, with the largest differences occurring at shorter wavelengths.

Photoelectrochemical measurements recorded over longer periods of time were performed to assess the relative durability of the as-deposited coatings (Figure 5.10). Photocurrent-time measurements were performed for all electrodes under AM 1.5G illumination in the absence of any surfactant at an applied potential of 0 V vs. *E*(RHE), i.e. under conditions where the photocurrent is light-limited for the MoS_x sample and near light-limited for the bare sample. An additional durability measurement was performed at +0.25 V to assess durability closer to the maximum power point. The photocurrent of the bare p-$GaInP_2$ electrode decayed quickly, reaching near zero within 3 hours. After the photoelectrodeposition using the same conditions as for Figure 5.3, the photocurrent of the p-$GaInP_2$ photoelectrode was markedly more stable. At 0 V vs *E*(RHE), the electrode maintained 85% of the initial photocurrent over 50 hours. Even after 100 hours under light-limited conditions, 80% of the initial photocurrent was observed. Durability on a sample produced by the same 30s photoelectrodeposition conditions at 0.25 V resulted in similar levels of stability over 50 h. P-type $GaInP_2$ electrodes coated with a film photoelectrodeposited for shorter times (10s) still showed some improved durability over bare p-$GaInP_2$ but less stability than the films photoelectrodeposited for 30s, losing 30% of the initial photocurrent density over 50 hours of continuous operation.

5.4. Discussion

The collective data supports three main points. First, photoelectrochemical reduction of $(NH_4)_2MoS_4$ on p-$GaInP_2$ is a straightforward route to obtain uniform coatings. The film material is disordered and results in negligible optical losses in the photoelectrochemical responses of p-$GaInP_2$. Second, the as-prepared films are electrocatalytic towards H^+ reduction. Third, such films impart enhanced durability to p-$GaInP_2$, similar to MoS_2 films deposited by vapor phase methods. These points are described below.

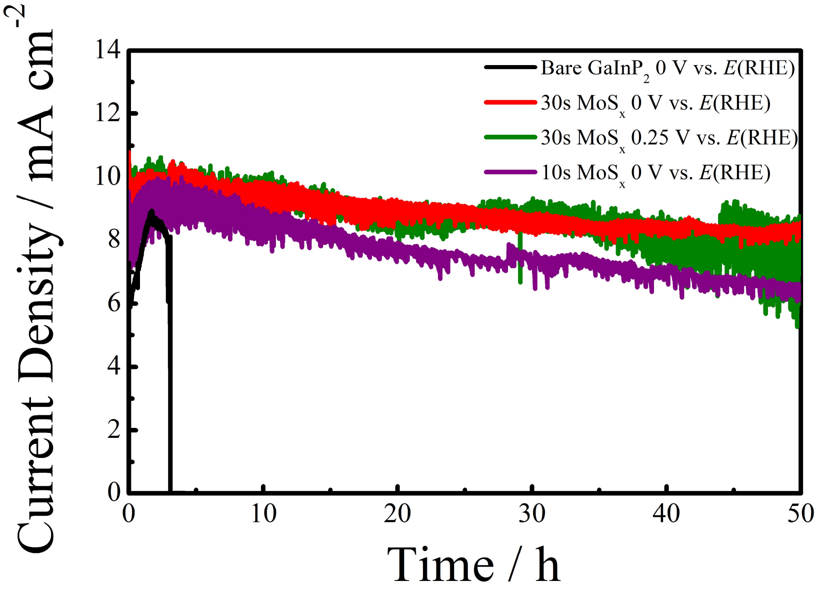

Figure 5.10. Durability measurements for bare p-GaInP$_2$, 10s deposited MoS$_x$/p-GaInP$_2$, and 30s deposited MoS$_x$/p-GaInP$_2$ photocathodes in 0.5 M H_2SO_4 under AM 1.5G illumination at an applied bias of either 0.0V or 0.25 V vs. *E*(RHE).

Photoelectrodeposited Thin Films of MoS_x

Although the photoelectrochemical reduction of $(NH_4)_2MoS_4$ on p-$GaInP_2$ can readily occur under a variety of conditions, this work highlights parameters necessary for thin, uniform films. First, a light intensity of 50 mW cm^{-2} white light was utilized, as full 1-sun illumination resulted in much thicker films, even for short deposition times. Second, $(NH_4)_2MoS_4$ concentrations on the order of 0.001 M were optimal. Higher concentrations resulted in strongly colored solutions that severely attenuated illumination. Lower concentrations resulted in sporadic, non-uniform deposits. Third, galvanostatic rather than voltammetric depositions yielded the most uniform films. Low current densities (~10^{-4} A cm^{-2}) also yielded the most continuous films. Higher current densities produced thicker (>60 nm) and rougher films which incurred greater optical losses and correspondingly lower attainable photocurrents.

The as-photoelectrodeposited thin films were neither crystalline nor homogeneous in composition. The cumulative XP spectra and EELS mapping suggest these films are a mixture of MoS_2 and non-stoichiometric molybdenum sulfide, i.e. MoS_x. The data are presently unclear whether any oxysulfide forms natively during photoelectrodeposition. Additionally, the distribution of different Mo/S valence states (e.g. clustering) within the film is uncertain. However, reactivity of the films towards oxygen would be consistent with the determination that the films are not strongly ordered. Crystalline features (e.g. Raman modes) were only observed after some annealing, implying that the photoelectrodeposition process yields a metastable form of MoS_x.

Still, a noteworthy feature of the photoelectrodeposition process was the apparent lack of Mo- and S-enrichment. This feature, in conjunction with the relative simplicity of the photoelectrodeposition process, stands in strong contrast to other methodologies for coating p-$GaInP_2$ with MoS_2-based coatings. A two-step Mo sputtering and subsequent sulfidization process has been reported previously for modifying p-$GaInP_2$ that indicated it is difficult to fully convert Mo^0 films, especially at the interface.[16] Although the sub-stoichiometry of the metal sulfide (and presence of Mo^0) apparently had minimal impact on the stability and catalytic activity of the electrode interface, the light-limited photocurrent was attenuated. This may signify an inherent limitation to the sulfidization process. That is, strong interactions between the Mo metal and the substrate, as well as the presence of coordinated oxygen could inhibit complete sulfidization within accepted thermal and temporal budgets.[41-42] Additionally, it is unclear whether sputtering damage occurs/impacts the performance of photoelectrodes during catalyst deposition. Plasma damage to sputtering substrates and resulting films is well documented, where ion bombardment can create surface defects that impact electrical properties.[43-45] Regardless, those complications did not affect this work. The lack of Mo^0 and the ability to deposit optically thin films stand as major practical advantages of the method presented here. Although the simplicity of ambient electrodeposition apparatus relative to high temperature equipment is well established at this point,[46] it merits further mentioning that ambient temperature deposition also avoids the inter-diffusion problems associated with exposing the film/electrode to high temperatures.[28]

A further notable aspect observed here is the absence of substantial optical losses after coating. The near invariance in light-limited photocurrents in Figure 5.8a implies these coatings are essentially transparent to the incident illumination. Any deposited material with a refractive index between that of $GaInP_2$ and the liquid electrolyte will necessarily decrease the amount of incident illumination reflected. Although it is tempting to ascribe some additional light trapping between the film and p-$GaInP_2$ as the source for the slight photocurrent enhancement, replicate samples showed the same primary observation (i.e. the photocurrent magnitude was the same) but with no discernable enhancement. This observation could speak to slight variations in the specific refractive indices or absorbance between films and was not assessed further. Nevertheless, the principal fact that films which were electrocatalytic yielded no substantial changes in the reflectance, wavelength-dependent quantum yields for photocurrent, and total white-light photocurrent is clear that the optical properties of the modified p-$GaInP_2$ photocathodes are well-suited for water splitting. This point is especially true for multi-junction photoelectrode architectures, where minimizing optical losses between layers is critical.[5, 9-10]

Electrocatalytic Properties of MoS_x

The marked difference in the current-potential responses under illumination before and after modification of p-$GaInP_2$ speaks strongly to the electrocatalytic nature of the as-prepared MoS_x films. That is, the as-prepared MoS_x films act as potent electrocatalysts for H^+ reduction. This point can be understood from the cumulative literature on the electrocatalytic nature of MoS_2. Simply, while crystalline MoS_2 is a layered material with extremely stable basal planes,[47-48] the most potent sites for H^+ adsorption and reduction are believed to be the under-coordinated Mo-S units at edge sites.[49-51] In fact, amorphous, heavily disordered, and defect-rich MoS_2 has been intentionally targeted as an ideal morphology of this sulfide for electrocatalysis.[31, 34, 50, 52-53] These disordered MoS_2/MoS_x materials can exhibit exchange current densities upwards of 10^{-5} A cm^{-2}, compared to 10^{-4} A cm^{-2} for Pt.[32, 54] The onset potential for hydrogen evolution of MoS_x thin films deposited for 30 seconds in this work (0.68 and 0.62 V at 0.1 mA cm^{-2}) surpasses other $MoS_{2/x}$ films on p-$GaInP_2$ photocathodes (0.36[16] and ~0.49[2] V at 0.1 mA cm^{-2}). Accordingly, these results suggest that the photoelectrodeposition process employed here also naturally yields a very active form of MoS_x.

Stability

The long operational life of the modified p-$GaInP_2$ electrodes is encouraging and noteworthy. Fundamentally, the stability of a photocathode immersed in water can be understood as a function of two (or more) current processes operating in parallel at the semiconductor/solution interface.[55] Concurrent to chemically-induced corrosion processes, photogenerated electrons can either participate in the electrochemical reduction of species in solution or in the electrochemical reduction of the semiconductor itself at the interface, with the relative fractions dictated by the 'resistance' (i.e. kinetics) of the two current branches. In the absence of any electrocatalyst, the current flowing across a p-$GaInP_2$ electrode in water under hydrogen evolving conditions quickly decreases because the concurrent reduction of the group III elements to zero-valent metals is kinetically competitive with H^+ to H_2.[13, 55-57] This aspect is clearly reflected in the rapid current loss in Figure 5.10 for the bare p-$GaInP_2$ photocathode. The substantially slower current decays of the p-$GaInP_2$ photocathodes modified by MoS_x reflect the fact that H^+ reduction became much more kinetically facile.

To be clear, the stability of these modified p-$GaInP_2$ electrodes is improved but by no means indefinite. Any loss in photocurrent indicates that some finite, parallel degradation process. Any residual faradaic current not directed towards H_2 evolution will eventually lead to catastrophic failure if it is coupled to some corrosion of the photoelectrode.[56-57] A detailed analysis was not performed on the failure mechanisms of these films. Failure could involve catalyst dissolution and/or poor catalyst adhesion. While the stability of MoS_2 in water-splitting reactions is known.[18] molybdenum oxides are susceptible towards dissolution under hydrogen-evolving conditions,[58-59] exposing the underlying substrate. Accordingly, elimination of any oxides in the film should be pursued to enhance stability for much longer operating times. Additionally, the native surface oxide on $GaInP_2$ likely influences adhesion of MoS_x. There is no reason *a priori* to believe adhesion should be strong at this interface but the evidence is clear that films adhere on the time scale of days. Specifically modifying $GaInP_2$ surfaces prior to photoelectrodeposition to enhance binding interactions with MoS_x may be required for much longer photoelectrolysis times. On this front, several routes for covalent modification of III-V semiconductor surfaces are known.[60-61]

5.5. Conclusions

The cumulative data show that direct photoelectrodeposition of MoS_x thin films on p-$GaInP_2$ epilayers provides excellent catalytic activity and enhanced durability for photoelectrochemical hydrogen evolution. The key advancement demonstrated by this work is the ability to fabricate thin films on high efficiency III-V substrates with high catalytic performance and negligible photocurrent loss via an ambient benchtop electrodeposition requiring only aqueous solutions and simple electronics. A notable conclusion is that these films can stabilize otherwise corrosion-prone materials, setting the basis for future studies aimed at depositing other catalytically active, yet stable materials on photoelectrodes. From a practical standpoint, the fact this stability enhancement was achieved without any other additional protection layer greatly simplifies interface design. Nevertheless, controlling the interfacial chemistry of the $GaInP_2$ electrode before photoelectrodeposition may also prove useful in manipulating the film morphology for adjusting the deposit's optical properties or altering the system energetics for enhanced overall performance. The fact that the photoelectrodeposited films shown here already demonstrate 50 hours of operation is encouraging, particularly given the ease and rapidity of their preparation.

5.6. References

1. MacLeod, B. A.; Steirer, K. X.; Young, J. L.; Koldemir, U.; Sellinger, A.; Turner, J. A.; Deutsch, T. G.; Olson, D. C. *ACS Appl. Mater. Interfaces* **2015,** *7*, 11346.

2. Gu, J.; Aguiar, J. A.; Ferrere, S.; Steirer, K. X.; Yan, Y.; Xiao, C. X.; Young, J. L.; Al-Jassim, M.; Neale, N. R.; Turner, J. A. *Nat. Energy* **2017,** *2* (2).

3. Wang, H. L.; Deutsch, T.; Turner, J. A. *J. Electrochem. Soc.* **2008,** *155*, 91.

4. Kocha, S. S.; Turner, J. A.; Nozik, A. J. *J. Electroanal. Chem.* **1994,** *367*, 27.

5. Young, J. L.; Steiner, M. A.; Doscher, H.; France, R. M.; Turner, J. A.; Deutsch, T. G. *Nat. Energy* **2017,** *2*.

6. Geisz, J. F.; Steiner, M. A.; Garcia, I.; Kurtz, S. R.; Friedman, D. J. *Appl. Phys. Lett.* **2013,** *103* (4).

7. Bertness, K. A.; Kurtz, S. R.; Friedman, D. J.; Kibbler, A. E.; Kramer, C.; Olson, J. M. *Appl. Phys. Lett.* **1994,** *65*, 989.

8. Kocha, S. S.; Montgomery, D.; Peterson, M. W.; Turner, J. A. *Sol. Energ. Mat. Sol. Cells* **1998,** *52*, 389.

9. Khaselev, O.; Turner, J. A. *Science* **1998,** *280*, 425.

10. May, M. M.; Lewerenz, H. J.; Lackner, D.; Dimroth, F.; Hannappel, T. *Nat. Commun.* **2015,** *6*.

11. Bansal, A.; Turner, J. A. *J. Phys. Chem. B* **2000,** *104*, 6591.

12. Wang, H.; Deutsch, T.; Welch, A.; Turner, J. A. *Int. J. Hydrog. Energy* **2012,** *37*, 14009.

13. Khaselev, O.; Turner, J. A. *J. Electrochem. Soc.* **1998,** *145*, 3335.

14. Kocha, S. S.; Turner, J. A. *J. Electrochem. Soc.* **1995,** *142*, 2625.

15. Kocha, S. S.; Peterson, M. W.; Nelson, A. J.; Rosenwaks, Y.; Arent, D. J.; Turner, J. A. *J. Phys. Chem.* **1995,** *99*, 744.

16. Britto, R. J.; Benck, J. D.; Young, J. L.; Hahn, C.; Deutsch, T. G.; Jaramillo, T. F. *J. Phys. Chem. Lett.* **2016,** *7*, 2044.

17. Sun, K.; Saadi, F. H.; Lichterman, M. F.; Hale, W. G.; Wang, H. P.; Zhou, X. H.; Plymale, N. T.; Omelchenko, S. T.; He, J. H.; Papadantonakis, K. M.; Brunschwig, B. S.; Lewis, N. S. *Proc. Natl. Acad. Sci. U.S.A.* **2015,** *112*, 3612.

18. Laursen, A. B.; Pedersen, T.; Malacrida, P.; Seger, B.; Hansen, O.; Vesborg, P. C. K.; Chorkendorff, I. *Phys. Chem. Chem. Phys.* **2013,** *15*, 20000.

19. Gu, J.; Yan, Y.; Young, J. L.; Steirer, K. X.; Neale, N. R.; Turner, J. A. *Nat. Mater.* **2016,** *15*, 456.

20. Hu, S.; Shaner, M. R.; Beardslee, J. A.; Lichterman, M.; Brunschwig, B. S.; Lewis, N. S. *Science* **2014,** *344*, 1005.

21. Zhou, X. H.; Liu, R.; Sun, K.; Papadantonakis, K. M.; Brunschwig, B. S.; Lewis, N. S. *Energ. Environ. Sci.* **2016,** *9*, 892.

22. Rovelli, L.; Tilley, S. D.; Sivula, K. *ACS Appl. Mater. Interfaces* **2013,** *5*, 8018.

23. Xu, Y. F.; Wang, X. D.; Chen, H. Y.; Kuang, D. B.; Su, C. Y. *Adv. Funct. Mater.* **2016,** *26*, 4414.

24. Xiao, J. R.; Huang, H. L.; Huang, Q. Y.; Li, X.; Hou, X. L.; Zhao, L.; Ma, R.; Chen, H.; Li, Y. D. *Appl. Catal. B-Environ.* **2017,** *212*, 89.

25. Prabhakar, R. R.; Septina, W.; Siol, S.; Moehl, T.; Wick-Joliat, R.; Tilley, S. D. *J. Mater. Chem. A* **2017,** *5*, 23139.

26. Morales-Guio, C. G.; Liardet, L.; Mayer, M. T.; Tilley, S. D.; Gratzel, M.; Hu, X. L., *Angew. Chem. Int. Ed.* **2015,** *54*, 664.

27. Kageshima, Y.; Minegishi, T.; Sugisaki, S.; Goto, Y.; Kaneko, H.; Nakabayashi, M.; Shibata, N.; Domen, K. *ACS Appl. Mater. Interfaces* **2018,** *10*, 44396.

28. Francis, C.; Bradley, M. A.; Boucaud, P.; Julien, F. H.; Razeghi, M. *Appl. Phys. Lett.* **1993,** *62*, 178.

29. Lita, B.; Goldman, R. S.; Phillips, J. D.; Bhattacharya, P. K. *Appl. Phys. Lett.* **1999,** *75*, 2797.

30. Pearton, S. J.; Malm, D. L.; Heimbrook, L. A.; Kovalchick, J.; Abernathy, C. R.; Caruso, R.; Vernon, S. M.; Haven, V. E. *Appl. Phys. Lett.* **1987,** *51*, 682.

31. Benck, J. D.; Chen, Z. B.; Kuritzky, L. Y.; Forman, A. J.; Jaramillo, T. F. *ACS Catal.* **2012,** *2*, 1916.

32. Merki, D.; Hu, X. L. *Energ. Environ. Sci.* **2011,** *4*, 3878.

33. Deng, Y. L.; Ting, L. R. L.; Neo, P. H. L.; Zhang, Y. J.; Peterson, A. A.; Yeo, B. S. *ACS Catal.* **2016,** *6*, 7790.

34. Merki, D.; Fierro, S.; Vrubel, H.; Hu, X. L. *Chem. Sci.* **2011,** *2*, 1262.

35. Barr, T. L.; Seal, S. *J. Vac. Sci. Technol. A* **1995,** *13*, 1239.

36. Vrubel, H.; Hu, X. L. *ACS Catal.* **2013,** *3*, 2002.

37. Ponomarev, E. A.; Neumann-Spallart, M.; Hodes, G.; Levy-Clement, C. *Thin Solid Films* **1996,** *280*, 86.

38. Benoist, L.; Gonbeau, D.; Pfisterguillouzo, G.; Schmidt, E.; Meunier, G.; Levasseur, A. *Thin Solid Films* **1995,** *258*, 110.

39. Cheong, H. M.; Mascarenhas, A.; Ernst, P.; Geng, C. *Phys. Rev. B* **1997,** *56*, 1882.

40. Li, H.; Zhang, Q.; Yap, C. C. R.; Tay, B. K.; Edwin, T. H. T.; Olivier, A.; Baillargeat, D. *Adv. Funct. Mater.* **2012,** *22*, 1385.

41. Spevack, P. A.; Mcintyre, N. S. *J. Phys. Chem.* **1993,** *97*, 11031.

42. Lee, B. S.; Rapp, R. A. *J. Electrochem. Soc.* **1984,** *131*, 2998.

43. Fonash, S. J.; Ashok, S.; Singh, R. *Appl. Phys. Lett.* **1981,** *39*, 423.

44. Kim, H. K.; Lee, K. S.; Kwon, J. H. *Appl. Phys. Lett.* **2006,** *88*.

45. Kelly, P. J.; Arnell, R. D. *Vacuum* **2000,** *56*, 159.

46. Fahrenkrug, E.; Maldonado, S. *Acc. Chem. Res.* **2015,** *48*, 1881.

47. Fleischauer, P. D. *ASLE Trans.* **1984,** *27*, 82.

48. Parzinger, E.; Miller, B.; Blaschke, B.; Garrido, J. A.; Ager, J. W.; Holleitner, A.; Wurstbauer, U. *ACS Nano* **2015,** *9*, 11302.

49. Li, G. Q.; Zhang, D.; Qiao, Q.; Yu, Y. F.; Peterson, D.; Zafar, A.; Kumar, R.; Curtarolo, S.; Hunte, F.; Shannon, S.; Zhu, Y. M.; Yang, W. T.; Cao, L. Y. *J. Am. Chem. Soc.* **2016,** *138*, 16632.

50. Xie, J. F.; Zhang, H.; Li, S.; Wang, R. X.; Sun, X.; Zhou, M.; Zhou, J. F.; Lou, X. W.; Xie, Y. *Adv. Mater.* **2013,** *25*, 5807.

51. Wu, Z. Z.; Fang, B. Z.; Wang, Z. P.; Wang, C. L.; Liu, Z. H.; Liu, F. Y.; Wang, W.; Alfantazi, A.; Wang, D. Z.; Wilkinson, D. P. *ACS Catal.* **2013,** *3*, 2101.

52. Ye, G. L.; Gong, Y. J.; Lin, J. H.; Li, B.; He, Y. M.; Pantelides, S. T.; Zhou, W.; Vajtai, R.; Ajayan, P. M. *Nano Lett.* **2016,** *16*, 1097.

53. Tan, J.; Yang, W.; Oh, Y.; Lee, H.; Park, J.; Moon, J. *ACS Appl. Mater. Interfaces* **2018,** *10*, 10898.

54. Sheng, W. C.; Gasteiger, H. A.; Shao-Horn, Y. *J. Electrochem. So.c* **2010,** *157*, 1529.

55. Gerischer, H. *J. Electroanal. Chem.* **1977,** *82*, 133.

56. Brown, E. S.; Peczonczyk, S. L.; Wang, Z. J.; Maldonado, S. *J. Phys. Chem. C* **2014,** *118*, 11593.

57. Butler, M. A.; Ginley, D. S. *J. Electrochem. Soc.* **1980,** *127*, 1273.

58. Saji, V. S.; Lee, C. W. *ChemSusChem* **2012,** *5*, 1146.

59. Chen, Z. B.; Cummins, D.; Reinecke, B. N.; Clark, E.; Sunkara, M. K.; Jaramillo, T. F. *Nano Lett.* **2011,** *11*, 4168.

60. Garner, L. E.; Steirer, K. X.; Young, J. L.; Anderson, N. C.; Miller, E. M.; Tinkham, J. S.; Deutsch, T. G.; Sellinger, A.; Turner, J. A.; Neale, N. R. *ChemSusChem* **2017,** *10*, 767.

61. Peczonczyk, S. L.; Mukherjee, J.; Carim, A. I.; Maldonado, S. *Langmuir* **2012,** *28*, 4672.

CHAPTER 6

Conclusions and Future Work

6.1. Conclusions

This thesis describes methods to measure and control charge transfer processes at semiconductor/liquid interfaces. Specifically, the SUME design and interpretation of the voltammetric response has been extensively detailed. Additionally, electrodeposition of ultra-thin catalyst films was shown to produce highly stable photoelectrodes. Cumulatively, the advances in electroanalysis and materials preparation demonstrated here have established a ground work for a wide variety of topics aimed at further advancing semiconductor (photo)electrochemistry.

Several specific research directions can be derived from this thesis. First, utilizing the SUME platform to directly observe the famed 'inverted' region of charge transfer would represent one of the most significant advances in charge transfer theory in the last several decades. Doing so, however, requires very careful design of both the SUME characteristics and electrolyte composition. Relatedly, examining other previously challenging questions in semiconductor electrochemistry, such as charge transfer from a perfect/defect-free semiconductor interface may be suitable for small SUMEs. Avenues in photoelectrochemical energy conversion may also be pursued. Utilizing electrodeposition for stabilizing photoanodes and designing array-based photoelectrodes could further address the need for functional and commercially-relevant photoelectrochemical systems. These aims are described in more detail below.

6.2. Future Directions

Direct Observation of 'Inverted' Behavior at III-V SUMEs

To date, few direct observations of charge transfer in the inverted regime at solid/liquid electrode contacts have been made.[1-4] As currently designed, the SUME platform developed herein may be able to tackle this challenge given the high obtainable current densities, wide mass-transport window, and flexibility/interchangeability of the semiconductor substrate. A key aspect of the analysis of the voltammetric response presented in Chapter 4 is the consideration of the applied potential distribution across the semiconductor/liquid interface. Under large applied bias (negative applied potential for n-type materials considered here), charges accumulate near the semiconductor surface and increase the capacitance to the point where potential begins to drop across the Helmholtz layer. When this occurs, band edges will unpin and begin to move upward (more negative) with increasing applied bias. Consequently, the driving force for charge transfer, $-\Delta G^{\circ\prime}$, will become potential-dependent. This scenario is shown in Figure 6.1 for depletion, flat-band, and accumulation conditions and should allow for utilizing an applied bias to push the system into the inverted regime. Preliminary analysis based on the framework in Chapter 4 allows for designing feasible system parameters (electrolyte, electrode, etc.) necessary to observe inverted behavior.

Direct 'inverted' behavior observed in a voltammetric response would consist of a decrease in the current at large applied bias. It should be noted for the simulated working curves presented here, that this decrease in current is symmetrical with the faradaic increase in current observed for a normal SUME response under low applied bias. That is, classical charge transfer theory is assumed.[5, 6] However, experimental results may show a non-symmetrical current decrease that would be indicative of vibronic contributions/non-classical behavior.[7] A key obstacle for observing this behavior is the cathodic solvent window of the electrolyte. Common solvents such as acetonitrile have relatively large potential windows and should be suitable for these measurements. Regardless, the ultimate goal of this analysis is to find electrode/electrolyte systems that show a current decrease at the most positive potential possible, i.e. exhibits the best chance for inverted behavior to be observed.

Figure 6.2a and 6.2b show the simulated voltammetric responses of n-Si SUMEs as a function of size and standard potential of the redox couple in solution, respectively. As the size decreases, the inverted behavior occurs at more positive potentials. This implies that a better chance for observing inverted conditions would be at smaller SUMEs. A similar trend is observed as $E^{\circ\prime}$ is set at more positive values, implying that a decrease in current is more likely to be observed when the semiconductor is pushed into accumulation quickly. This aspect is particularly informative for choosing a redox couple and semiconductor substrate for voltammetric measurement. That is, highly positive redox couples with $E^{\circ\prime}$ still located within the band gap are

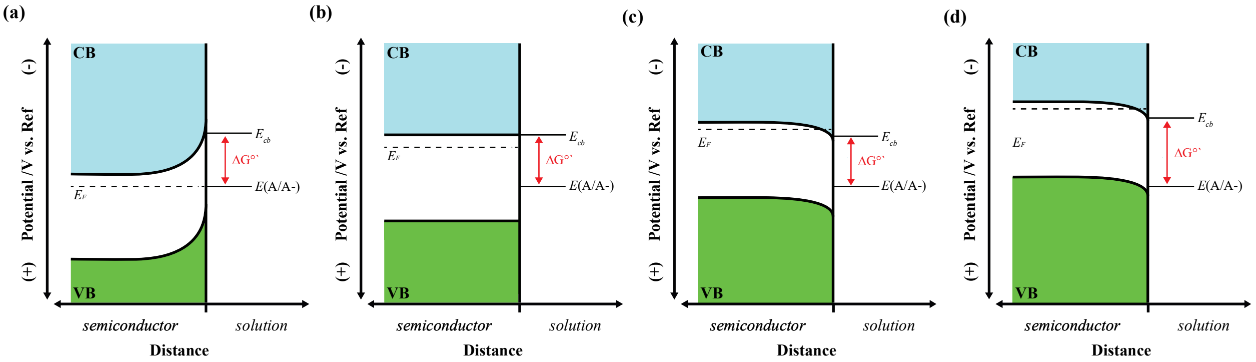

Figure 6.1. Changes in driving force for charge transfer, Δ*G*°`, under (a) depletion, (b) flat-band, and (c,d) differing degrees of accumulation.

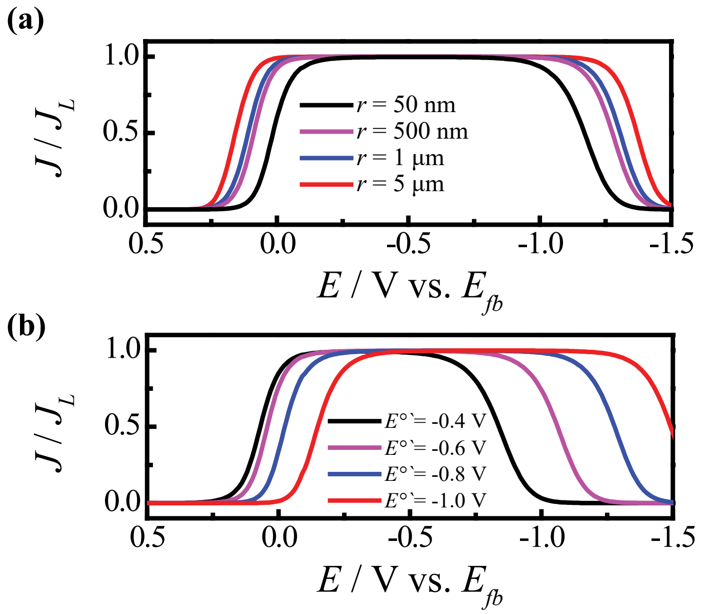

Figure 6.2. Simulated voltammetric responses of a n-Si SUME as a function of (a) electrode radius and (b) redox couple standard potential. For these working curves, $N_d = 10^{18}$ cm^{-3}, $N_{ss} = 5 \times 10^{14}$ cm^{-2}, $l = 0.2$ nm, $\lambda_{sc} = 0.6$, $E_{cb} = -1.0$ V, and $E_{ss} = 0.2$ V vs. E_{fb}.

desired (with n-type semiconductors). Preliminary work towards development of n-GaP (2.2 eV) and n-GaN (3.4 eV) SUMEs will be detailed below.

n-GaP (r = 5 μm) and n-GaN (r = 1 μm) SUMEs can be produced in a similar fashion to the n-Si SUMEs highlighted in Chapters 3 and 4. The main difference in the fabrication process flow is the necessity to minimize exposure of the III-V materials to high temperatures.[8, 9] This is accomplished with replacing the annealed SiO_xN_y insulator with a ~ 150 nm SiO_2 layer deposited by plasma-enhanced chemical vapor deposition at T = 350 °C. Voltammetric responses of these SUMEs were recorded in a N_2-filled glovebox with 2 mM $CoCp^+$ in anhydrous methanol and are shown in Figure 6.3a and 6.3b. Both GaP and GaN SUMEs exhibit a nominally sigmoid-shaped response, but the mass transfer-limited current for both electrodes is higher than the Cottrell-predicted value for a recessed UME (2.7 nA and 0.47 nA for r = 5 and 1 μm UMEs with 150 nm recession, respectively). These results have several implications for future work aimed at using these platforms for electroanalysis. First, the quality of the insulator should be verified. That is, detailed characterization of the SiO_2 structure and morphology should be carried out to identify the origin of excess current. No obvious pinholes were detected via optical microscopy, but methods with higher resolution should be sought out. If this becomes a persistent issue, alternative low-temperature insulator deposition processes, such as atomic layer deposition,[10] can be used for III-V SUME fabrication.

Additionally, the ideal electrolyte composition remains unresolved. Specifically, a highly positive redox couple needs to be identified. The ferrocenium cation is one possible option in that it can be prepared via electrolysis of ferrocene (or purchased commercially) and has a very positive standard redox potential (~ 0.2 V vs. E(Ag/AgCl)).[11] Potential issues with this species include the large amount of ferrocene impurities necessarily present in the salt (~ 4-5%) and the possibility of undergoing a second reduction step to metallic iron at large applied bias.[12] Further effort to identify an optimal redox couple for examination of charge transfer theories is necessary.

Nano-SUMEs

An interesting extension to the work described in Chapters 3 and 4 is to fabricate SUMEs with dimensions as small as possible. Not only does the obtainable mass transport-limited current density increase with decreasing size,[13] but the possibility for purposefully isolating or avoiding defects on the semiconductor surface emerges. Figure 6.4 highlights this principle through

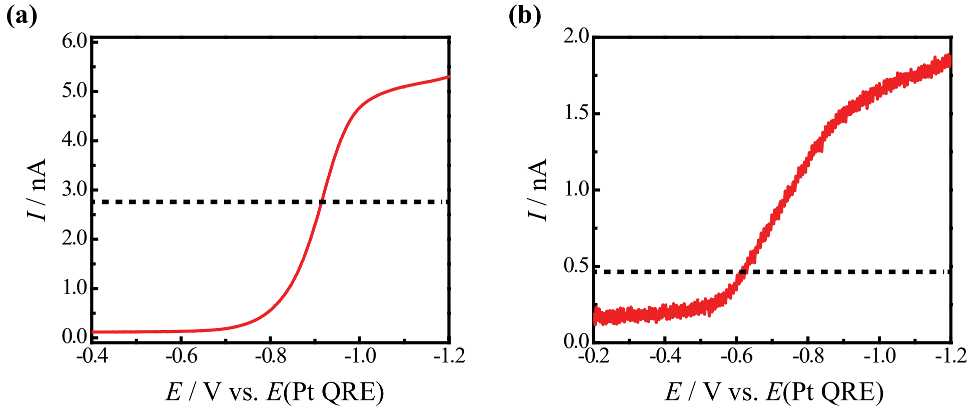

Figure 6.3. Linear sweep voltammograms of (a) 5 μm n-GaP and (b) 1 μm n-GaN SUMEs in contact with 2 mM $CoCp^+$. The dashed line indicates expected mass-transport limited current.

depicting two semiconductor electrodes with the same defect density, but different electrode areas exposed to solution. For the larger electrode shown in 6.4a, numerous defects are present and may impact charge transfer. However, for the masked, smaller electrodes in 6.5b, a distribution of defect characteristics will be observed. Importantly, there may be several electrodes that have a single or no defect in the active electrode area. Surface recombination velocities can be used a metric to identify semiconductor surfaces where the average distance between traps is relatively large. Velocities below 10 cm s^{-1} are obtainable on carefully prepared group IV semiconductor surfaces[14] (corresponding to an average trap separation larger than ~150 nm) and electron-beam lithography techniques should be capable of producing SUME active areas on the order of $r = 50$ nm.[15] It is unclear whether the fabrication process at this scale would introduce added defects or how to conclusively identify the voltammetric response characteristics of defect-less electrode. Nevertheless, the SUME platform developed in this thesis is highly amenable to probing fundamental charge transfer questions as described here.

Protection of Nanoporous GaP for Photoelectrochemical Water Oxidation

Given the simplicity of the method described in Chapter 5 for preparing dual-function protective catalyst layers, other relevant, but corrosion-prone photoelectrode materials could be stabilized for long-term photoelectrolysis using the same approach. In particular, n-GaP is a promising material for photoelectrochemistry.[16] With a band gap of 2.2 eV, a sufficient photovoltage for water-splitting can be generated while still absorbing a significant amount of the solar spectrum. A major challenge that has hindered wide-scale use of GaP for photoelectrochemical reactions is poor photogenerated electron and hole lifetimes combined with large absorption depths that limit the efficiency of charge collection.[17, 18] Increasing the porosity of the material has been a way to substantially improve the external quantum yields but leaves highly defective surfaces only operable for extended periods of time in non-aqueous media.[16] In this sense, devising thin film electrodeposition strategies for porous structures that improve interfacial kinetics while simultaneously mitigating degradation in aqueous environments would be highly beneficial for advancing GaP as a relevant photoelectrode material.

Fe-doped NiOOH (Fe:NiOOH) is a popular solar water oxidation catalyst given its high activity for oxygen evolution and stability in alkaline media.[19-21] The main question explored here is whether direct electrodeposition of Fe:NiOOH onto porous GaP can result in a uniform catalyst

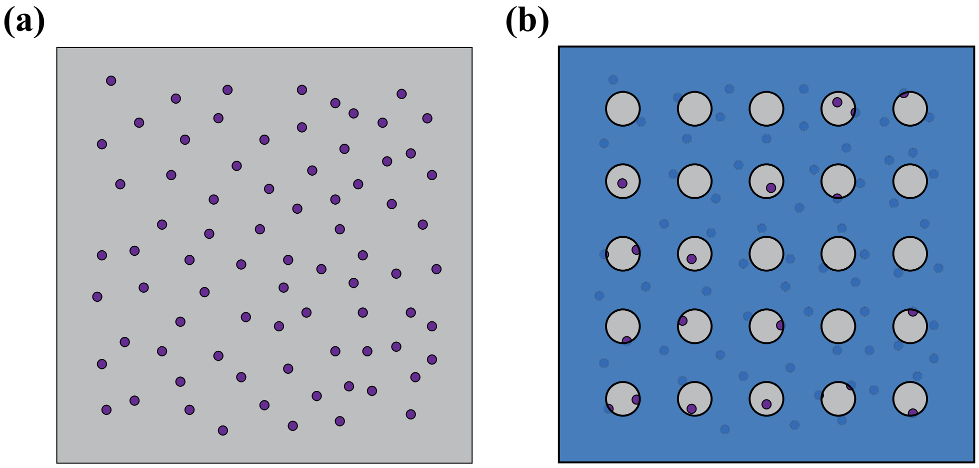

Figure 6.4. (a) Depiction of a macroscopic semiconductor electrode covered in surface traps. (b) Same electrode patterned into a SUME array. The purple dots indicate defined surface trap locations.

layer across the pore network and exhibit a high catalytic activity and durability. Porous GaP is fabricated by applying a +10 V (vs. *E*(Ag/AgCl) bias to a planar n-GaP substrate submerged in 0.5 M H_2SO_4. The strong positive bias pushes GaP into deep inversion, where holes tunnel to the surface and oxidize surface Ga atoms. The resulting oxide then easily dissolves in the acidic solution, forming a nanoporous network that corresponds to the optimal morphology for hole extraction (Figure 6.5a). A small complication of this process is that a surface layer exists post-anodic etch that minimizes access to much of the pore volume (Figure 6.5b). It is unknown whether this layer is the result of an inherent etching mechanism or re-deposition of dissolved oxides, but regardless, can be removed through brief immersion in commercial GaP etchants (e.g. Transene GaP Etch). After this second etch step, a freely-accessible pore network is formed (Figure 6.5c and 6.5d) that has a depth directly proportional to the electrochemical etching time. As highlighted in Figure 6.6, the nanoporous GaP photoanode exhibits significantly higher current densities than the planar counterpart in 1 M KOH under 100 mW cm^{-2} illumination.

The method for catalyst preparation used here involves the electrodeposition of $Ni(OH)_2$ through an indirect mechanism in nitrate-containing solutions,[22, 23] *eqs. 6.1* and *6.2,*

$$NO_3^- + 7H_2O + 8e^- \rightarrow NH_4^+ + 10OH^- \qquad (6.1)$$

$$Ni^{2+} + 2OH^- \rightarrow Ni(OH)_2 \qquad (6.2)$$

where the $Ni(OH)_2$ is converted to the active NiOOH form upon exposure to alkaline media,[22, 24-26] *eq. 6.3*

$$Ni(OH)_2 \rightarrow NiOOH + H^+ + e^- \qquad (6.3)$$

To explore how the deposition time effects the catalyst penetration through the pore network, un-doped $Ni(OH)_2$ was deposited from 50 mM $NiNO_3$ + 500 mM KNO_3 at an optimized cathodic current density of 0.3 mA cm^{-2} in the absence of illumination. Figure 6.7 shows energy dispersive spectroscopy (EDS) Ni K_α line scans across ~40 μm nanoporous GaP samples as a function of deposition time. For short times, Ni appears predominantly at the bottom of the pore structure. With increasing time, Ni is observed throughout the pore structure and at the longest time point explored here, it appears that Ni begins to accumulate at the top of the pore structure to the point where electrolyte access is almost completely blocked off. Figure 6.8 show transmission electron microscope images of the 60 min. sample at different depths within the pores. These images

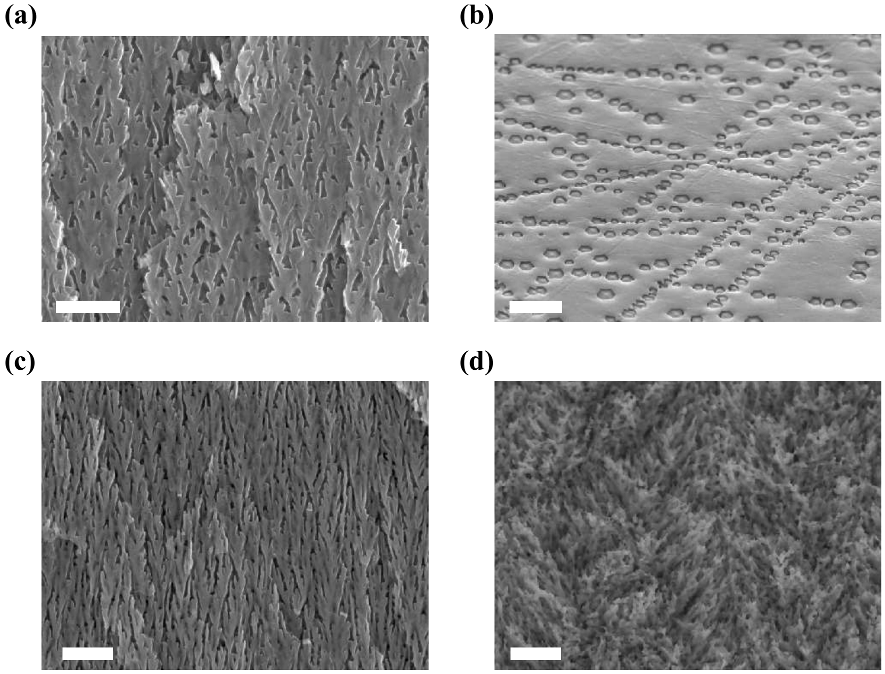

Figure 6.5. (a,c) Cross-section and (b,d) top-down scanning electron micrographs of anodically-etched GaP (a,b) before and (c,d) after immersing in a chemical etchant. Scale bars: 1 μm.

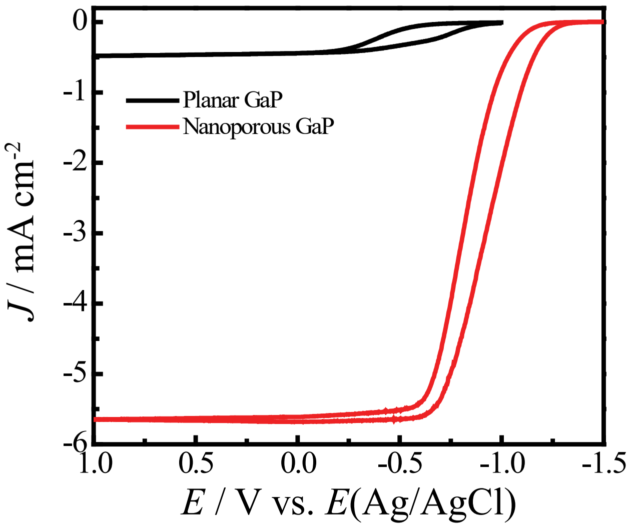

Figure 6.6. Voltammetric responses of planar and nanoporous GaP photoanodes in 1 M KOH under 100 mW cm^{-2} illumination.

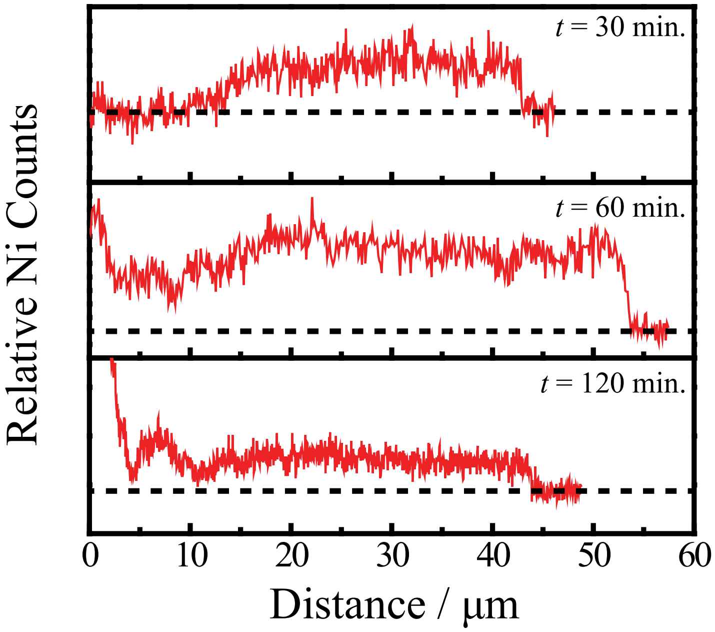

Figure 6.7. Ni EDS line scans for depositions times of 30, 60, and 120 minutes. The dashed line indicates Ni counts at the bulk GaP wafer base (i.e. baseline). Distance is plotted from top of the pore structure to bottom.

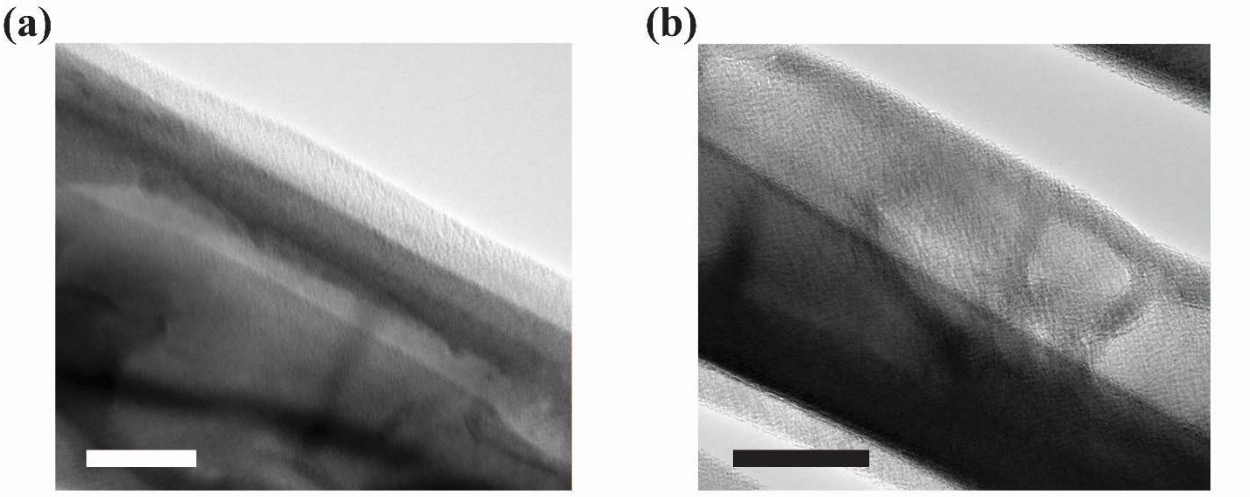

Figure 6.8. Transmission electron micrographs of a NiOOH-coated GaP sample at pore depths of (a) 4 μm and (b) 16 μm. Scale bars: 50 nm.

suggest that the deposit is coated across the pore volume, but the actual thickness depends on the depth. In total, these results suggest by altering deposition conditions (e.g. time), enough control over the deposit coverage is afforded for full coating throughout the pore volume.

Still, several aspects need to be addressed to produce a functional photoanode in which durability can be assessed. First, the composition of the deposit needs to be characterized. It is unclear at this point whether the Ni signal results from Ni metal, a NiO_x species, or $Ni(OH)_2$. The formation of the hydroxide salt is essential for conversion of the deposit to its most catalytically-active state.[24] Further, incorporation of Fe into these films needs to be detailed. In particular, determining how the initial deposition bath composition affects iron incorporation is essential for optimizing Fe content. FeOOH has a much lower solubility product value than $Ni(OH)_2$,[26] so the initially bath concentrations of Fe need to be very low relative to Ni. Finally, the combined photoanodes will have to be evaluated by several metrics relative to bare nanoporous GaP, including catalytic activity dependence of Fe-incorporation and film thickness dependence on light-limited photocurrent loss and durability. Such experiments will be germane in demonstrating catalyst electrodeposition on porous photoelectrodes for efficient photoelectrochemical water splitting.

SUME Arrays for Photoelectrochemical Water Splitting

A final proposal based on the work completed in this thesis marries the SUME platform with photoelectrochemical energy conversion systems. A SUME array platform fabricated by coating a semiconductor photoelectrode substrate with a semitransparent insulator (e.g. SU-8) may offer the possibility of enhanced photocurrents and photovoltages for photoelectrochemical reactions. For photocurrent enhancement, incident photons will illuminate both active and non-active electrode areas. If the individual SUME electrodes are spaced with pitches ~2x the minority carrier diffusion length, the effective photocurrent density will be ideally twice what was obtainable at a typically macroscopic electrode. The UME geometry will also support faster diffusion of reactants to the electrodes' surfaces. Additionally, the maximum photovoltage may be augmented in this design. The open-circuit voltage, V_{oc}, is proportional to the short-circuit photocurrent density, J_{sc}, (and thus the electrode area, A) through *eq. 6.4*[16]

$$V_{oc} = \frac{k_B T}{q} \ln\left(\frac{J_{sc}}{J_0}\right) = \frac{k_B T}{q} \ln\left(\frac{\Psi}{J_0 A}\right) \qquad (6.4)$$

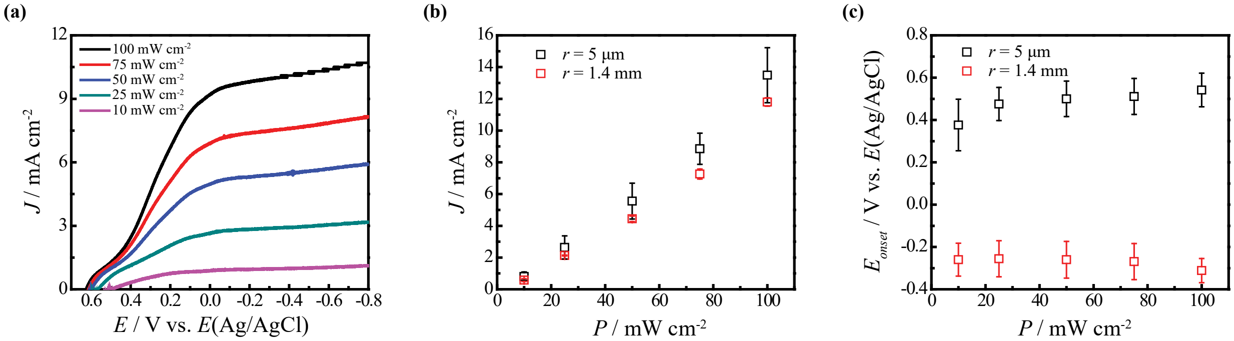

Figure 6.9. (a) Voltammetric response of a r = 5 µm p-GaInP$_2$ SUME in 0.5 M H$_2$SO$_4$ as a function of incident light intensity. (b) Current density of r = 5 µm and 1.4 mm p-GaInP$_2$ photoelectrodes as a function of light intensity. (c) Onset potential for r = 5 µm and 1.4 mm p-GaInP$_2$ photoelectrodes as a function of light intensity.

where J_o is the dark current density and Ψ is the number of photogenerated charge-carriers. That is, an increase in photocurrent per unit area is necessarily tied to increase in attainable photovoltage.

The current-potential response of a single, discrete 5 μm p-$GaInP_2$ SUME under illumination in 0.5 M H_2SO_4 was compared to its macroscopic counterpart to test the notion of enhanced photocurrent and photovoltage with small semiconductor/liquid contacts. The response of the SUME is shown in Figure 6.10a with the comparisons of photovoltage and photocurrent (the photocurrent onset potential in this case) in Figures 6.10b and 6.10c, respectively. The results follow the general prediction enumerated above, with small improvements in both the photocurrent and onset potential of the SUME photoelectrode. Ideally, this enhancement would be magnified with careful array design. Moreover, utilizing a poised solution will better define the exact magnitude of improvements in V_{oc}.

Further examination of carrier dynamics within the proposed semiconductor array device may prove fruitful in selecting device components and optimizing the SUME geometry. For example, this analysis assumes that the insulator/semiconductor junction will not impact carrier transport to the active electrode interface. Recombination sites at this junction may decrease the total number of useful photogenerated charge carriers.[27] Additionally, screening effects from the insulator may alter the electric field driving carriers to the interface,[28] especially if the electrode sizes approach the insulator thickness.

6.3. References

1. Fajardo, A. M.; Lewis, N. S. *Science* **1996,** *274*, 969.
2. Hamann, T. W.; Gstrein, F.; Brunschwig, B. S.; Lewis, N. S. *J. Am. Chem. Soc.* **2005,** *127*, 7815.
3. Hamann, T. W.; Gstrein, F.; Brunschwig, B. S.; Lewis, N. S. *J. Am. Chem. Soc.* **2005,** *127*, 13949.
4. Morrison, S. R. *Surf. Sci.* **1969,** *15*, 363.
5. Marcus, R. A. *J. Chem. Phys.* **1965,** *43*, 679.
6. Royea, W. J.; Fajardo, A. M.; Lewis, N. S. *J. Phys. Chem. B* **1997,** *101*, 11152.
7. Siders, P.; Marcus, R. A. *J. Am. Chem. Soc.* **1981,** *103*, 748.
8. Francis, C.; Bradley, M. A.; Boucaud, P.; Julien, F. H.; Razeghi, M. *Appl. Phys. Lett.* **1993,** *62*, 178.
9. Pearton, S. J.; Malm, D. L.; Heimbrook, L. A.; Kovalchick, J.; Abernathy, C. R.; Caruso, R.; Vernon, S. M.; Haven, V. E. *Appl. Phys. Lett.* **1987,** *51*, 682.
10. Groner, M. D.; Fabreguette, F. H.; Elam, J. W.; George, S. M. *Chem. Mater.* **2004,** *16*, 639.

11. Bond, A. M.; Mclennan, E. A.; Stojanovic, R. S.; Thomas, F. G. *Anal. Chem.* **1987,** *59*, 2853.
12. Ito, N.; Saji, T.; Aoyagui, S. *J. Organomet. Chem.* **1983,** *247*, 301.
13. Kim, J.; Bard, A. J. *Anal. Chem.* **2016,** *88*, 1742.
14. Yablonovitch, E.; Allara, D. L.; Chang, C. C.; Gmitter, T.; Bright, T. B. *Phys. Rev. Lett.* **1986,** *57*, 249.
15. Donthu, S.; Pan, Z. X.; Myers, B.; Shekhawat, G.; Wu, N. G.; Dravid, V. *Nano Lett.* **2005,** *5*, 1710.
16. Price, M. J.; Maldonado, S. *J. Phys. Chem. C* **2009,** *113*, 11988.
17. Wight, D. R.; Blenkinsop, I. D.; Harding, W.; Hamilton, B. *Phys. Rev. B* **1981,** *23*, 5495.
18. Aspnes, D. E.; Studna, A. A. *Phys. Rev. B* **1983,** *27*, 985.
19. Klaus, S.; Cai, Y.; Louie, M. W.; Trotochaud, L.; Bell, A. T. *J. Phy.s Chem. C* **2015,** *119*, 7243.
20. Michael, J. D.; Demeter, E. L.; Illes, S. M.; Fan, Q. Q.; Boes, J. R.; Kitchin, J. R. *J. Phys. Chem. C* **2015,** *119*, 11475.
21. Chen, J. Y. C.; Dang, L. N.; Liang, H. F.; Bi, W. L.; Gerken, J. B.; Jin, S.; Alp, E. E.; Stahl, S. S. *J. Am. Chem. Soc.* **2015,** *137*, 15090.
22. Jayashree, R. S.; Kamath, P. V. *J. Power Sources* **2001,** *93*, 273.
23. Wohlfahrt-Mehrens, M.; Oesten, R.; Wilde, P.; Huggins, R. A. *Solid State Ionics* **1996,** *86-8*, 841.
24. Gao, M. R.; Sheng, W. C.; Zhuang, Z. B.; Fang, Q. R.; Gu, S.; Jiang, J.; Yan, Y. S. *J. Am. Chem. Soc.* **2014,** *136*, 7077.
25. Diaz-Morales, O.; Ferrus-Suspedra, D.; Koper, M. T. M. *Chem Sci* **2016,** *7*, 2639-2645.
26. Cai, L. L.; Zhao, J. H.; Li, H.; Park, J.; Cho, I. S.; Han, H. S.; Zheng, X. L. *ACS Energy Lett.* **2016,** *1*, 624.
27. Aberle, A. G.; Glunz, S.; Warta, W. *J. Appl. Phys.* **1992,** *71*, 4422.
28. Fu, K. Y.; Han, D.; Ma, C. X.; Bohn, P. W. *Nanoscale* **2017,** *9*, 5164.